ARMY RESEARCH LABORATORY

A Computational Study of Munitions Response to Double Impact and Crushing Impact From a Flyer Plate

Patsy B. Simmers
Richard E. Lottero

ARL-TR-2279

AUGUST 2000

Army Research Laboratory
Aberdeen Proving Ground, MD 21005-5066

ARL-TR-2279 August 2000

A Computational Study of Munitions Response to Double Impact and Crushing Impact From a Flyer Plate

Patsy B. Simmers
Richard E. Lottero
Weapons and Materials Research Directorate

Abstract

This report describes the results of a series of hydrocode computations, each of which modeled a steel flyer plate striking a single munition, either an M2A3 or an M483, in one of two different mounting configurations. One mounting configuration was for the munition to be first struck by the flyer plate and then to subsequently translate and strike a backing plate. The second configuration was to have the munition mounted with a buffer pack in contact on the flyer-plate side and be in initial contact with the backing plate on the opposite side. Some of the computations simulated experiments that were previously performed and reported by the U.S. Army Research Laboratory. Those experiments were not instrumented, so only limited data were produced. The primary purpose of the computations was to compute the pressures that may have occurred in the explosive fill to help explain the various exothermic reactions (or lack thereof) that occurred. Several different flyer-plate velocities were simulated in the computations. A brief discussion of parameters that may be related to ignition by shearing is also included.

ACKNOWLEDGMENTS

Technical consultation on the selection of munitions to be modeled was provided by Drs. Robert Frey and John Starkenberg of the U.S. Army Research Laboratory (ARL). Technical consultation and support in the use of the latest versions of the CTH hydrodynamics computer code were provided by Messrs. Stephen Schraml and Kent Kimsey of ARL and by Dr. Eugene Hertel of Sandia National Laboratories, New Mexico. Technical and financial support were provided by Mr. Duane Scarborough of the U.S. Army Defense Ammunition Logistics Activity, New Jersey. The technical review of this report was provided by Dr. Patrick Baker of ARL. The assistance and support of all these people are gratefully acknowledged.

INTENTIONALLY LEFT BLANK

TABLE OF CONTENTS

LIST OF FIGURES

INTENTIONALLY LEFT BLANK

LIST OF TABLES

INTENTIONALLY LEFT BLANK

A COMPUTATIONAL STUDY OF MUNITIONS RESPONSE TO DOUBLE IMPACT AND CRUSHING IMPACT FROM A FLYER PLATE

1. Introduction

A continuing problem for the U.S. Army has been to find ways to prevent chain reactions from occurring in munitions storage areas. When some initiating event occurs in a stack of munitions, chain reactions can subsequently occur in nearby stacks of munitions. The munitions stack that experiences the first initiating event is hereinafter referred to as the "donor" stack. A munitions stack that is in proximity to a donor stack is referred to as an "acceptor" stack. Any munition within such a stack is referred to as an "acceptor" munition, or simply as an "acceptor." Often, the result is that much or all of the supply of munitions and other materiel in the storage area is lost. The chain reaction can propagate by a variety of means. Some of the means are (a) relatively immediate sympathetic detonation caused by impact or shock and (b) somewhat slower initiations caused by such events as crushing at high strain rates, fragment impact and penetration, and fire. Not all of the relatively prompt (i.e., within milliseconds) impact-related mechanisms for causing a true high-order detonation are well understood and are a matter of continuing debate. The criteria for direct initiation of detonation by shock overpressure are relatively well known. An excellent discussion of direct shock initiation of explosives is presented in a report by Liddiard and Forbes.[1] The major findings of that report are that the modified gap test (MGT) [2] indicates that the "...onset of detectable burning occurs at peak stresses in explosives of 8.8 to 75.0 kbar in the explosives that have been tested..." and the underwater shock test (UST) [2] indicates that "...burning occurs at peak stresses of 4 to 12 kbar in the explosives..." A further statement is made [1] that "...compression by a 3- or 4-kbar shock is, of itself, a sufficient external stimulus to start chemical reaction in a heterogeneous solid explosive such as pentolite."

The criteria for predicting the initiation of explosives, through either relatively prompt high-order detonation or a much slower burning process, by an event dominated by mechanical shearing are not as well understood and are a matter of continuing debate. Liddiard and Forbes [1] also presented a brief discussion of shear initiation of explosives, including a table that showed the threshold of burning for various explosives for combinations of lateral "...flow rates of 28-45 m/s resulting from shock pressures in water of 3-6 kbar." These shock pressures, when combined with lateral flow, are generally lower for a given explosive than the shock pressures for simple shock initiation. Here, lateral flow refers to flow induced in the explosive in a normal direction to the shock velocity vector. In a material that can support viscous and deviatoric stresses, the lateral flow is reasonably related to and is an indicator of shearing stresses and the strain rate in that normal direction. The initiation of explosives by shear has been considered for some time as a possible mechanism, through either simple friction at surfaces or the formation of shear bands. Frey [3] suggested a model that describes the heating that could occur at either sliding interfaces or shear bands, along with temperature limitations imposed by melting. Incipient shear bands having a width on the order of 0.1 μm were assumed by Frey to start the computations. For shear applied over a region 0.1 mm wide, the shear band grew to a width of 0.24 μm at the time the peak temperature (about 1100-1200 degrees C) was reached. The shearing velocity in this case was 0.2 km/s and the pressure was 10.3 kbar. For shear applied over 2.0 mm under the same conditions, the model indicated that the peak temperature would be reached in approximately 1.3 μs. A summary [4] of shear initiation experiments, along with applications of Frey's model, provides additional insight into the problem. The computations described therein indicated that widths of shear bands could be on the order of 1.0 μm. A maximum temperature (limited by the melting temperature) could be reached in about 1.0 μs. Howe [5] showed through the analysis of collected experimental data that, in addition to the classical shock initiation mechanism, there is evidence that supports shear as a mechanism for initiation. This is further supported by a study [6] of damage patterns and detonation within the explosive fill in cased munitions struck by flying steel plates. Kipp [7] presented a model that showed that shear band formation is a feasible mechanism for the initiation of granular explosives. The computed shear band widths were comparable to those suggested by Frey.[3] Comparison was also made with available data. The study focused on shear and did not include porous collapse mechanisms. Coffey [8] used heat-sensitive film to identify hot spots in energetic materials subjected to low-level impact or low-level shock and presented an analysis to support the contention that the hot spots were associated with regions of high shear.

The preceding has been presented as an extended introduction to the topic of this report to clarify the evolution of the analysis that is presented here. The computations that are discussed here were primarily designed to analyze the shock pressures in a series of problems modeling the impact of a steel flyer plate on two different munitions. As the analysis developed, it became clear that the shock pressures that were computed were consistently low as compared with the shock initiation criteria of Liddiard and Forbes.[1] It became evident that an argument was building for the presence of another initiating mechanism, very possibly shear, in the experiments [9] that were being simulated in the study that is being reported herein because several of those experiments resulted in initiations. With that, the discussion of the current work will proceed.

The computations reported herein constitute one part of a continuing U.S. Army Research Laboratory (ARL) project, "Munitions Survivability Technology," supported and funded by the U.S. Army Defense Ammunition Logistics (Ammolog) Activity. Earlier computational work on this project, which has been completed and reported, focused on evaluating the blast from the complete high-order detonation of a simplified donor munitions stack modeled as a bare charge, the loading on and response of various intervening barricades, and the subsequent loading on and response of an acceptor munitions stack. The first ARL report [10] documented a pair of uncoupled hydrodynamics computer code ("hydrocode") computations that used a 1996 version of the CTH [11] hydrocode. (Please see the appropriate references for information about the CTHGEN users' manual [12] for grid generation and the CTH users' manual [13] for running the CTH hydrocode.) Both the donor and acceptor munitions stacks were simplified versions of stacks of 72 pallets each of M107 155-mm munitions.[14] The choice of the munitions stack configuration for those and all subsequent computations for munitions stacks to this time was based on earlier ARL work on fragmentation propagation.[15] The donor stack was modeled here and in all similar computations as a bare explosive charge with a nominal mass of 4,000 kg of Composition B (hereinafter referred to as "Comp-B" in the text for brevity). The term "uncoupled" is used here in a specific mathematical sense.

The first attempts to run a single, fully coupled computation resulted in failures because of numerical stability problems. This computation attempted to include the detonation of the donor stack, the loading and response of the barricade, the impact of the barricade in its distorted form against the acceptor stack, and the loading and response of the acceptor stack in a single simulation. Because of the failures, the problem was divided into two uncoupled computations. Using simplified representations of the stack and barricade in a two-dimensional (2-D) Cartesian coordinates system, the first of the two uncoupled computations in that report [10] simulated the detonation of the donor stack, the loading on a water barricade, and the ensuing bulk motion of the water barricade. Performing computations in a 2-D Cartesian coordinates system implies that any resulting distortion of the barricade up to actual break-up would be in a "plane-strain" mode. The water barricade shape being evaluated was based on a design provided to Ammolog by one of its contractors.[16] A simplified trapezoidal cross section for the water barricade was assumed, with the sloping sides having a 30-degree included angle to a line perpendicular to the ground plane. The separation distance, i.e., the "standoff distance," measured along the ground plane between a presumed right face of the donor stack and the left-most edge at the bottom of the water barricade was 3.05 m (10.0 ft). This 3.05-m standoff was identified by Ammolog and its consultants as a probable first estimate of the standoff distance that might be chosen for field use in the absence of any new technical guidance. The second of the two uncoupled computations simulated the water barricade, reformed into its original undistorted shape, traveling toward the acceptor stack at the final bulk velocity from the first computation and impacting the acceptor stack. This provided insight into the peak pressures and integrated blast and impact loading on the acceptor stack and its whole-body response to that loading. However, the effect of the decoupling on the loading on and response of the acceptor stack could not be quantified in that report. This work was also summarized in a technical paper.[17]

A later version of CTH [11] (this is still the basic reference), along with the complementary documentation and instructions for the grid generation [18] and

CTH hydrocode [19] input options and execution instructions, was used to run the first of three series of fully coupled computations.[20] These 2-D Cartesian computations simulated the same donor and acceptor stacks and trapezoidal water barricade as were simulated in the previous study.[10] Five computations were completed, each for a different standoff distance. The standoff distances in each computation were kept equal between both the donor stack and the barricade on one side and the barricade and the acceptor stack on the other side. These standoff distances were 2.00 m, 2.25 m, 2.50 m, 2.75 m, and 3.05 m. This version of CTH had better numerical stability than the previous version, so it was possible in each of the five computations to run the problems in a fully coupled mode. The essential difference is that the impact of the barricade on the acceptor stack for the computation for the 3.05-m standoff in this series had the barricade striking as a distorted and differentially accelerated mass rather than as a reshaped mass with a uniform bulk velocity as was done in the second of the two uncoupled computations.[10] One of the primary points of information from this first series of computations was that there is a disproportionately small increase as an inverse function of standoff distance in loading on and bulk acceleration of the acceptor stack over this 2.00-m to 3.05-m range in standoff distances. This indicated that there may be only a moderate penalty in increased loading on the acceptor stack in this simplified simulation for a relatively large reduction in required land area for at least a field-expedient, temporary munitions storage site. The sloping sides of the trapezoidal water barricade also helped to develop shear layers in the flow that kept explosive products from impinging on the acceptor stack during all of the nominal 40-ms simulation times.

The second series of fully coupled computations simulated the same donor and acceptor munitions stacks separated by a water barricade with a thin (1.17-m width) rectangular cross section.[21] Three standoff distances (2.00 m, 2.50 m, and 3.05 m) were simulated to match three of the previously simulated distances and cover the same range. It was noted in that report [21] that changing from the trapezoidal cross section to the rectangular for a given standoff had the effect, which is probably undesired, of moving the center of mass of the barricade closer to the donor stack. The thin rectangular barricade also had a significantly smaller mass per unit depth (28.6 kg/cm) in the 2-D Cartesian computational flow field than did the trapezoidal cross section barricade, which had 58.7 kg/cm of depth. Comparisons with the previously reported computations for the water barricade with the trapezoidal cross section showed that the barricade-impact loading on the acceptor stack was much greater at a given standoff for the thin rectangular barricade. This was shown to be primarily because of a combination of the greater efficiency of the vertical sides of the thin rectangular barricade in accumulating greater loading in both peak values of pressure and total integrated impulse from the detonation of the donor stack, the lower mass of that barricade, and the greater efficiency of its vertical opposite side in delivering loading to the acceptor stack. Considerable amounts of explosive products impinged directly on the acceptor stack at later time for all of the computations for the thin rectangular water barricade, which was also disintegrated and swept out of the flow field much more quickly than was the case for the trapezoidal barricade.

The third series of fully coupled computations simulated the same configurations as for the thin rectangular water barricade except that in these, the water barricade thickness was 1.70 m. The mass of that water barricade was 41.5 kg/cm of depth. These computations were reported [22] along with a summary analysis that included all of the results from the three series of fully coupled computations. A simple correlation was presented that related the final values of the total integrated impulse on the side of the acceptor stack facing the barricade for all computations with a scaled barricade mass. This scaled barricade mass was computed from a combination of the actual barricade mass per centimeter of depth, a trigonometric function for the slope of each of the two sides of the barricade, and a 1/3 power of the standoff distance.

The plans for computations for the current fiscal year include performing, analyzing, and reporting three-dimensional (3-D) computations of at least the trapezoidal water barricade with a 3.05-m standoff for the same donor and acceptor munitions stacks to quantify the 3-D versus 2-D effects on loading. This will be done with the latest version of CTH with a massively parallel computation. Also, attempts had been made with one of the earlier versions of CTH to simulate sections of either water or dry sand striking stacked rows and columns of simplified individual munitions at various velocities in the range of those obtained from the 2-D computations. Enough of those computations failed because of numerical stability problems that they were not deemed to be of sufficient merit to warrant full analysis and publication of the results. If time and funding permit, these computations will be run with the latest version of CTH to see if the particular numerical stability problems that arose in those geometries can now be overcome.

Hopefully, this summary of computational work completed to date and planned for this year has served to place the work that is being reported herein in proper perspective. The discussion now shifts to the latest computations and their specific background and relation to munitions survivability. Several years ago, a series of experiments [9] was performed at ARL with the goal of identifying at least some worst-case acceptors among munitions by subjecting several different types of munitions to either double impact or crushing impact from a steel flyer plate. This report documents the results of continuum mechanics computer code calculations that simulate a particularly interesting subset of those experiments, plus several complementary computations that simulate conditions that were not included in the experiments. The purpose of this computational study was to provide additional insight to aid in the understanding of the results of those experiments.

2. Earlier Experimental Work

The experiments [9] of direct interest in this report are those that involved either double impact or crushing impact. Double impact occurs when a round is struck on one side, is accelerated, and then strikes another independent object. That other object could be anything, including another munition. Crushing impact occurs when a heavy object strikes buffering material on one side of a munition that is already in contact with another munition or hard object on its opposite side. Two of the munitions that were identified in that study as candidates to be considered as probable worst-case acceptors for either double or crushing impact are the M2A3 demolition charge and the M483 155-mm projectile. The M2A3 now has Comp-B as its only available explosive fill for rounds entering the inventory. The earlier, more sensitive version with a pentolite fill is no longer being produced and is generally not available. The M483 contains a large number of individually cased submunitions that have A5 for an explosive fill. A5 is a sensitive explosive containing 98.5 percent rapid detonating explosive (RDX).

Four different flyer-plate sizes were used in the actual experiments. The largest flyer plate, 10.16 cm thick by 45.72 cm high by 76.1 cm wide (4.0 in. by 18.0 in. by 30 in.), was specifically identified [9] as the one used for the 155-mm munitions, including the M483 projectile. The size of the flyer plate that was used in the experiments for the M2A3 was not given, so it was assumed from the context of the report to be of the same size as for the M483. All flyer plates were described as being made of steel, but specific alloys were not identified. All experiments included a massive steel backing plate against which the munition was either impacted and subsequently crushed (double-impact experiments) or simply crushed (crushing experiments). Buffer packs for the crushing experiments were made of alternating layers of high-density polyethylene and steel, eight layers in all, with each layer 2.54 cm (1.0 in.) thick. All buffer packs in the experiments began with a polyethylene layer on the flyer-plate side and ended with a steel layer on the munition side. The reader is referred to the original technical report for details of the physical layouts of the experiments. The various types of exothermic reactions (or lack thereof) of the munitions observed by the experimenters were noted in their report.

3. Summary of CTH Hydrocode Computations

The computations reported herein were performed with the CTH [11] hydrodynamics computer code, or "hydrocode." The CTH hydrocode was developed by the Sandia National Laboratories, which also provides continuing support to the user community in the use of the code. The guidelines and options available for use of CTH's grid generation code are given in the CTHGEN user's manual [18] and for the CTH hydrocode in its user's manual.[19] All of the CTH hydrocode computations performed in the current study, which simulate the double impact and the crushing interactions, are summarized in Table 1. The first column in Table 1 shows the identifying name for each computation that will be used in this report. That identifying name can be broken down to give specific information for each simulation. The first character is either a "D" for "double impact" or a "C" for "crushing impact." The second through fourth characters are either "M2-," indicating the M2A3 munition, or "M4-," indicating the M483. The two- or three-digit numbers that follow indicate the impact velocity of the flyer plate in meters per second. The presence of an "R" at the end of the identifying name for the crushing-impact computations indicates that the computation simulated a reverse-ordered buffer pack. If no letter appears at the end of an identifying name for a crushing-impact computation, the simulation of a forward-ordered buffer pack should be assumed. No experiments actually used a reverse-ordered buffer pack; these computations were performed to allow an evaluation of the effects of changing the sequential order of layers in a buffer pack. No double-impact computation or experiment used a buffer pack of any kind. The notations in parentheses in the penultimate column are taken from the experimenters' reported observations. "No Go" indicates that no exothermic reaction in the explosive fill of the munition was observed; "Burn" indicates a simple burning; "Expl" indicates an explosion but not a detonation; and "Det" indicates a confirmed high-order detonation. The last column contains the time that was simulated in each of the computations. The computations that match actual experiments are discussed in detail in this report. Limited subsets of information from the additional, complementary computations are presented after the discussion of the computations that matched the experiments. All CTH computations were performed in 2-D Cartesian coordinates. The munitions were modeled as cross-sectional cuts normal to the axis of symmetry of semi-infinite cylinders with a unit depth of 1.0 cm, measured along that axis of symmetry in this 2-D coordinate system.

The steel in all CTH computations was modeled as 4130 steel with the Mie-Gruneisen equation of state (EOS). The previous CTH computations [9] used Lucite to simulate the polyethylene layers in the buffer packs. Although both polyethylene and Lucite data for the Mie-Gruneisen EOS were available in CTH, it was decided to also model the polyethylene as Lucite within the Mie-Gruneisen EOS to allow for later possible comparisons with those earlier computations. No such direct comparisons are made in this report. The unreacted Comp-B was also modeled with the Mie-Gruneisen EOS. Because the mechanical properties of the A5 explosive fill for the M483 were not as well documented as were those for Comp-B, the unreacted A5 was also simulated as Comp-B. It is important to note that the M483 in the computations discussed here was further simplified as an outer steel casing with a single, continuous, complete fill of Comp-B. This was done because attempting to model the individual submunitions with their casings and explosive fills and also model the open spaces between the submunitions would have forced the grid resolution to a much finer level. The resulting computations would have been much more complex, time consuming, and well beyond the scope of the effort. Thus, this simplified representation of the M483 is not a good representation of an actual one and should be considered as being more representative of a generic, high explosive (HE)-filled round.

The unreacted Comp-B was designated for all runs as capable of detonating within the logic of the "history variable reaction burn" (HVRB) model [23] if the dynamics of a given interaction met the HVRB initiation criteria. If any such reactions occurred, the input data were configured to model the explosive products [24] within the Sesame [23] EOS package. No exothermic reactions of the Comp-B were automatically triggered in any of the computations, so no explosive products were generated. A recent study [25] showed good performance of the HVRB model within CTH computations in properly predicting shock initiation of various explosives for flyer plates impacting at velocities that were typically much higher than those used in the current study. That study also used considerably finer zoning than is being used here, but that may not be a primary issue. A typical density [26] for the unreacted Comp-B was assumed. The various parameters and constants used to set the properties of those materials are summarized in Table 2. It must be noted here that there was uncertainty and inconsistency in choosing a value for Poisson's ratio, ν, an elastic-deformation parameter, for the unreacted Comp-B explosive fill. A value of 0.35 (reasonable) was used for the crushing-impact computations and a value of 0.45 (too high) was used for the double-impact computations. The effect of having these different values for ν on the results of the computations, particularly pressure, was unknown. As a check, computation CM2-45 was rerun as computation CM2-45pr with all parameters kept the same except for setting $\nu = 0.45$. The differences in representative pressure peaks were relatively minor. This is discussed in more detail in Section 5. The authors regret having introduced this added uncertainty. At least the resulting need to address the issue of choosing a proper value for ν for the part of the response of the explosive fill that was elastic in nature has expanded the conveyance of information in this report.

All computations were run until both the flyer plate and the munition had either come to rest or were in a sustained rebound phase. The typical simulated times were on the order of 4.0 to 8.0 ms, measured from a defined zero time at the instant of the impact of the flyer plate on the outside (i.e., left-most) surface of the munition or the buffer pack, as appropriate.

Table 1. Summary of Double-Impact and Crushing-Impact Computations That Use the CTH Hydrocode

Computational Identifier	Acceptor Munition	Flyer Plate Impact Velocity (m/s)	Buffer Pack Layers Plate to Munition Each Layer 2.54 cm Thick L=Lucite, S=Steel	Match to Experiment? (result of experiment)	Simulated Time (ms)
DM2-15	M2A3	15.0	No buffer pack	Yes ("No Go")	8.00
DM2-24	M2A3	24.0	No buffer pack	Yes ("Expl")	6.00
DM2-45	M2A3	45.0	No buffer pack	Yes ("Det")	6.00
DM2-100	M2A3	100.0	No buffer pack	No	5.00
DM4-33	M483	33.0	No buffer pack	Yes ("No Go")	6.00
DM4-45	M483	45.0	No buffer pack	No	6.00
DM4-49	M483	49.0	No buffer pack	Yes ("Expl")	5.00
DM4-100	M483	100.0	No buffer pack	No	5.00
CM2-45	M2A3	45.0	L/S/L/S/L/S/L/S	Yes ("Burn")	5.27
CM2-100	M2A3	100.0	L/S/L/S/L/S/L/S	No	5.25
CM2-300	M2A3	300.0	L/S/L/S/L/S/L/S	No	3.36
CM2-45R	M2A3	45.0	S/L/S/L/S/L/S/L	No	5.27
CM2-100R	M2A3	100.0	S/L/S/L/S/L/S/L	No	4.75
CM4-43	M483	43.0	L/S/L/S/L/S/L/S	Yes ("No Go")	4.00
CM4-45	M483	45.0	L/S/L/S/L/S/L/S	No	4.00
CM4-95	M483	95.0	L/S/L/S/L/S/L/S	Yes ("Expl")	4.00
CM4-100	M483	100.0	L/S/L/S/L/S/L/S	No	3.77
CM4-45R	M483	45.0	S/L/S/L/S/L/S/L	No	4.85
CM4-100R	M483	100.0	S/L/S/L/S/L/S/L	No	5.33

Table 2. Constants and Properties for Mie-Gruneisen Materials (in CTH input units)

Constant or Property	Steel	Unreacted Composition B	Lucite
Density (g/cm^3)	7.81	1.72	1.181
Sound Speed (cm/s)	4.58x10^5	2.55x10^5	2.26x10^5
Constant Volume Specific Heat (ergs/(g-ev)) (ev=electron volt)	5.091x10^{10}	1.35x10^{11}	Nominal default 1.0x10^{10}
$U_s - U_p$ Linear Hugoniot Coefficient (-)	1.49	1.99	1.816
Gruneisen Parameter (-)	1.69	1.0	0.75
Yield Strength			
(dynes/cm^2)	12.0x10^9	5.0x10^8	4.2x10^9
(kbar)	12.0	0.5	4.2
Poisson's Ratio		Dbl Imp = 0.45	
(-)	0.279	Crush = 0.35	0.45
Best for Future?		0.285	0.321
Melting Point	(Set high)		(Set high)
(ev)	1.0x10^{10}	4.8x10^{-2}	1.0x10^{10}

4. A Comparison of the Double-Impact Computations and Experiments

4.1 The Computational Grid Geometry

The geometries of the computational flow fields used for all double-impact computations for the M2A3 and M483 munitions are described in Table 3. The computational cell sizes were approximately 0.1 cm in each direction. This grid resolution (i.e., degree of fineness in cell sizes) was chosen primarily for the purpose of adequately resolving the shock fronts that were expected to be generated as a result of the impact of the flyer plate on the munition in the grid. Another contributing factor in this choice of cell size was that no data were taken in the experiment to determine either the time of the first indication of an energetic reaction relative to a reference time or the location within the munition of that first reaction. Thus, it was decided that all computations would be run until an actual explosive initiation was indicated by the computation (discussed later) or a reversal of velocity of the flyer plate (i.e., a rebound) was computed. This fixed the probable range of simulated time in the computations at 4.0 to 8.0 ms, depending on the initial flyer-plate velocity and the combination of the munition and any buffer pack that might be present. Given the processor speed of the ARL Major Shared Resource Center (MSRC) SGI[1] Origin 2000 computer system on which the computations were run, the total number of computations that were planned, the allotted time and resources, and the decision at the time to focus on looking for possible indications of shock initiation, the choice of 0.1-cm cell sizes was confirmed. The ARL MSRC is maintained and operated by ARL at Aberdeen Proving Ground, MD, on behalf of the Department of Defense High Performance Computing Modernization Office, which owns the computing assets. A discussion is presented later in this report of parameters related to shear initiation for some of the computations. However, because this grid resolution and the material model are entirely inadequate for a proper study of the development of shear bands within the explosive, the data that are presented must be regarded only as an interesting but intrinsically incomplete commentary.

---

[1] not an acronym

Table 3. Main Features of Flow-Field Geometry for the Double-Impact Computations

Left to Right in X-Direction Geometry	X Direction (cm)	Y Direction (cm)	Shell Thickness (cm)
Reflective Left Boundary	Yes	-	-
Reflective Left Boundary to Flyer Plate Simulated as a Void	(Open Span) M2A3 - 3.39 M483 - 3.35	-	-
Steel Flyer Plate	(Thickness) Both - 10.16	(1/2 Height) Both - 22.86	
Phenolic Shell, Simulated as a Void	-	-	M2A3 - 0.3175
Steel Shell	-	-	M483 - 1.33985
Unreacted Composition B	(Diameter) M2A3 - 17.145 M483 - 12.8143	(Radius) M2A3 - 8.5725 M483 - 6.4072	-
Phenolic Shell, Simulated as a Void	-	-	M2A3 - 0.3175
Steel Shell	-	-	M483 - 1.33985
Outer Shell Surface to Backing Plate Simulated as a Void	(Open Span) M2A3 - 7.06 M483 - 9.346	-	-
Reflective Right Boundary Simulating Backing Plate	Yes	-	-
Reflective Bottom Boundary to Transmissive Top Boundary	-	M2A3 - 35.05 M483 - 35.0	-

4.2 Results of the M2A3 Double-Impact Computations

4.2.1 Analysis of Flow Fields for the M2A3 Double-Impact Computations

Computation DM2-15 simulated the impact of the flyer plate traveling at 15.0 m/s on an M2A3 munition and the subsequent second impact of the accelerated munition against the backing plate. This was a "No Go" event in the experiment [9], indicating that no exothermic reaction occurred in the Comp-B explosive fill. The time at the start of the computation, as it will be in all double-impact computations, is defined as t = 0.00 at the theoretical instant of impact of the flyer plate on the outside surface of the munition's shell. The flow field at time t = 0.00 for computation DM2-15 is shown in Figure 1. In this figure, the flyer plate is moving from left to right at 15.0 m/s, which is also the measure of positive X-direction velocity. The red hemisphere representing the explosive fill of the M2A3 is stationary. Because of difficulties in finding a suitable material to simulate the phenolic case of the M2A3 in the CTH materials library, its thinness (0.3175 cm) (which would have then dominated the computational grid sizing), and its minimal strength, the case was simulated simply as a void for all M2A3 double-impact computations. It was omitted from the crushing-impact computations. Thus, t = 0.00 is more specifically defined here as the time at which the flyer plate would have struck the actual left-most location of the M2A3 as it was modeled. Air was not simulated in this or any of the other computations because its inclusion for the types of interactions simulated here would have only added complexity without corresponding improvements in the fidelity of the computations. Massless "tracers," which record flow-field data versus time, were placed at a variety of locations and are indicated by the asterisks in the figure. The column of asterisks at the X = 35.0-cm location in the figure indicates a series of tracers placed along the reflective right boundary representing the steel backing plate.

There is only a minor amount of distortion at the left face of the explosive fill of the M2A3 as it is accelerated by the impact of the flyer plate and translated rightward toward the steel backing plate. As an illustration of this, Figure 2 shows the flow field at 4.00 ms. The right-most edge of the explosive fill is still about 2.5 cm away from impacting the backing plate at that time. The explosive is showing essentially no significant distortion at that edge. Figure 3 shows the flow field at 6.00 ms. The right-most edge of the explosive fill has just impacted the backing plate. The explosive is showing only minor distortion at that edge. Figure 4 shows the flow field at 8.00 ms, the ending time of the computation. The relatively moderate crushing of the M2A3 explosive fill appears to be nearly symmetrical about a line normal to the X axis and passing through the "top" of the explosive.

Computation DM2-24 simulated the same M2A3 munition being struck by the same flyer plate traveling at 24.0 m/s. There was an explosion in the corresponding experiment.[9] A total time of 6.00 ms was simulated. Because the flow field at the starting time of t = 0.00 is identical to that for DM2-15 except for the initial velocity of the flyer plate, it will not be shown. The flow field at 4.00 ms for computation DM2-24 is shown in Figure 5. The right interface of the explosive has already impacted upon the backing plate by this time and is showing a noticeable compressive distortion. By comparison, the explosive in DM2-15 had not yet reached the backing plate by this same time. Figure 6 shows the flow field at the ending time of 6.00 ms. It shows a greater amount of distortion of the explosive at this time than did DM2-15 at its ending time of 8.00 ms.

The flow field at time t = 0.00 for computation DM2-45 is not shown here because it is identical in appearance to that shown in Figure 1 except for the indicated velocity of the flyer plate. The impact velocity of the flyer plate in computation DM2-45 is 45.0 m/s. In the experiment [9] that this computation simulated, the impact caused a confirmed high-order detonation. Figure 7 shows the flow field at t = 4.00 ms. It shows considerably more compression of the explosive fill than is shown in either Figure 2 (flyer-plate velocity of 15.0 m/s) or Figure 5 (flyer-plate velocity of 24.0 m/s). Figure 8 shows the flow field at t = 6.00 ms, the ending time of the computation. The relatively large amount of compression of the explosive fill is evident at this time, especially in comparison with that shown in Figures 3 and 6 for flyer-plate velocities of 15.0 m/s and 24.0 m/s, respectively, at that same time.

Computation DM2-100 was run to simulate the impact of a flyer plate traveling at 100.0 m/s and striking the M2A3 in the same experimental configuration. There was no corresponding experiment. In the interest of brevity, no flow-field plots are shown. This computation was run for a total simulated time of 5.00 ms.

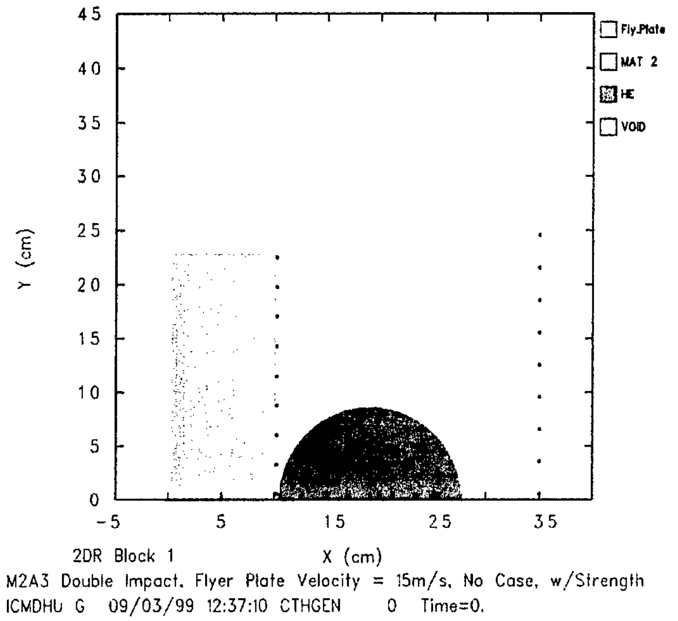

Figure 1. Flow Field at Time = 0.00 for Computation DM2-15, Double Impact of a Flyer Plate at 15.0 m/s With an M2A3 Munition.

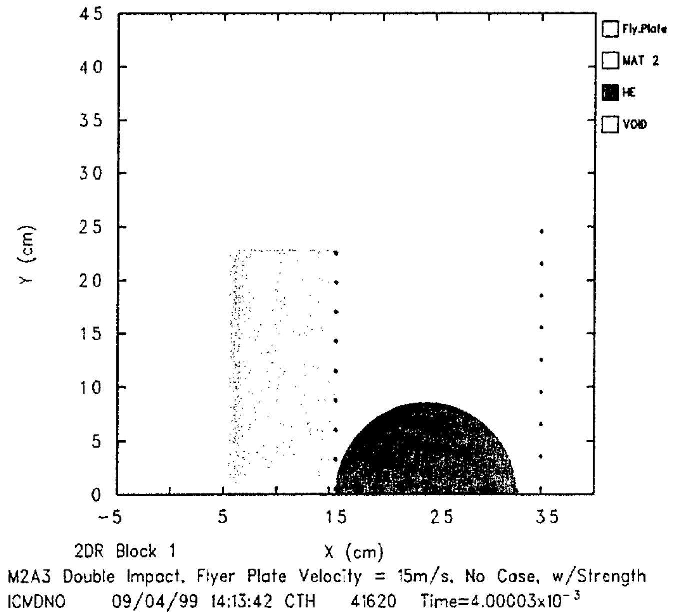

Figure 2. Flow Field at Time = 4.00 ms for Computation DM2-15, Double Impact of a Flyer Plate at 15.0 m/s With an M2A3 Munition.

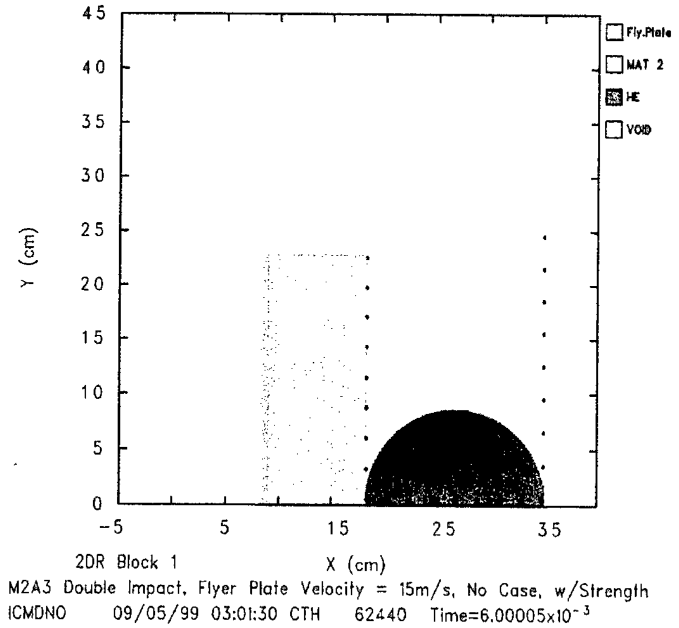

Figure 3. Flow Field at Time = 6.00 ms for Computation DM2-15, Double Impact of a Flyer Plate at 15.0 m/s With an M2A3 Munition.

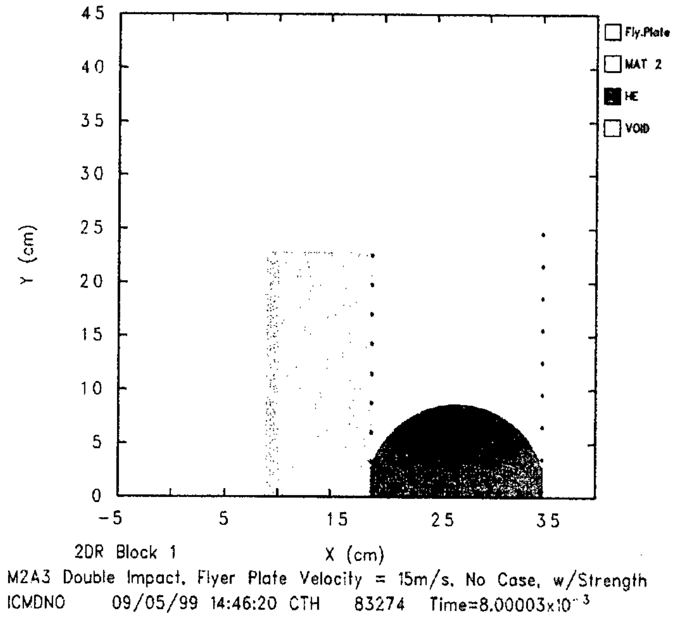

Figure 4. Flow Field at Time = 8.00 ms for Computation DM2-15, Double Impact of a Flyer Plate at 15.0 m/s With an M2A3 Munition.

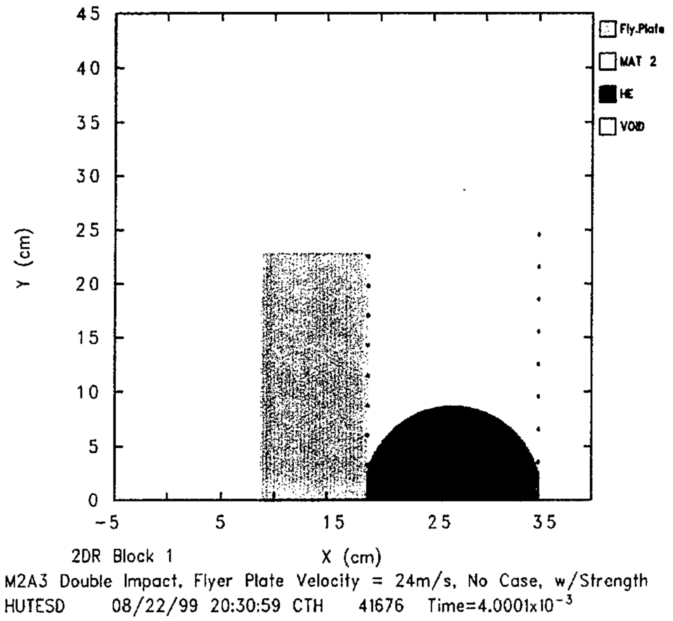

Figure 5. Flow Field at Time = 4.00 ms for Computation DM2-24, Double Impact of a Flyer Plate at 24.0 m/s With an M2A3 Munition.

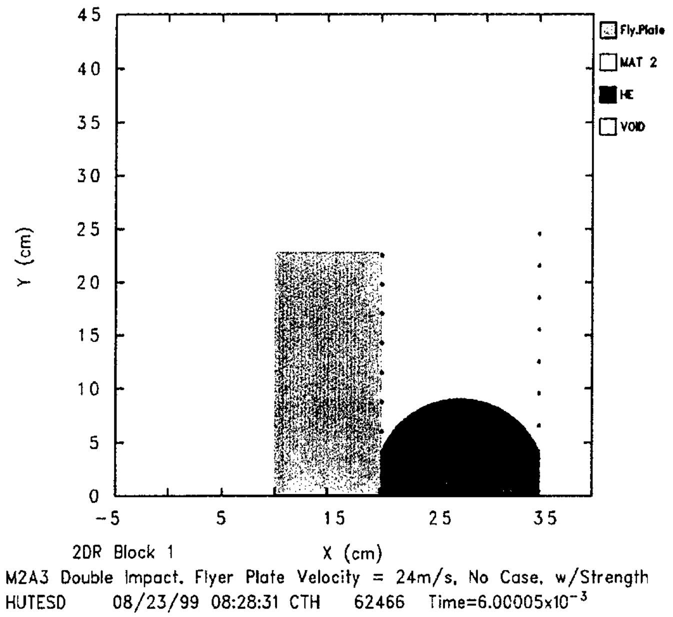

Figure 6. Flow Field at Time = 6.00 ms for Computation DM2-24, Double Impact of a Flyer Plate at 24.0 m/s With an M2A3 Munition.

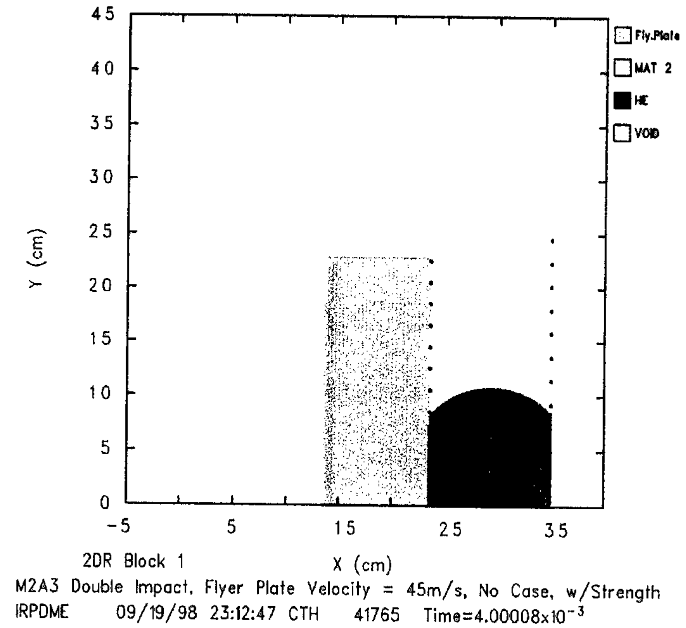

Figure 7. Flow Field at Time = 4.00 ms for Computation DM2-45, Double Impact of a Flyer Plate at 45.0 m/s With an M2A3 Munition.

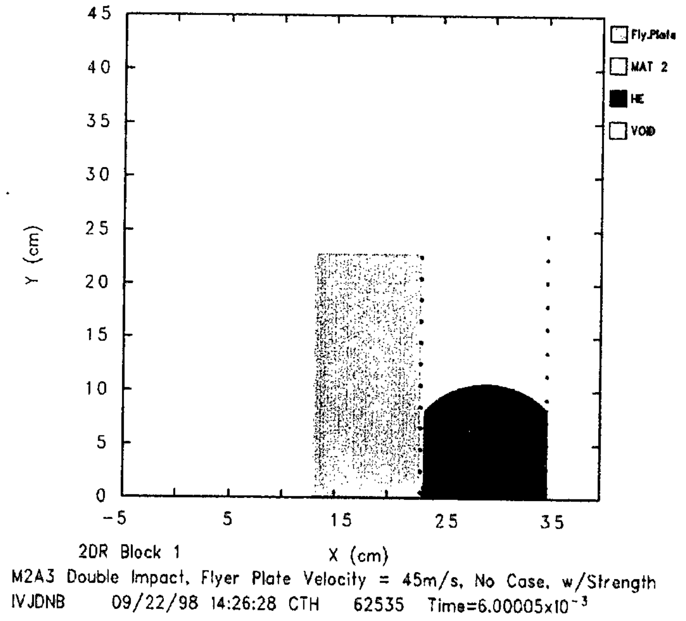

Figure 8. Flow Field at Time = 6.00 ms for Computation DM2-45, Double Impact of a Flyer Plate at 45.0 m/s With an M2A3 Munition.

4.2.2 Analysis of the Pressure in the Explosive Fills for the M2A3 Double-Impact Computation

Figure 9 shows the unsmoothed overpressure at each of three locations within the Comp-B explosive fill of the M2A3 munition for computation DM2-15. The overpressure is defined as the absolute value of pressure minus the ambient pressure (i.e., one atmosphere, or one bar of principal stress in the solid materials in these computations) at the start of the computation. Because the values of overpressure of interest here greatly exceed the initial pressure (i.e., initial principal stress), they are hereinafter simply referred to as "pressure," with the implicit understanding that they are actually values of overpressure. The plot of pressure for the first point in Figure 9 is identified in the legend as the red line labeled "Left Interface." That point is located just inside the left-most surface of the Comp-B (i.e., within one or two cells of the first computational cell completely filled with explosive) and just above (i.e., within one or two cells) the horizontal centerline of the M2A3 (see Figure 1). The data for the pressure at the second point, labeled "Center" with the green line, are taken at the center of the explosive fill, also just above the horizontal centerline. The blue line labeled "Right Interface" shows the pressure at a point that is just inside the right surface of the Comp-B and just above its horizontal centerline. The pressure near the left surface of the explosive fill begins to rise from its ambient level at approximately 0.14 ms. The 0.14-ms time span is the approximate transit time of the flyer plate across the void representing the thickness of the phenolic case of the M2A3. The pressure at this point increases to approximately 0.8 kbar in less than 0.5 ms and then decreases to a relatively low value during the translation of the explosive toward the backing plate. The pressure near that left surface experiences a second rapid increase starting at 5.8 ms, presumably from the arrival of a compression or shock wave that originates at the right surface upon its impact against the backing plate that occurs at approximately 5.67 ms. The peak pressure in the explosive fill near the right interface is higher (0.9 kbar) upon impact with the backing plate than the initial peak pressure near the left interface, but the highest pressure (1.05 kbar) during this 8.00-ms simulation actually occurs at the left interface after that impact. These pressure peaks are well above the assumed yield strength of 0.5 kbar of the Comp-B. Interestingly, the tracer at the center of the explosive fill never shows a strong compression wave and actually goes into moderate tension after 0.5 ms.

These unsmoothed pressure curves contain high-frequency components which, although they may contain useful data, at least partially mask some of the trends in the data, sometimes including the average ordinate value at any given time about which the data are oscillating. One of the many useful features in CTH's routine for plotting tracer data, HISPLT[2] [27] is a data-smoothing option that can filter out such high-frequency information. In Figure 10, the pressures have been smoothed with the parameter $\tau = 6.0x10^{-6}$, which is defined in the HISPLT user's

---

[2] not an acronym

manual along with the smoothing function that is used by HISPLT. While some of the various extrema in the smoothed plots are lower in absolute value than their counterparts in the unsmoothed plots, the essential features of the curves have been preserved and the underlying trends are now more readily seen. The reader is cautioned that considerable case-by-case experimentation with very small values of τ, relative to output plotting units, is apparently necessary if major trends in the data are to be preserved. With this in mind, the practice for this report will be to show both unsmoothed and smoothed pressure curves for each case on the same page, with the same plot size and scaling, to maximize the value of the presentation of the data.

Figure 11 shows the unsmoothed pressure at each of three locations within the Comp-B explosive fill of the M2A3 munition for computation DM2-24. In Figure 12, the pressures have been smoothed with the parameter $\tau = 5.0x10^{-6}$. The data for the points were plotted with the same choices of line color and identification in the legend as for computation DM2-15. The locations of the points were also the same. As was the case for DM2-15, the initial pressure peak at 0.2 ms near the left interface of the explosive is approximately 0.8 kbar, but the second peak at the left interface caused by the impact of the explosive on the backing plate at 3.65 ms is slightly lower than that for DM2-15 at about 0.9 kbar. The largest peak of 1.05 kbar occurs at 3.7 ms near the right interface. After the passage of an early compression wave, the center of the explosive fill is in tension for nearly all of the simulated time.

Figure 13 shows the unsmoothed pressure at each of three locations within the Comp-B explosive fill of the M2A3 munition for computation DM2-45. The pressure at the right interface indicates that the impact of the explosive on the backing plate occurs at 2.03 ms. In Figure 14, the pressures have been smoothed with the parameter $\tau = 7.0x10^{-6}$. The data for the points were plotted with the same choices of line color and identification in the legend as for computations DM2-15 and DM2-24. The locations of the points were also the same.

Figure 15 shows the unsmoothed pressure in the explosive fill for computation DM2-100, with the locations of the points and the choices of color for the plotted lines being the same as for the computations discussed previously. The greatest unsmoothed peak values of pressure are approximately 2.25 kbar. Figure 16 shows the same pressures as are shown in Figure 15, except that they have been smoothed with the parameter $\tau = 6.0x10^{-6}$. There is a strong oscillatory phase in pressure after 3.0 ms.

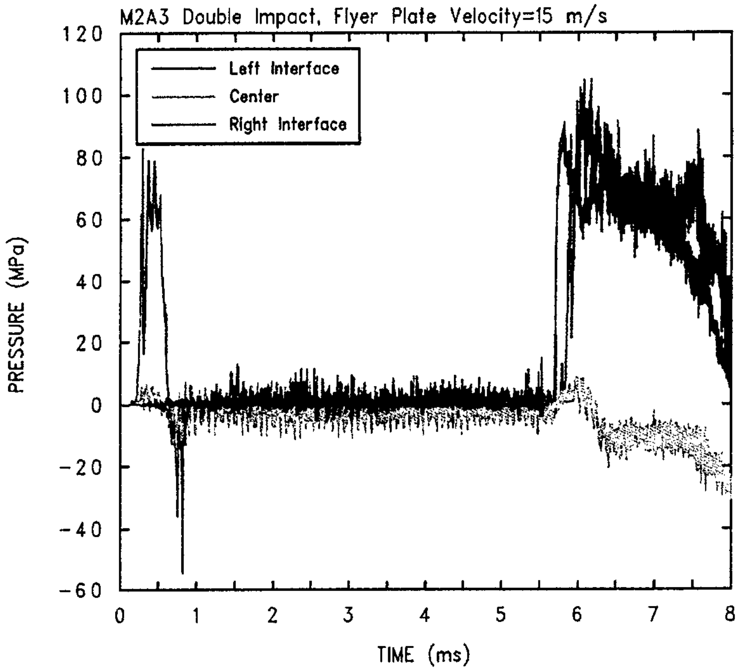

Figure 9. Pressure in the Unreacted Explosive Fill of the M2A3 Munition in Computation DM2-15 (unsmoothed).

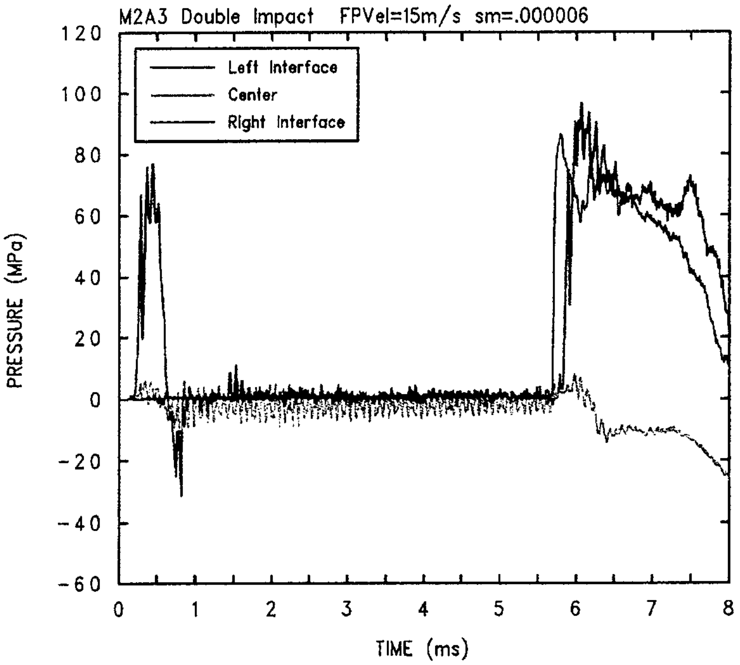

Figure 10. Pressure in the Unreacted Explosive Fill of the M2A3 Munition in Computation DM2-15 (smoothed).

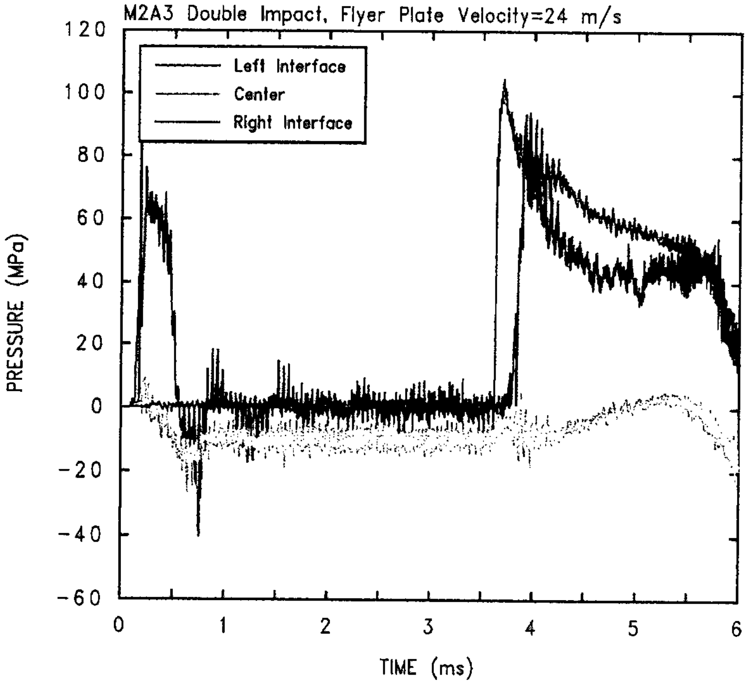

Figure 11. Pressure in the Unreacted Explosive Fill of the M2A3 Munition in Computation DM2-24 (unsmoothed).

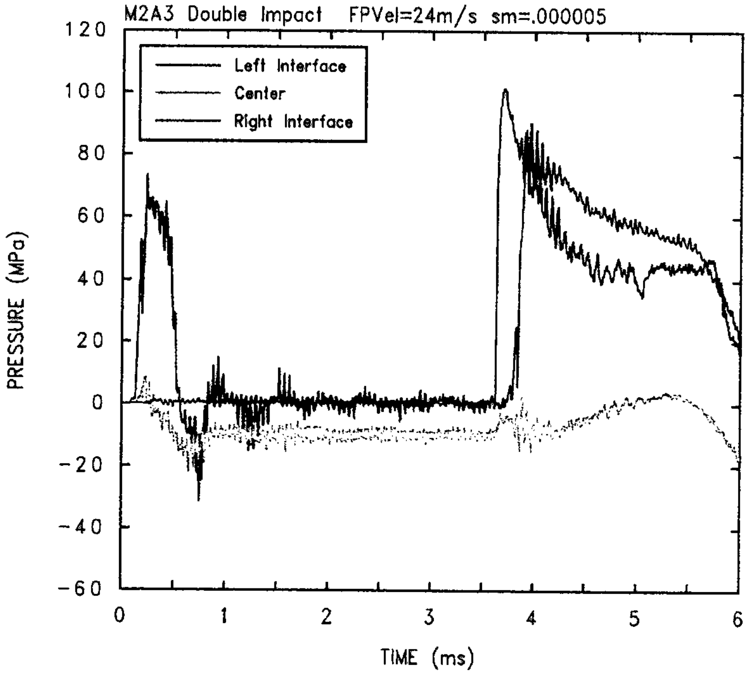

Figure 12. Pressure in the Unreacted Explosive Fill of the M2A3 Munition in Computation DM2-24 (smoothed).

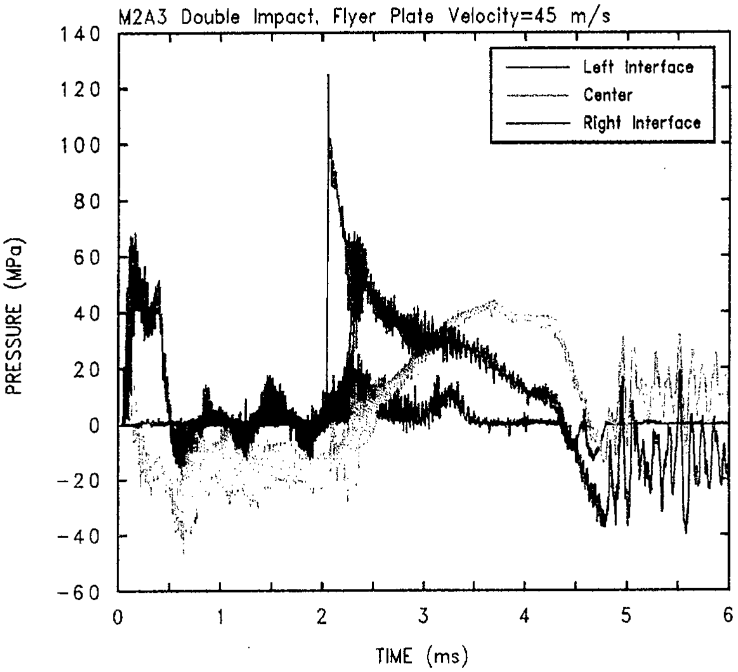

Figure 13. Pressure in the Unreacted Explosive Fill of the M2A3 Munition in Computation DM2-45 (unsmoothed).

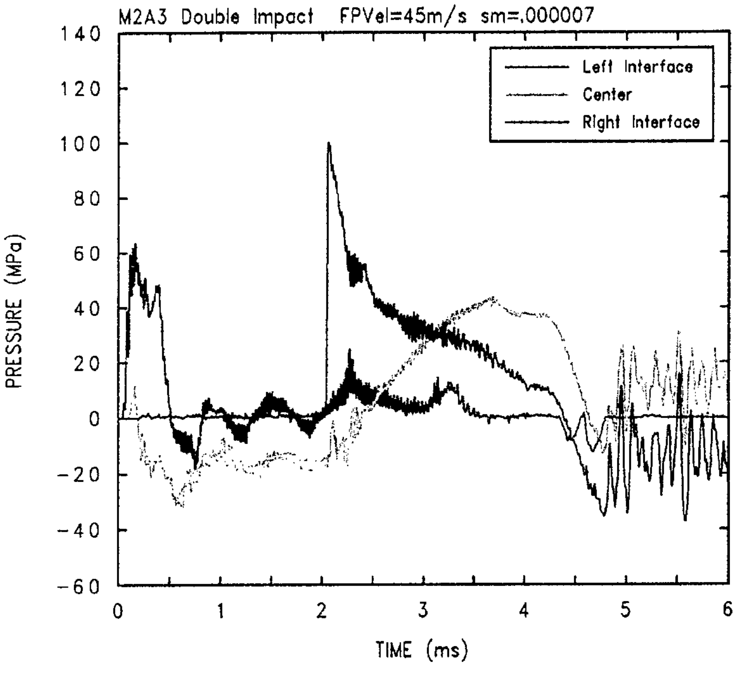

Figure 14. Pressure in the Unreacted Explosive Fill of the M2A3 Munition in Computation DM2-45 (smoothed).

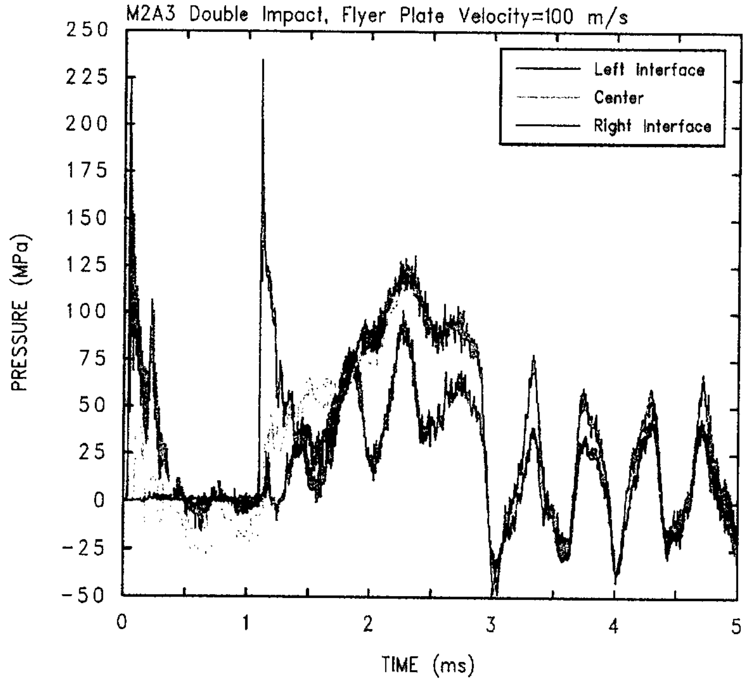

Figure 15. Pressure in the Unreacted Explosive Fill of the M2A3 Munition in Computation DM2-100 (unsmoothed).

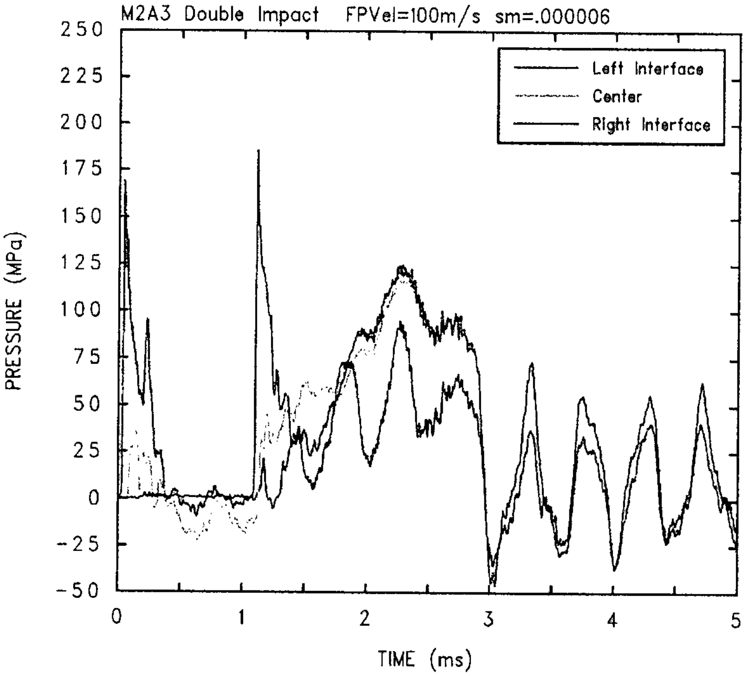

Figure 16. Pressure in the Unreacted Explosive Fill of the M2A3 Munition in Computation DM2-100 (smoothed).

4.2.3 Analysis of the Bulk Motion of the Explosive Fills for the M2A3 Double-Impact Computations

Figure 17 shows the X-direction momentum of the flyer plate and the X- and Y-direction momenta of the Comp-B explosive fill of the M2A3 munition versus time in Computation DM2-15. Figure 18 shows the X-direction velocity of the flyer plate and the X- and Y-direction velocities of the Comp-B explosive fill of the M2A3 munition. These velocities were computed by dividing the appropriate time-dependent momentum of the desired material by the mass of that material. Figure 19 shows the X-direction acceleration of the flyer plate and the X- and Y-direction accelerations of the Comp-B explosive fill of the M2A3 munition. These accelerations were computed by piece-wise differentiation of the respective velocities computed from the momentum for the respective materials over time. Together, these three figures show the initial transfer of the X-direction momentum of the flyer plate to the explosive, with most of that initial transfer going into the X-direction momentum of the explosive. The early part of this initial momentum transfer into the explosive appears to involve a relatively high increase in the shear, pressure, and internal energy in a comparatively small unit mass of explosive at the impact point. Both the flyer plate and the explosive show a period of several milliseconds of nearly constant X-direction velocity of 13.4 m/s prior to the impact of the explosive on the backing plate at 5.6 ms. After that time, the X-direction momentum of the explosive and the much greater remaining X-direction momentum of the flyer plate are largely dissipated in the explosive by some combination of increases in body-force and thermodynamic parameters such as shear, pressure, and internal energy within the explosive, apparently on a broad spatial scale. Some indicative examples are provided later in this report. With much finer grid resolution and greatly improved material strength and failure models, the distributions of shear and internal energy would very likely be quite differentiated, particularly at high impact velocities. Such a refined analysis is not possible at present.

The explosive shows a peak X-direction acceleration of about -57.6 km/s^2 (i.e., a deceleration) at 5.8 ms. The flyer plate shows a considerably milder X-direction deceleration of -12.0 km/s^2 at 6.2 ms. Even though the accelerations have the appearance of being mostly noise, possibly some of it numerical, the largest of the Y-direction accelerations of the explosive are interesting in that they are numerous and of comparable magnitude to the largest X-direction accelerations in both range and value. Because the acceleration data are derived directly from the bulk momentum of the explosive fill in all computational cells in this one-half symmetry region, there is a good argument for a conclusion that it is not simply a manifestation of numerical noise. If the existence of these oscillations can be confirmed via experiment, they may be an indicator of a cumulative damage process that could lead to initiation beyond some combination of frequency and amplitude.

Figure 20 shows the X-direction momentum of the flyer plate and the X- and Y-direction momenta of the Comp-B explosive fill of the M2A3 munition versus time in computation DM2-24. The figure shows the same type of multi-stage delivery and conversion of momentum of the flyer plate into the explosive. This occurs initially as a relatively small transfer of X-direction momentum and later as a transformation of flyer-plate momentum into body forces and thermodynamic-state parameters such as shear, internal energy, and pressure in the explosive. The timing of the transfers occurs at a faster rate because of the greater impact velocity of the flyer plate. Figure 21 shows the X-direction velocity of the flyer plate and the X- and Y-direction velocities of the Comp-B explosive fill of the M2A3 munition. These velocities were computed from the appropriate momentum of the desired material as before. Figure 22 shows the X-direction acceleration of the flyer plate and the X- and Y-direction accelerations of the Comp-B explosive fill of the M2A3 munition. After the initial transfer of momentum from the flyer plate to the explosive, the flyer plate then moves at a nearly constant velocity of 21.4 m/s for approximately 3.0 ms before its final deceleration upon the impact of the explosive fill against the backing plate. The X-direction velocity of the explosive fill shows damped oscillation about that same value during that time. The acceleration data show not only the moderate, distinct X-direction acceleration minima and maxima as for DM2-15 but also the same type of interesting high-frequency Y-direction accelerations over about half of the absolute range of the X-direction accelerations.

Figure 23 shows the X-direction momentum of the flyer plate and the X- and Y-direction momenta of the Comp-B explosive fill of the M2A3 munition versus time in computation DM2-45. Figure 24 shows the X-direction velocity of the flyer plate and the X- and Y-direction velocities of the Comp-B explosive fill of the M2A3 munition. These velocities were computed from the appropriate momentum of the desired material as before. Figure 25 shows the X-direction acceleration of the flyer plate and the X- and Y-direction accelerations of the Comp-B explosive fill of the M2A3 munition.

The strong oscillatory phase in pressure for computation DM2-100, which can be seen in Figures 15 and 16, corresponds to a similar oscillatory phase in the bulk X-direction velocity of the flyer plate, shown as the blue line in Figure 26. Also shown in Figure 26 are the flyer-plate velocities for computations DM2-15, DM2-24, and DM2-45. These were discussed earlier in this section, but it is informative to plot them together in this way. All of the plots show a similar multi-stage decrease in X-direction velocity of the flyer plate to either a negative-velocity rebound stage or an oscillatory stage. Figure 27 shows a similar set of plots of the bulk X-direction velocity of the explosive fill for each of the four computations. There is an interesting trend in the respective peak velocities for the computations. The peak velocities are 20.4 m/s for DM2-15 (1.36 times the impact velocity of the flyer plate), 30.0 m/s for DM2-24 (1.25 times the impact velocity of the flyer plate), 51.8 m/s for DM2-45 (1.15 times the impact velocity of the flyer plate), and 98.2 m/s for DM2-100 (0.98 times the impact velocity of the flyer plate). Finally, Figure 28 shows the bulk Y-direction velocities of the explosive fill for each of the double-impact computations. Taken together, these three figures show a composite view of the similar, multi-stage processes by which the initial X-direction velocity (actually momentum) of the flyer plate is transformed in the explosive fill, primarily in the forms of pressure, internal energy, and shear. The issue of evaluating the sensitivity of this process of energy transfer to the explosive from the flyer plate to better modeling of the material properties of the explosive was not addressed. It is unquestionably important.

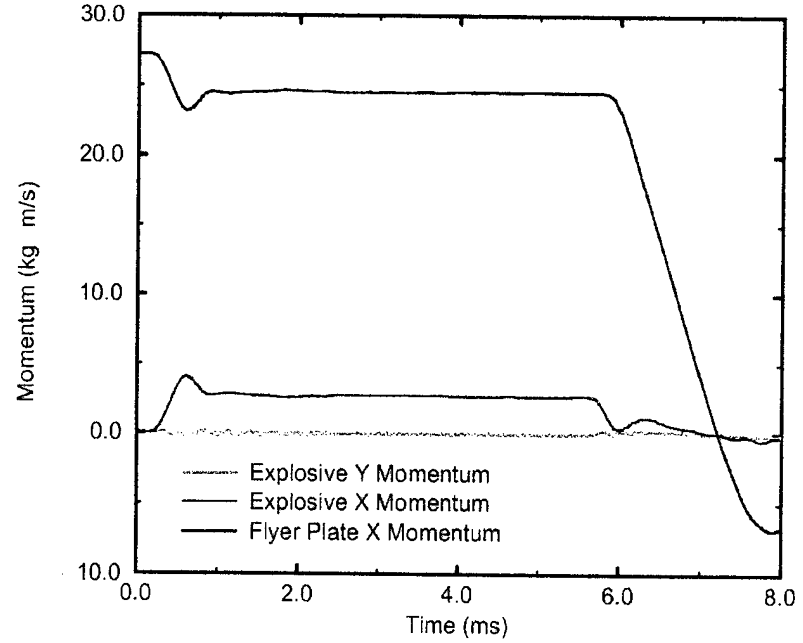

Figure 17. Momenta of the Flyer Plate and the Unreacted Explosive Fill of the M2A3 Munition in Computation DM2-15.

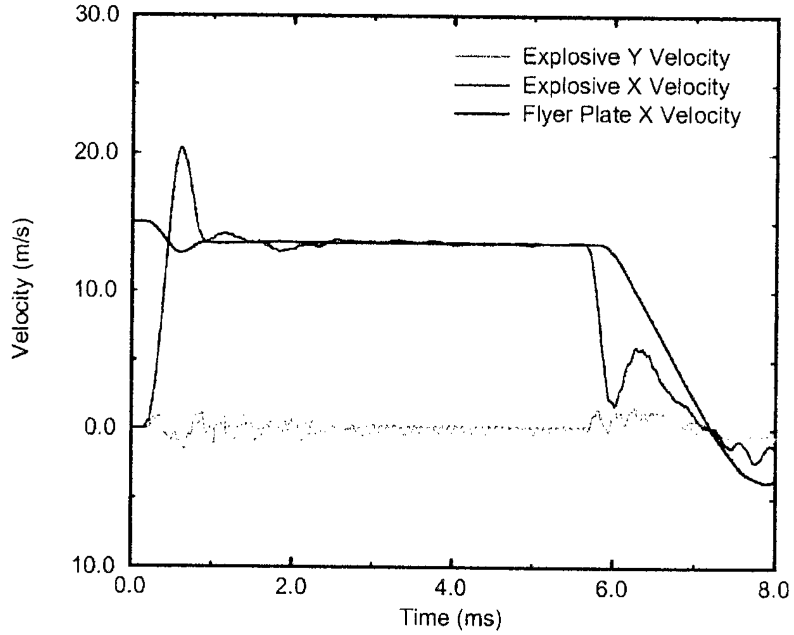

Figure 18. Velocities of the Flyer Plate and the Unreacted Explosive Fill of the M2A3 Munition in Computation DM2-15.

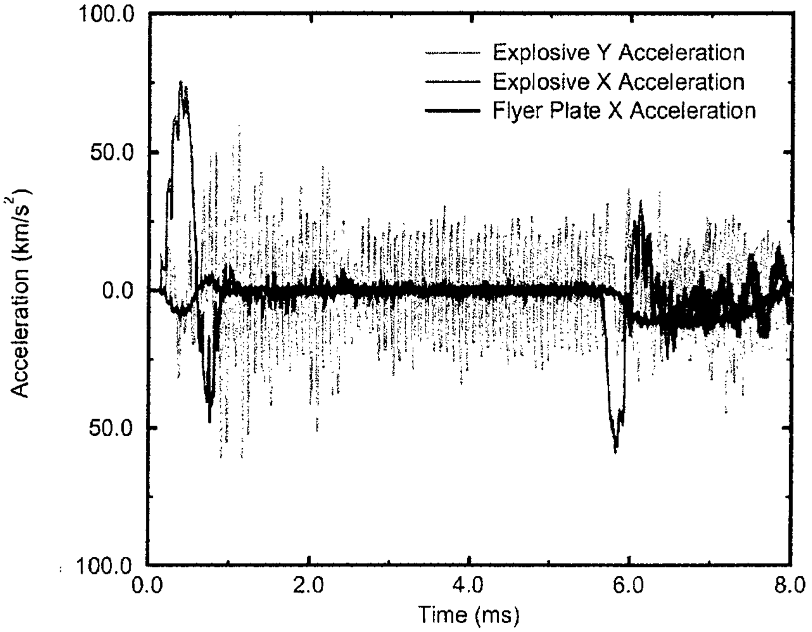

Figure 19. Accelerations of the Flyer Plate and the Unreacted Explosive Fill of the M2A3 Munition in Computation DM2-15.

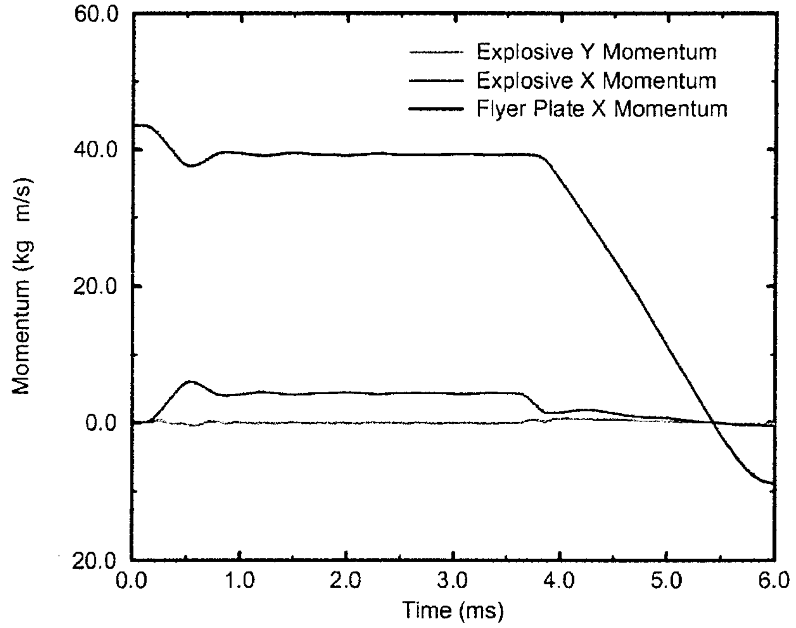

Figure 20. Momenta of the Flyer Plate and the Unreacted Explosive Fill of the M2A3 Munition in Computation DM2-24.

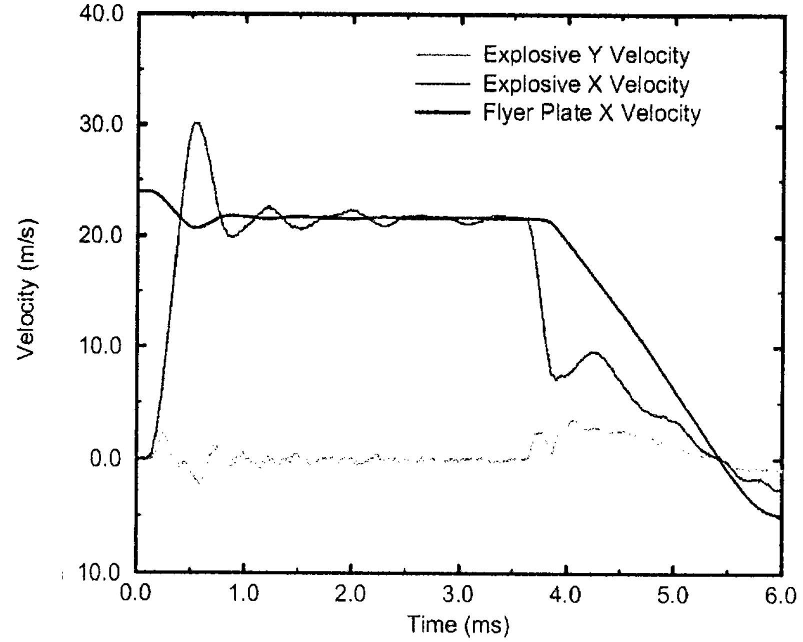

Figure 21. Velocities of the Flyer Plate and the Unreacted Explosive Fill of the M2A3 Munition in Computation DM2-24.

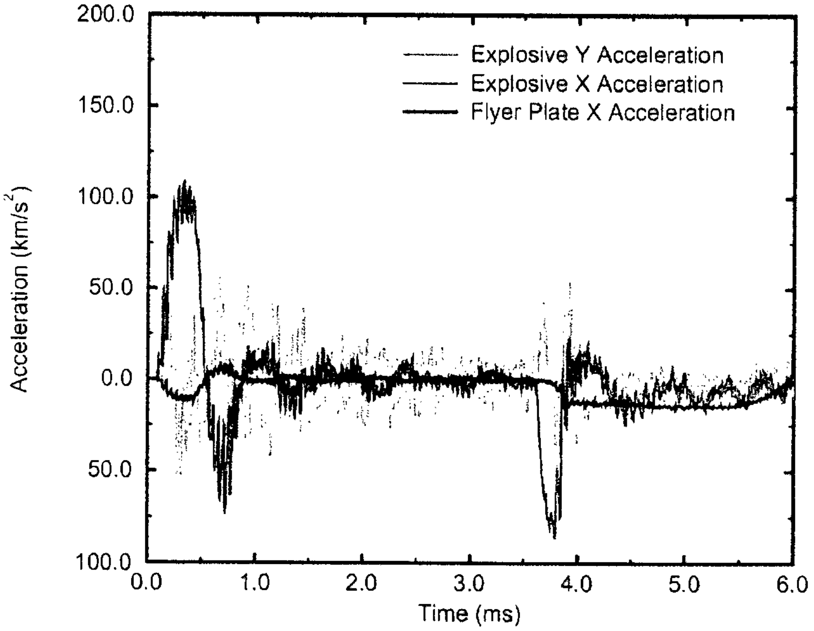

Figure 22. Accelerations of the Flyer Plate and the Unreacted Explosive Fill of the M2A3 Munition in Computation DM2-24.

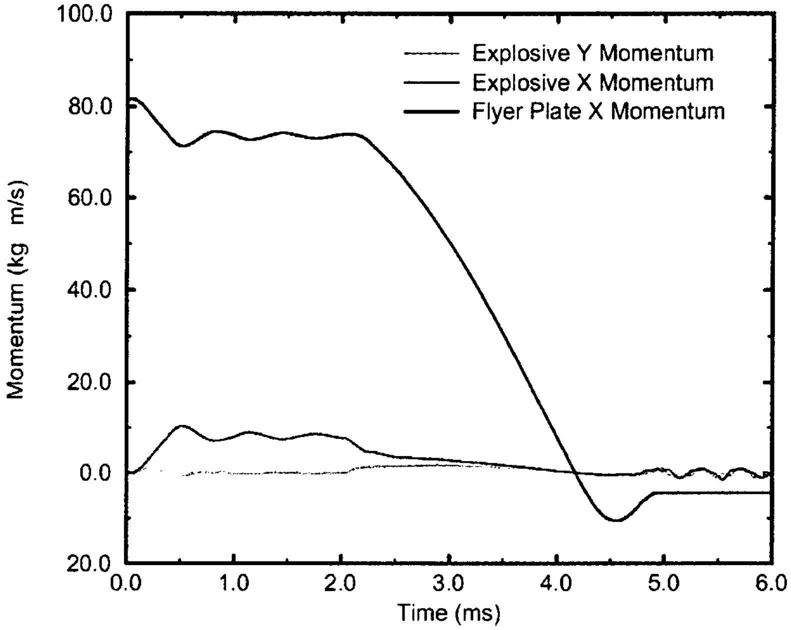

Figure 23. Momenta of the Flyer Plate and the Unreacted Explosive Fill of the M2A3 Munition in Computation DM2-45.

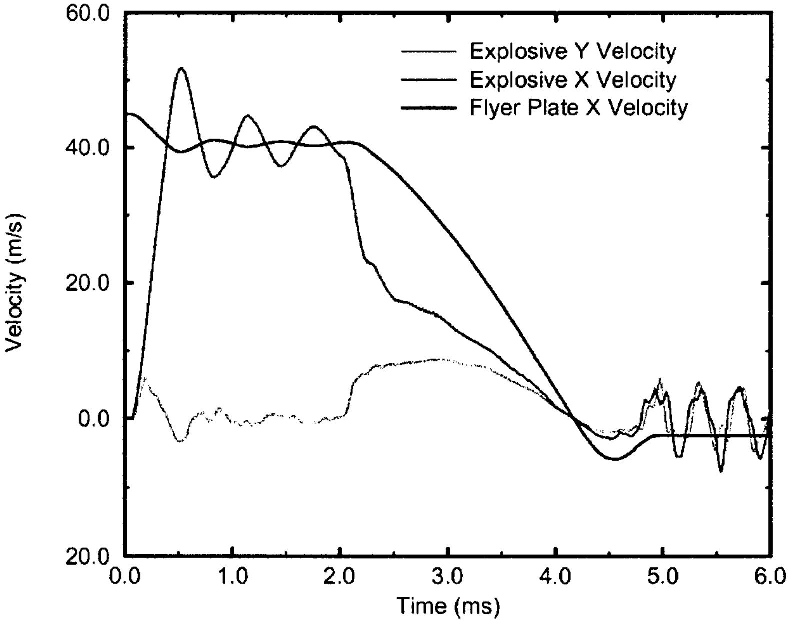

Figure 24. Velocities of the Flyer Plate and the Unreacted Explosive Fill of the M2A3 Munition in Computation DM2-45.

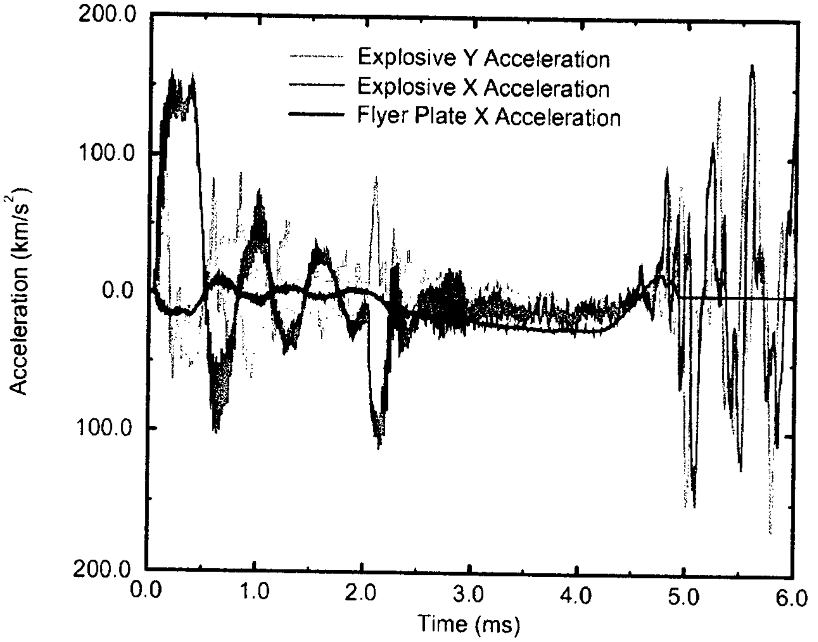

Figure 25. Accelerations of the Flyer Plate and the Unreacted Explosive Fill of the M2A3 Munition in Computation DM2-45.

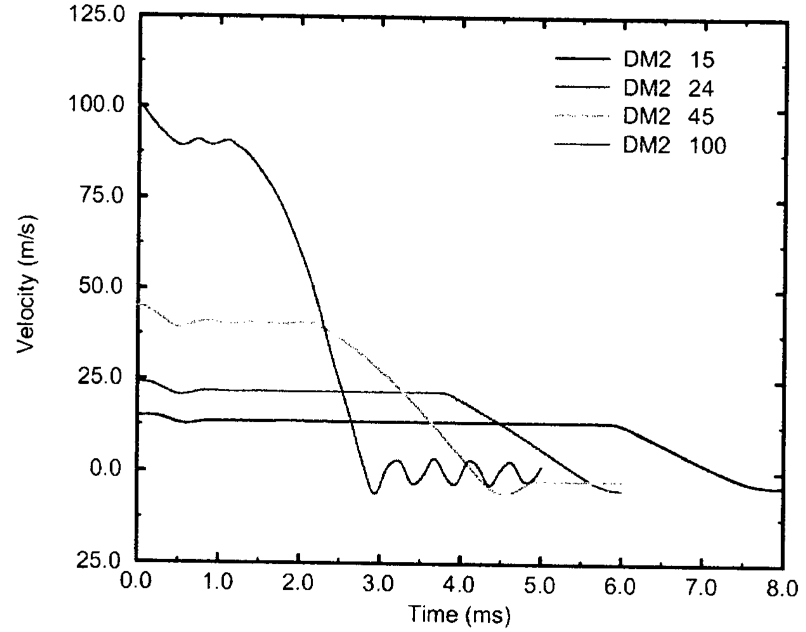

Figure 26. X-Direction Velocities of the Flyer Plate for Each of the Double-Impact Computations for the M2A3 Munition.

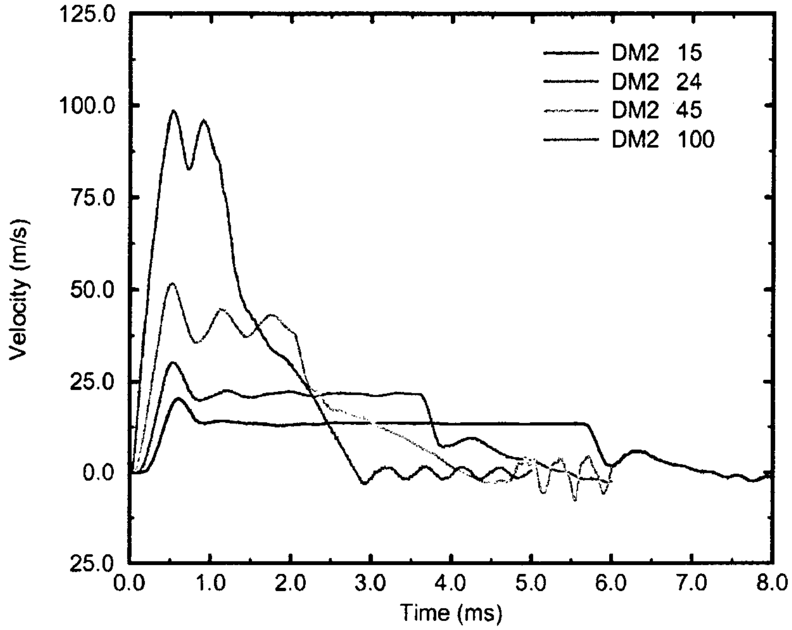

Figure 27. X-Direction Velocities of the Explosive Fill of the M2A3 Munition for Each of the Double-Impact Computations.

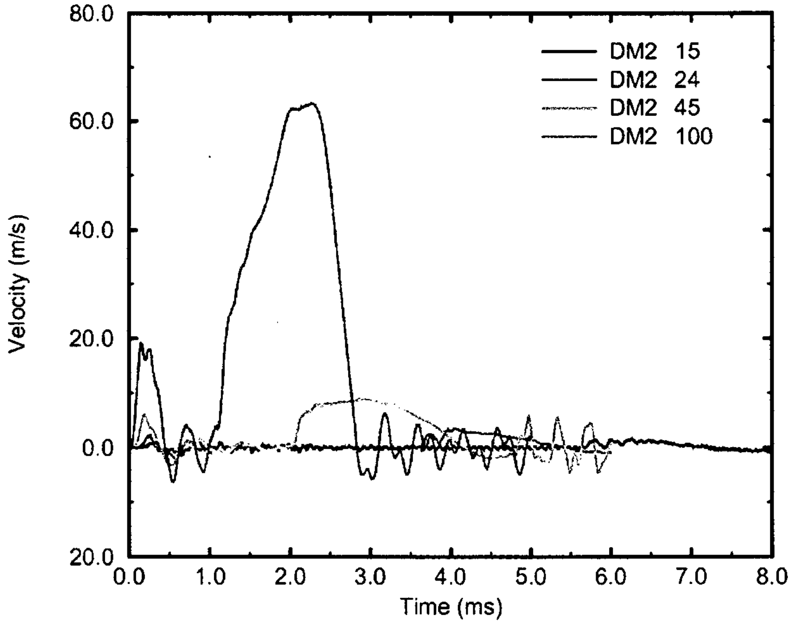

Figure 28. Y-Direction Velocities of the Explosive Fill of the M2A3 Munition for Each of the Double-Impact Computations.

4.2.4 Analysis of Shear and Other Parameters for Selected M2A3 Double-Impact Computations

Computation DM2-45 simulates the only experiment [9] of those discussed herein in which a confirmed high-order detonation occurred. The peak values of the computed shock pressures are relatively low in comparison with the levels suggested by Liddiard and Forbes [1] for direct shock initiation. Therefore, it is instructive to add a brief discussion of parameters related to possible shear initiation but with the caution that the resolution of the computational grid in DM2-45 is too coarse to allow a definitive analysis. Three parameters measuring the dynamics in the undetonated explosive are discussed here, but they are not the only parameters relevant to shear initiation. The first is the hydrostatic pressure (i.e., the values of pressure discussed throughout this report), also referred to as the spherical stress.[28] The second is the maximum principal stress. This is the greatest value of the principal stress components that are computed for an isotropic material when a set of orthogonal axes is rotated so that all deviatoric stress components are equal to zero.[28] The third is the functional relationship of the flow velocity in the vertical (i.e., Y) direction along spatial cuts through the undetonated explosive. The spatial cuts are parallel to the Y axis (i.e., along a range of Y values at a given fixed value of X).

It appears that, as far as pressure and maximum principal stress are concerned, the most intense activity is at the initial impact point of the flyer plate on the explosive fill. The activity is slightly less intense at the impact point of the explosive fill on the backing plate. Some examples that illustrate that activity are shown in the following figures. These examples and the related discussion do not constitute a full technical analysis. Figure 29 shows the pressure in the explosive fill at t = 0.10 ms, just after the initial impact of the flyer plate on the explosive fill. This shows the greatest pressure peak in the explosive fill from all of the flow-field "restart dumps" (i.e., complete numerical records of the flow field from which the computation could be restarted), which were done at intervals of 0.05 ms of simulated time. This peak, approximately 143 MPa (1.43 kbar), occurred in the computational cell(s) at the extreme lower left edge of the now-deforming explosive fill. This is a highly localized pressure peak. The resultant compression waves, which are considerably weaker than this peak value, are still diverging and moving across the explosive fill. This is not necessarily the greatest pressure computed anywhere in the explosive over the entire range of the simulated time. The range of values chosen for the continuous color bands, shown at the right of the figure in units of dynes per square centimeter, is based on a combination of two criteria. The first is an objective criterion of determining the greatest and smallest numerical values of pressure found by searching through all of the restart dumps. The second is a subjective criterion of selecting the upper and lower values for the color bands, slightly within the objective extrema, so that the gradations of color that are presented can convey a reasonable impression of the dynamic nature of the gradients in the flow field. Thus, the scale for the color bands also includes a white band for an off-scale minimum and a black band for an off-scale maximum. This is particularly useful in avoiding the suppression of the color-band values at the high end of the scale because the extreme values were typically of very limited spatial and temporal extent. There is an inevitable loss of information because of the selection of pixel density and the standard printing process for this report in a figure such as Figure 29. Assigning the most intense red value to the exact value of the greatest pressure peak has the unintended effect of suppressing the high-level color bands.

Figure 30 shows the Y-direction velocity in the explosive fill at this same time. The range of values for the color bands of velocity was chosen with the same logic as for the pressure bands just discussed. It can be readily seen that the peak Y velocities at the left-most edge of the explosive at this time, which occur at about 7.1 m/s, are considerably less than the greatest found over all of the simulated time. A computation performed with finer zoning and better constitutive models would be expected to show different results, quite possibly including greater peaks in both pressure and velocity. The case could easily be made for making comparative computations with either a purely Lagrangian hydrocode or an arbitrary Lagrangian-Eulerian (ALE) hydrocode. Perhaps that should be done in a future study.

Figure 31 shows the pressure field in the explosive fill at t = 0.15 ms, the time of the next restart dump. The scale of the color band at the right of the figure is identical to that for Figure 29 and not specifically scaled to the pressure field at 0.15 ms. The peak pressure at this time is 117 MPa (1.17 kbar), still at the left-most edge of the explosive but now at approximately Y = 1.5 cm. The leading edge of the pressure wave is now close to the right-most lower edge of the explosive. Figure 32 shows the corresponding Y-velocity field at that same time.

Figure 33 shows a temporal sequence of values of pressure, exclusively in the explosive, along a spatial cut through the explosive and parallel to the Y axis at a constant value of X = 10.95 cm. The spatial cuts are taken from all of the restart dumps, ranging from t = 0.00 to t = 0.25 ms, inclusively, at 0.05-ms intervals. In the legend, the symbol "(*)" at the right indicates that the particular line was completely overwritten by the line for t = 0.25 ms. This captures the passages of both the shock from the initial impact of the flyer plate and then the passage of the right-most edge of the flyer plate itself. The plot of ambient pressure in the explosive at t = 0.0 appears to be a completely overwritten line at essentially zero simply because of the large scale of the plot ordinate for pressure. The very small increase in pressure near Y = 0.00 at t = 0.05 ms shows the beginning of the passage of the computational pressure wave. The greatest peak value is at Y = 0.00 at t = 0.10 ms, shown by the green line. By t = 0.15 ms, the shock front has already passed the spatial cut position at X = 10.95 cm, as can be seen in the lesser peak for the dark blue line. By t = 0.20 ms, the shock has passed by entirely, and the orange line for the pressure appears to be essentially zero, as does the magenta line for t = 0.25 ms. As yet, no discernible negative pressure (i.e., tension) has developed along this spatial cut. Figure 34 presents a corresponding set of spatial cuts of Y-direction velocity along the same range of Y at the same X = 10.95-cm location and the same times. Only the plots for t = 0.10 ms and t = 0.15 ms show any significant values of Y velocity. The greatest positive Y velocity at the left-most edge of the explosive fill (see Figures 30 and 32) is 21.1 m/s. The greatest negative Y velocity at that edge is -18.4 m/s. The change from the greatest positive to the greatest negative value occurs over a change in Y of 0.10 cm, indicating a region of relatively large velocity gradients even with this coarse grid resolution.

In order to provide some insight into the development of the relative magnitudes of the deviatoric stress components of the stress tensors, the fields of the maximum principal stresses in the explosive fill are shown in Figure 35 at t = 0.10 ms and in Figure 36 for t = 0.15 ms. As would be expected, the peak values are somewhat greater than the respective peaks in pressure because of the contribution from the non-zero deviatoric stresses in the X-Y set of axes to the orthogonal set within which there are only principal stresses. Figure 37 shows spatial cuts in the Y direction at X = 10.95 cm of maximum principal stress. It shows moderately higher peaks (168 MPa [1.68 kbar] at t = 0.10 ms and 150 MPa [1.50 kbar] at t = 0.15 ms) than are shown in Figure 33 for pressure at the corresponding times.

The temporally coincident values of pressure and Y velocity in the time span of 0.10 ms to 0.15 ms shown in Figures 33 and 34, respectively, are smaller than the values for initiation by shearing suggested by Liddiard and Forbes.[1] However, this region within the explosive fill was the one that showed concurrently high values of each. As stated before, a computation with much better grid resolution, constitutive models, and strength parameters might show very interesting results that could very well include greater extrema in the local values of stress and velocity. This was the one experiment of all those simulated here that resulted in a confirmed high-order detonation, but neither the time of the initiation of the detonation relative to the time of impact nor the location within the explosive was recorded. The simple, incomplete analysis in this section provides only a suggestion of its possible causative agent and point of initiation in space and time.

Computation DM2-24 simulated the same experimental configuration as did DM2-45, except the velocity of the flyer plate in both the experiment and in DM2-24 was 24.0 m/s. The experiment resulted in an explosion. The same discussion regarding the inadequacy of the grid resolution for DM2-45 is also directly relevant to DM2-24. The pressures and values of Y-direction velocity in the explosive fill for DM2-24 were examined. The most significant combined activity for these two parameters was also near the point of the initial impact of the flyer plate against the explosive fill of the M2A3. Figure 38 shows the most significant Y-direction spatial cuts of pressure at the constant X = 10.95-cm location. The greatest values are approximately 90 MPa (0.9 kbar) at 0.25 ms. In the legend, the symbol "(*)" at the right indicates that the particular line was completely overwritten by the line for t = 0.40 ms. Figure 39 shows the corresponding values of the Y-direction velocity, with the plot for 0.25 ms showing the greatest peak value of approximately 10 m/s. Figures 40 and 41 show similar plots of pressure and Y-direction velocity, respectively, for the same times at spatial cuts along a constant X = 11.06-cm location.

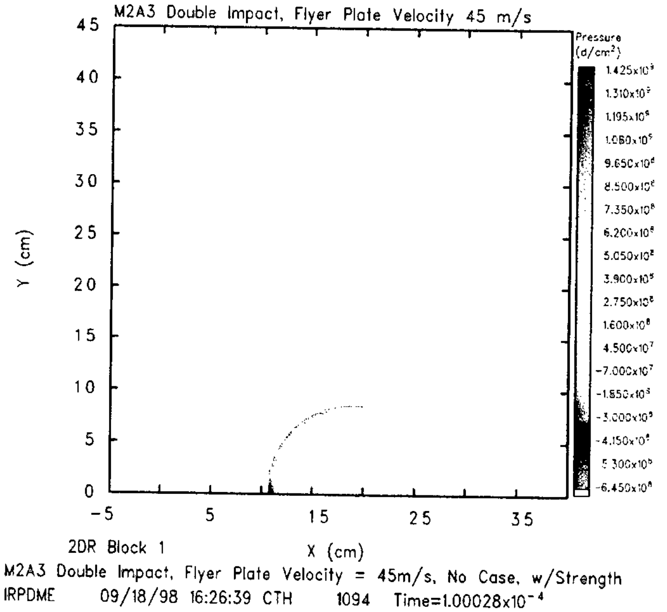

Figure 29. Explosive Hydrostatic Pressure at Time = 0.10 ms for Computation DM2-45, Double Impact of a Flyer Plate at 45.0 m/s With an M2A3 Munition.

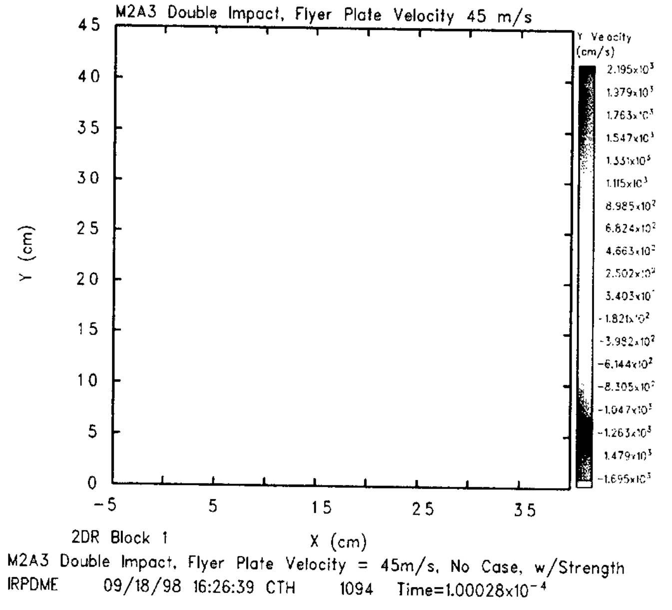

Figure 30. Explosive Y-Direction Velocity at Time = 0.10 ms for Computation DM2-45, Double Impact of a Flyer Plate at 45.0 m/s With an M2A3 Munition.

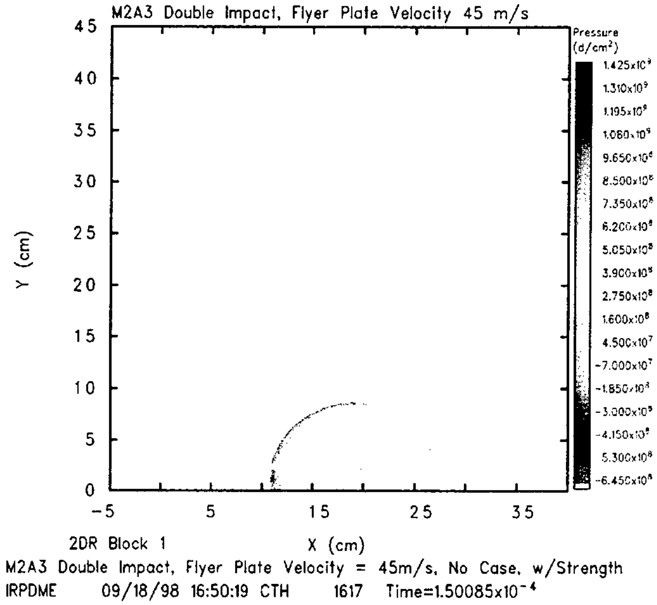

Figure 31. Explosive Hydrostatic Pressure at Time = 0.15 ms for Computation DM2-45, Double Impact of a Flyer Plate at 45.0 m/s With an M2A3 Munition.

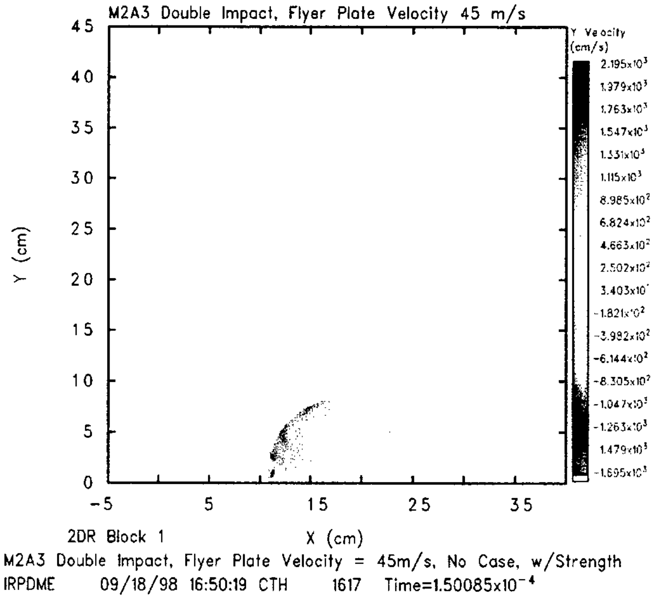

Figure 32. Explosive Y-Direction Velocity at Time = 0.15 ms for Computation DM2-45, Double Impact of a Flyer Plate at 45.0 m/s With an M2A3 Munition.

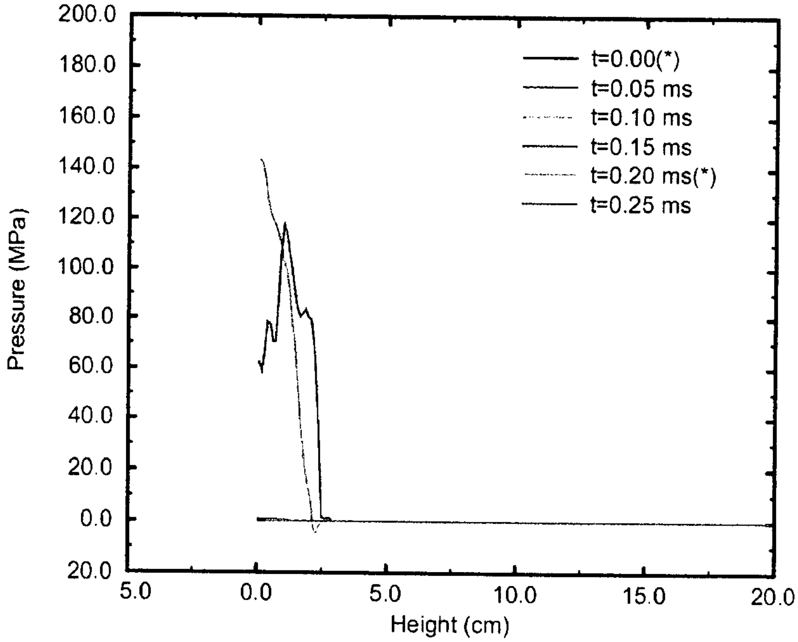

Figure 33. Y-Direction Spatial Cuts of Hydrostatic Pressure at X = 10.95 cm in the Explosive Fill of the M2A3 Munition in Computation DM2-45.

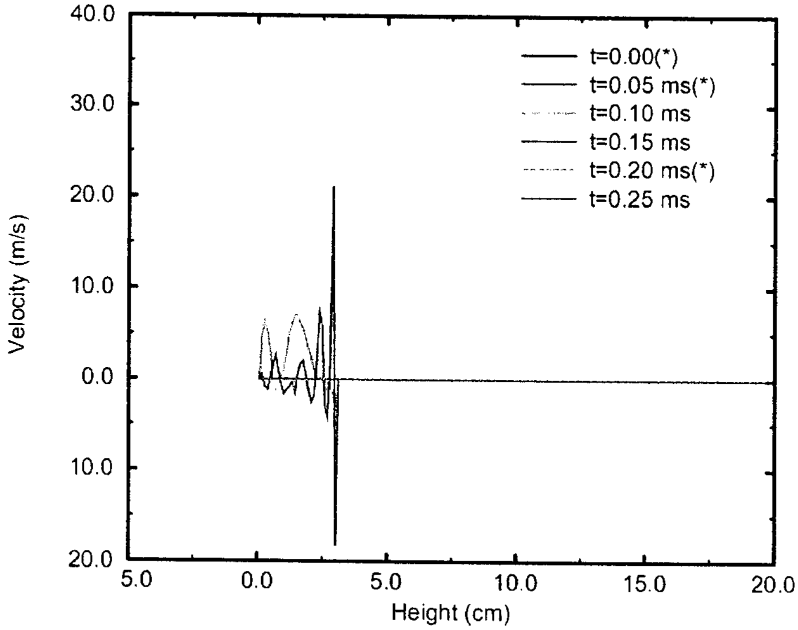

Figure 34. Y-Direction Spatial Cuts of Y-Direction Velocity at X = 10.95 cm in the Explosive Fill of the M2A3 Munition in Computation DM2-45.

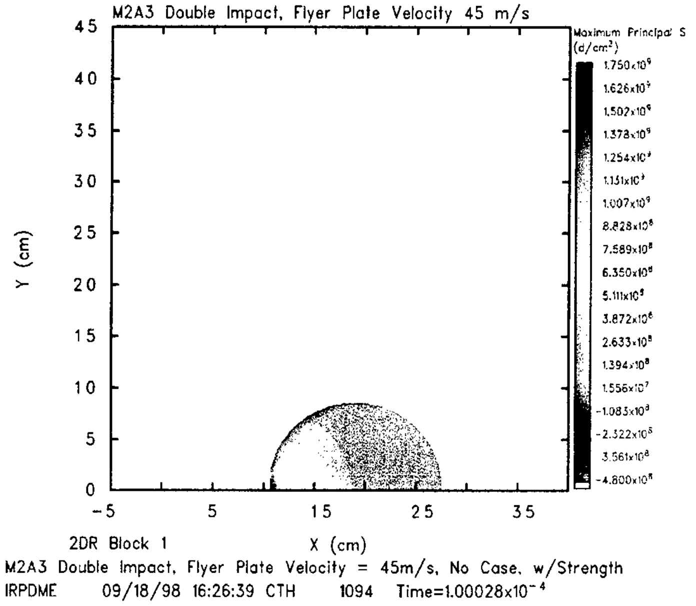

Figure 35. Explosive Maximum Principal Stress at Time = 0.10 ms for Computation DM2-45, Double Impact of a Flyer Plate at 45.0 m/s With an M2A3 Munition.

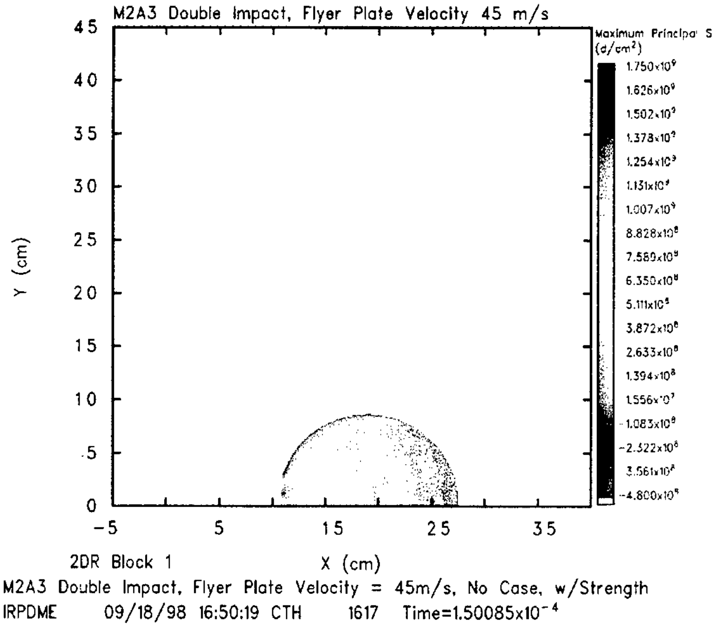

Figure 36. Explosive Maximum Principal Stress at Time = 0.15 ms for Computation DM2-45, Double Impact of a Flyer Plate at 45.0 m/s With an M2A3 Munition.

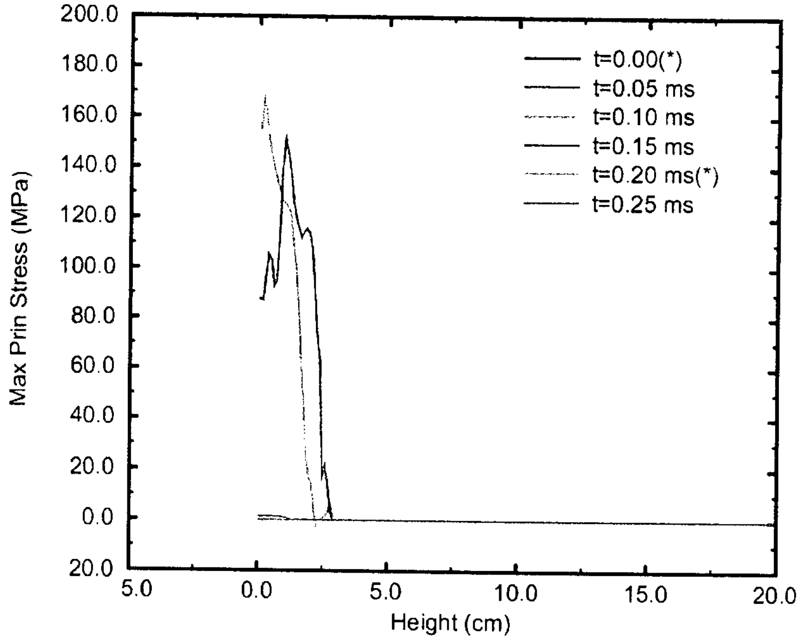

Figure 37. Y-Direction Spatial Cuts of Maximum Principal Stress at X = 10.95 cm in the Explosive Fill of the M2A3 Munition in Computation DM2-45.

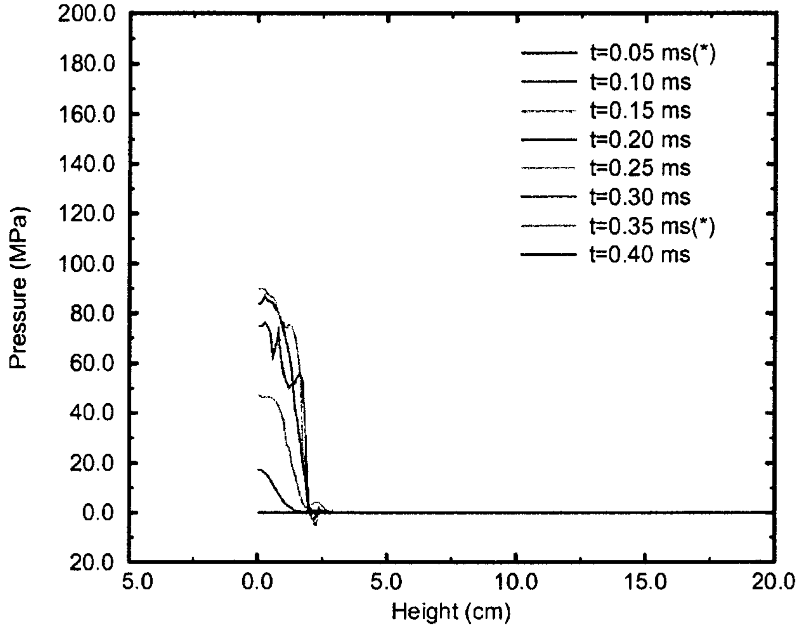

Figure 38. Y-Direction Spatial Cuts of Hydrostatic Pressure at X = 10.95 cm in the Explosive Fill of the M2A3 Munition in Computation DM2-24.

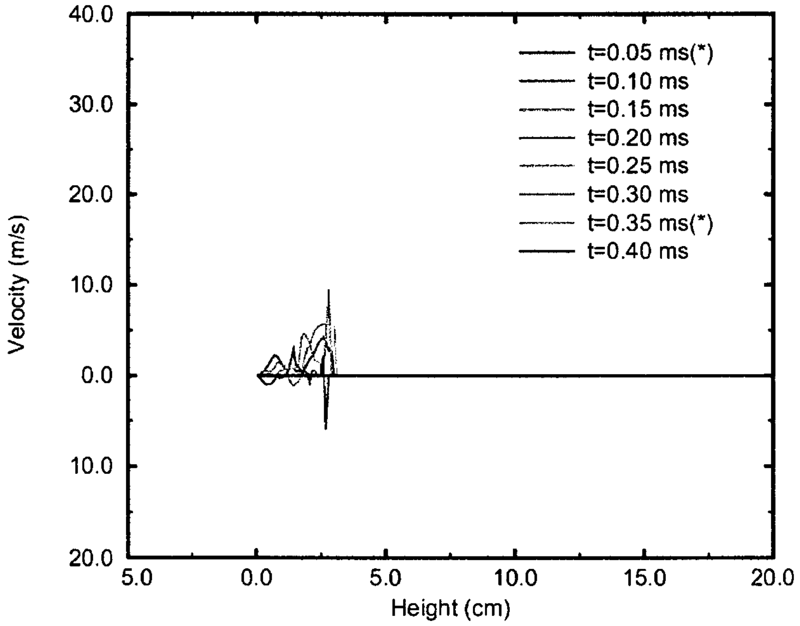

Figure 39. Y-Direction Spatial Cuts of Y-Direction Velocity at X = 10.95 cm in the Explosive Fill of the M2A3 Munition in Computation DM2-24.

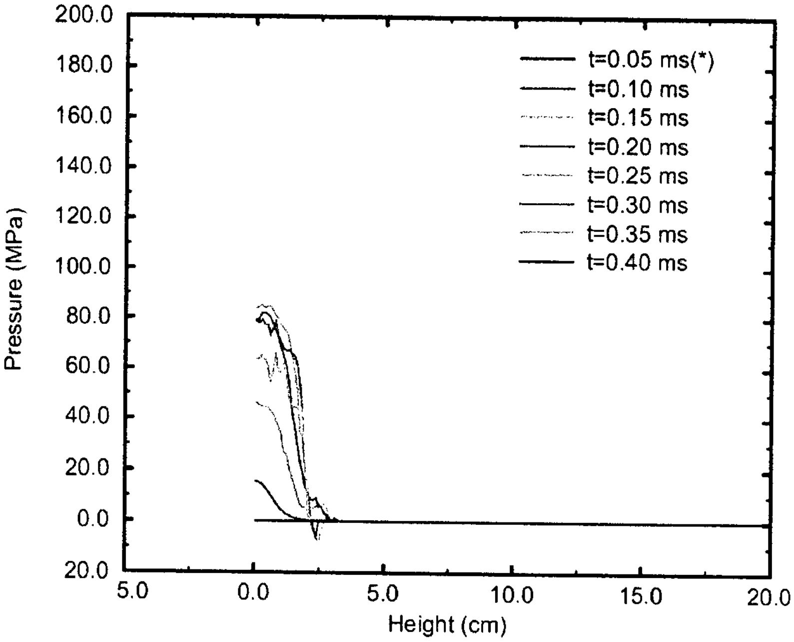

Figure 40. Y-Direction Spatial Cuts of Hydrostatic Pressure at X = 11.06 cm in the Explosive Fill of the M2A3 Munition in Computation DM2-24.

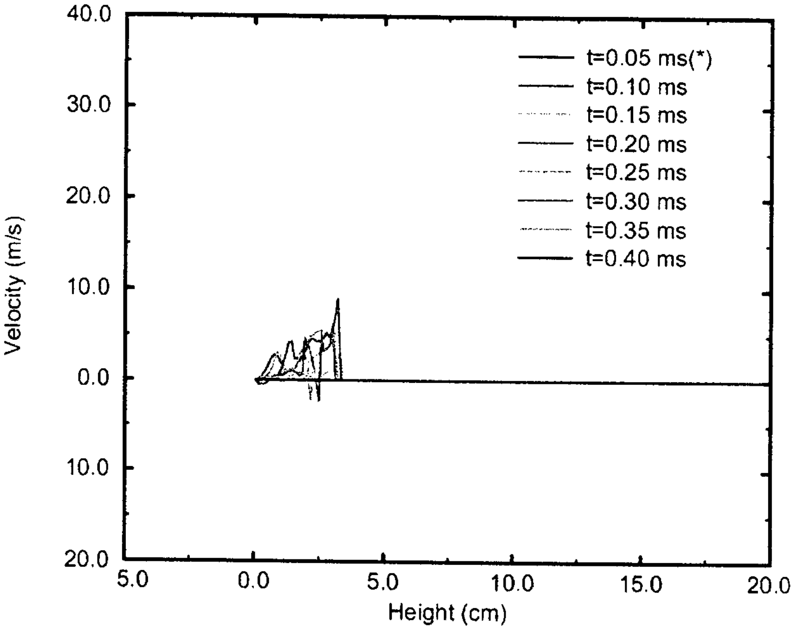

Figure 41. Y-Direction Spatial Cuts of Y-Direction Velocity at X = 11.06 cm in the Explosive Fill of the M2A3 Munition in Computation DM2-24.

4.3 Results of the M483 Double-Impact Computations

4.3.1 Analysis of the Flow Fields for the M483 Double-Impact Computations

Computation DM4-33 simulates a flyer plate traveling at 33.0 m/s and striking an M483 munition in a double-impact event. As noted earlier, the modeling of the M483 in DM4-33 and all other computations for the M483 has been greatly simplified as an outer steel casing with a continuous, complete fill of Comp-B. There was no attempt to model the actual individually cased submunitions whose normal explosive fill is A5. Thus, it is not a good representation of an actual M483 and should be considered as being more representative of a generic, HE-filled round. The corresponding experiment [9] used an actual M483 round and did not experience an exothermic reaction. The flow field at time t = 0.00 for computation DM4-33 is shown in Figure 42. The flyer plate is traveling from left to right in this figure at 33.0 m/s. The flow field is shown at the instant of impact on the left-most outer surface of the steel casing of the M483 munition, shown in green. The column of asterisks at the X = 35.0-cm location also delineates the reflective right boundary representing the steel backing plate. The simplified explosive fill is shown in red. Figure 43 shows the computational flow field at 2.00 ms after impact. The left side of the M483 is showing some distortion as a result of the impact. There is a noticeable development of a void between the casing and the explosive fill at the top of the M483 at this time. Figure 44 shows that additional distortion has occurred at the left side of the munition and that the void near the top has been at least temporarily reduced in size by 3.00 ms. The right-most side of the M483 has not yet arrived at the steel backing plate. Figure 45 shows the flow field at 4.00 ms, just before the impact of the right-most outer surface of the casing with the steel backing plate. The distortion at the left interface has increased from that at 3.00 ms, and the void at the top is somewhat larger than it was at 3.00 ms. Figure 46 shows the flow field at 6.00 ms, the ending time of computation DM4-33. The impact of the munition on the backing plate has caused compressive distortion on the side of the M483. There are only minimal traces of voids between the explosive and the casing at the top of the M483 at this time.

The flow field at time t = 0.00 for computation DM4-49 is not shown because it is the same as that in Figure 42 except for the impact velocity of 49.0 m/s of the flyer plate. There was an explosion in the experiment [9] that this computation simulates. Figure 47 shows the flow field at 2.00 ms after the impact of the flyer plate. As might be expected, there is more distortion at the left of the M483 for this interaction than in the impact of the 33.0-m/s flyer plate for DM4-33 shown in Figure 43 at this same time. There is a similar void between the explosive and the casing at the top of the munition. By 3.00 ms, the void has been partially closed, as may be seen in Figure 48. Figure 49 shows the flow field at 4.00 ms. By this time, the M483 has deformed in a nearly symmetric manner in the X direction as a result of its impact against the steel backing plate. The void at the top has closed. Figure 50 shows the flow field at 5.00 ms after the initial impact. This is the ending time of the computation. There is significant, nearly symmetric distortion in the X direction on both sides of the munition, with small voids between the explosive fill and the casing on both sides.

Computations DM4-45 and DM4-100 were run to simulate the impact of a flyer plate traveling at 45.0 m/s and 100.0 m/s, respectively, and striking the M483 in the same experimental configuration. There were no corresponding experiments. In the interest of brevity, flow-field plots for these computations are not shown. Computation DM4-45 simulated 6.00 ms. DM4-100 simulated 5.00 ms and showed a complete rupture of the casing starting just before 1.5 ms.

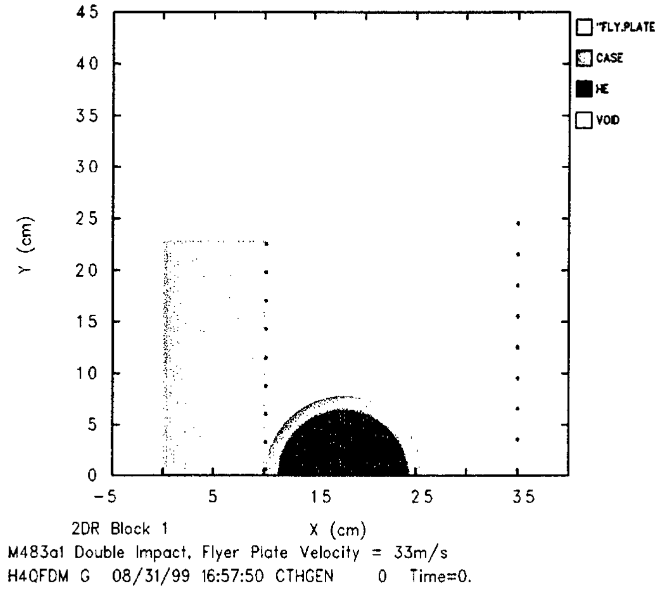

Figure 42. Flow Field at Time = 0.00 for Computation DM4-33, Double Impact of a Flyer Plate at 33.0 m/s With an M483 Munition.

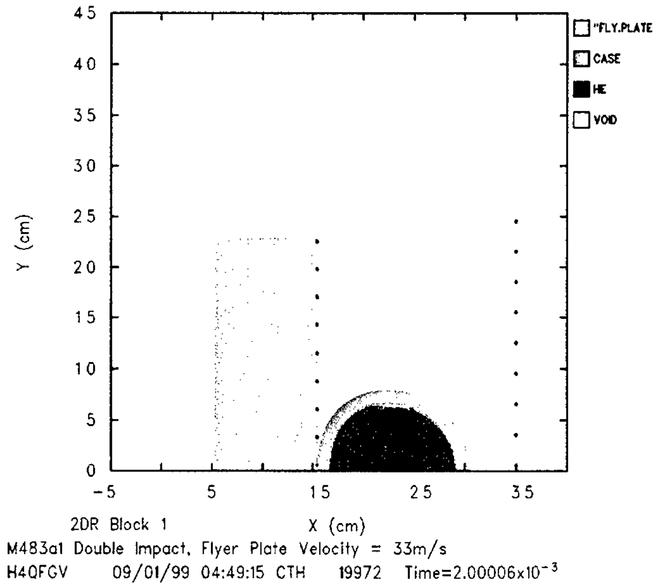

Figure 43. Flow Field at Time = 2.00 ms for Computation DM4-33, Double Impact of a Flyer Plate at 33.0 m/s With an M483 Munition.

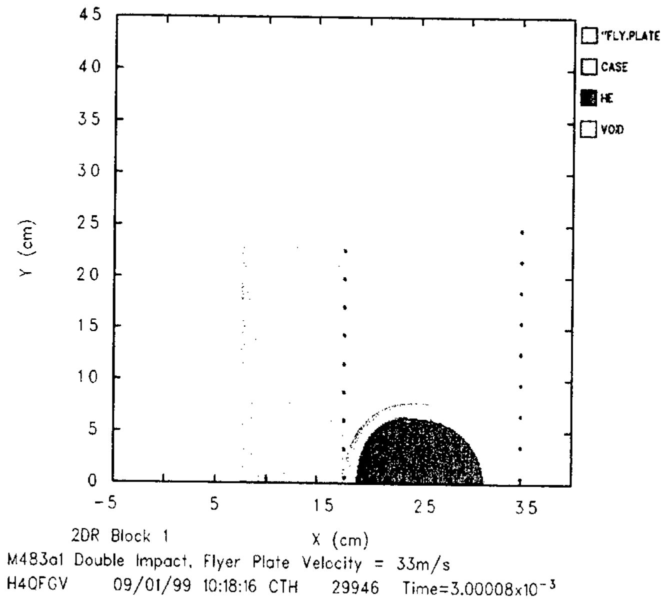

Figure 44. Flow Field at Time = 3.00 ms for Computation DM4-33, Double Impact of a Flyer Plate at 33.0 m/s With an M483 Munition.

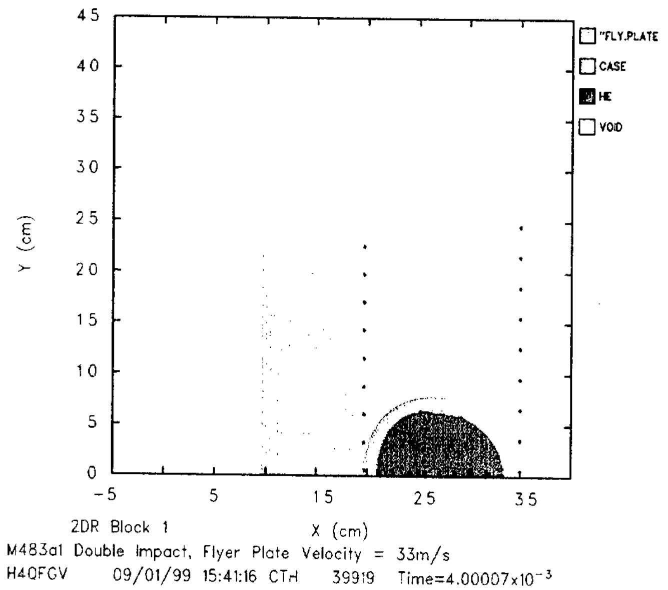

Figure 45. Flow Field at Time = 4.00 ms for Computation DM4-33, Double Impact of a Flyer Plate at 33.0 m/s With an M483 Munition.

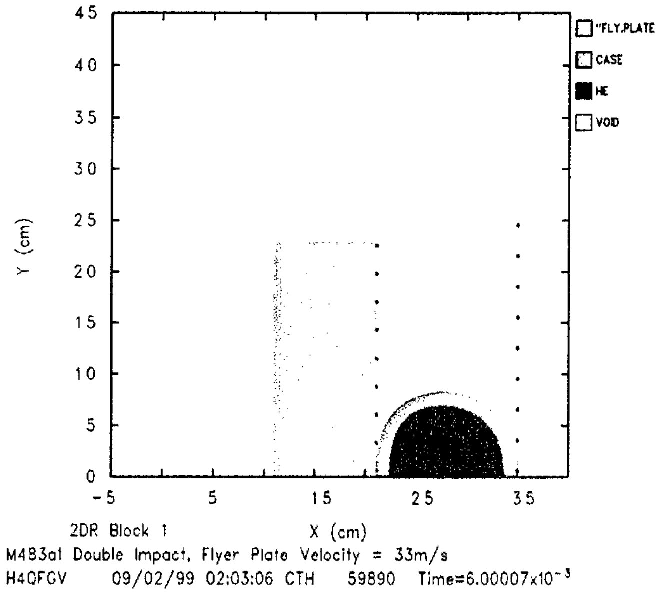

Figure 46. Flow Field at Time = 6.00 ms for Computation DM4-33, Double Impact of a Flyer Plate at 33.0 m/s With an M483 Munition.

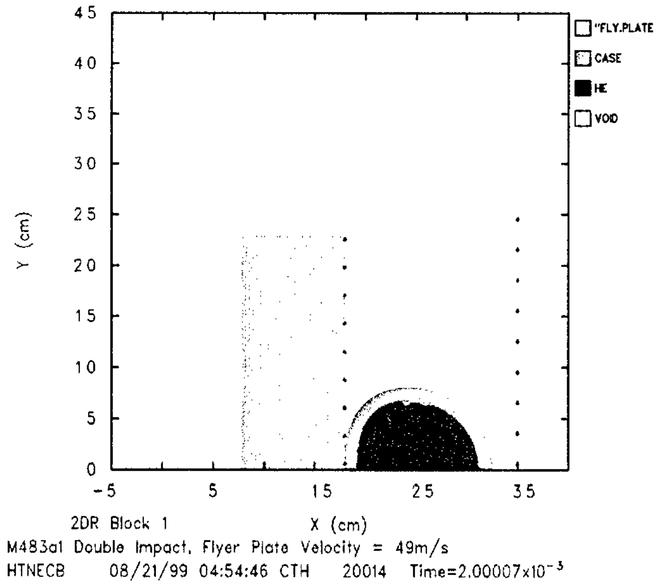

Figure 47. Flow Field at Time = 2.00 ms for Computation DM4-49, Double Impact of a Flyer Plate at 49.0 m/s With an M483 Munition.

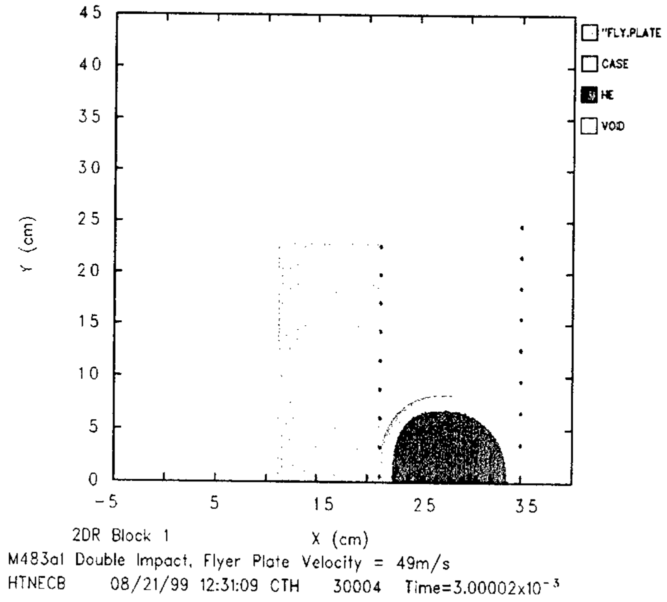

Figure 48. Flow Field at Time = 3.00 ms for Computation DM4-49, Double Impact of a Flyer Plate at 49.0 m/s With an M483 Munition.

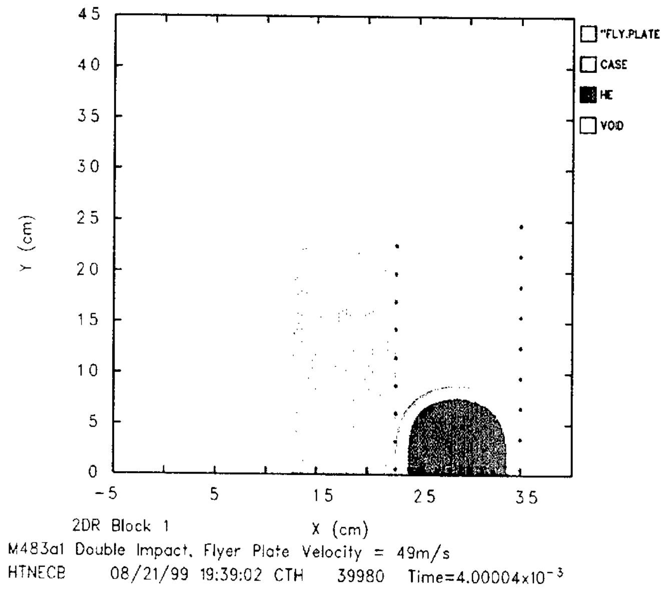

Figure 49. Flow Field at Time = 4.00 ms for Computation DM4-49, Double Impact of a Flyer Plate at 49.0 m/s With an M483 Munition.

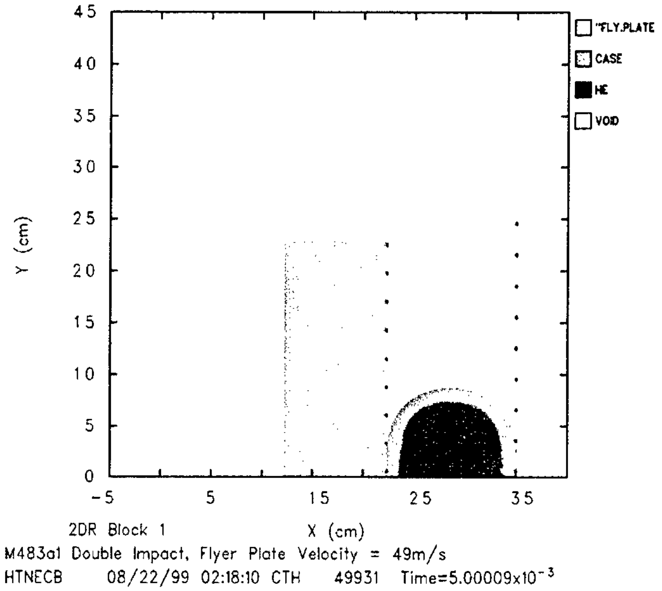

Figure 50. Flow Field at Time = 5.00 ms for Computation DM4-49, Double Impact of a Flyer Plate at 49.0 m/s With an M483 Munition.

4.3.2 Analysis of the Pressure in the Explosive Fills for the M483 Double-Impact Computations

Figure 51 shows the unsmoothed pressure at each of three locations within the explosive fill of the M483 munition for computation DM4-33. The point locations in the explosive fill of the M483 and choices of line color are the same as described earlier for the plots of pressure for the M2A3 in Figure 9 and will be the same throughout this section. As noted previously, Comp-B was simulated as a mechanical surrogate for the A5 actually used as the explosive fill for the submunitions in a real M483. There is considerably more high-frequency oscillation of the pressure than is shown in any of the previously discussed plots of pressure for the double-impact computations for the M2A3. This is caused by the initial steel-on-steel impact of the flyer plate on the M483 casing and the subsequent repeated reflections of shock, compression, and rarefaction waves at the high impedance mismatch interface between the steel casing and the explosive fill. In Figure 52, the pressures have been smoothed with the parameter $\tau = 8.0x10^{-6}$. This clearly shows that the peak pressure at the right interface is the highest, reaching a value of 4.0 kbar at 4.5 ms in the unsmoothed data. It is noteworthy that the explosive fill is, on average, in compression for these points for all of the simulated time, although all three points show numerous excursions into tension. The strongest tensile wave for these three points occurs at the right interface and has a minimum value of -1.0 kbar in the unsmoothed data.

Figure 53 shows the unsmoothed pressure at each of the same three locations within the explosive fill of the M483 munition for computation DM4-49. In Figure 54, the pressures have been smoothed with the parameter $\tau = 8.0x10^{-6}$. The range of pressures for these points shows a strong contrast to that for those same points for computation DM4-33. Computation DM4-49 shows nearly equal maxima of about 2.5 kbar at both the left and right interface and a minimum value of -0.8 kbar at the right interface. The late-time general compression of the explosive between 2.5 ms and 4.5 ms is much longer in duration than the 0.6-ms-wide compression with the greater maximum of 4.0 kbar (unsmoothed) at the right interface in DM4-33. Computation DM4-33, with the greater maximum pressure of 4.0 kbar, was a "No Go," while DM4-49 showed lower maxima of 2.5 kbar and experienced an explosion. This may add support to the argument for the existence of an initiating mechanism other than that from direct shock pressure, but these pressures are not known with complete assurance to be definitively the highest in those computations.

Figure 55 shows the unsmoothed pressure in the explosive fill for computation DM4-45. Figure 56 shows the same pressures as are shown in Figure 55, except that they have been smoothed with the parameter $\tau = 8.0x10^{-6}$. Given that there is only a 4.0-m/s difference in the impact velocities of the flyer plate, the smoothed pressure plots in Figure 56 for DM4-45 and Figure 54 for DM4-49 have some remarkably different features. Most notable are the differences in the plots between 3.0 and 5.0 ms. Figure 54 has a clear shock-like increase at the right interface of the explosive at 3.33 ms and the greatest smoothed peaks at the left interface at 3.85 ms and just before. Conversely, Figure 56 does not show a shock-like feature near 3.3 ms for any of the three points but does show the greatest smoothed peaks near 4.0 ms occurring at the right interface. Figure 57 shows the unsmoothed pressure in the explosive fill for computation DM4-100. Figure 58 shows the same pressures as are shown in Figure 57, except that they have been smoothed with the parameter $\tau = 8.0x10^{-6}$. As might be expected, Figures 57 and 58 show very different pressure curves from the lower velocity impacts at all three locations in the explosive fill because of the much higher 100.0-m/s impact velocity. The sharp drop in pressure after about 1.5 ms appears to correspond with the rupture of the casing, which began shortly before that time.

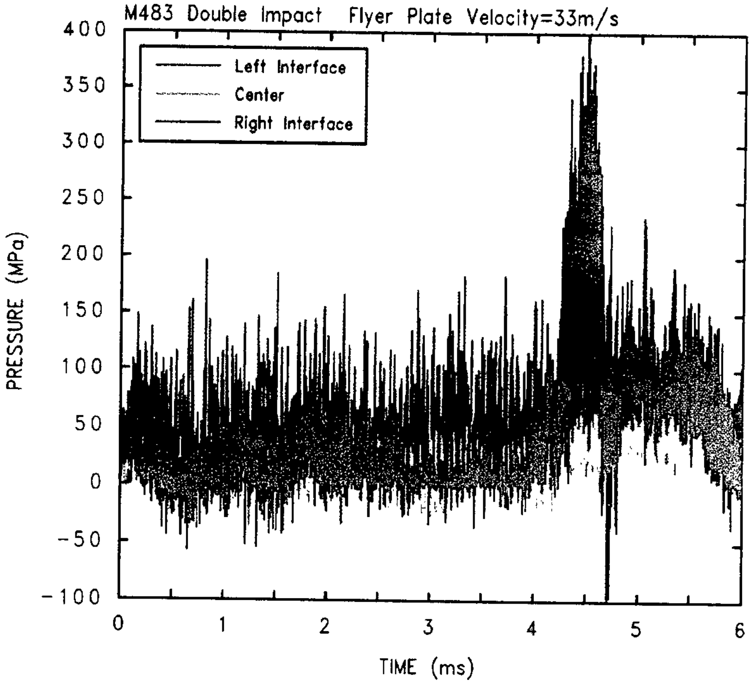

Figure 51. Pressure in the Unreacted Explosive Fill of the M483 Munition in Computation DM4-33 (unsmoothed).

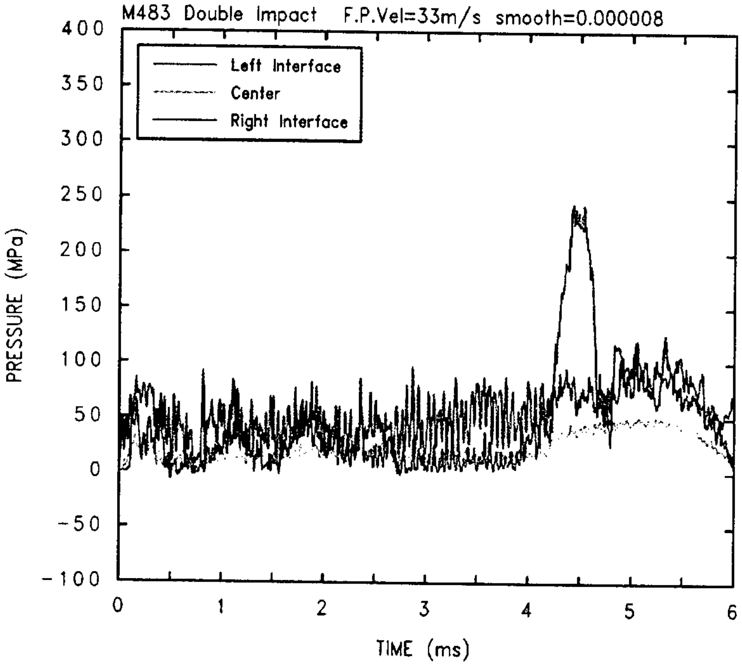

Figure 52. Pressure in the Unreacted Explosive Fill of the M483 Munition in Computation DM4-33 (smoothed).

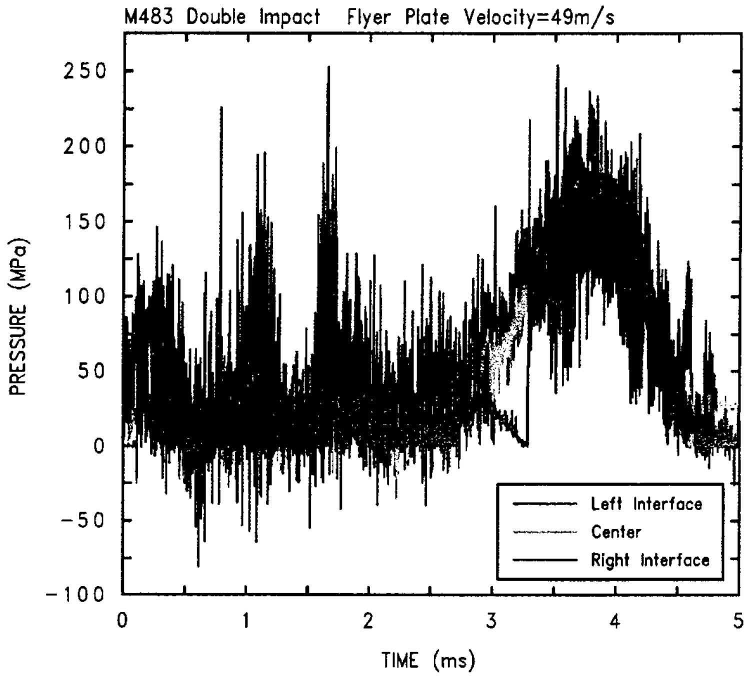

Figure 53. Pressure in the Unreacted Explosive Fill of the M483 Munition in Computation DM4-49 (unsmoothed).

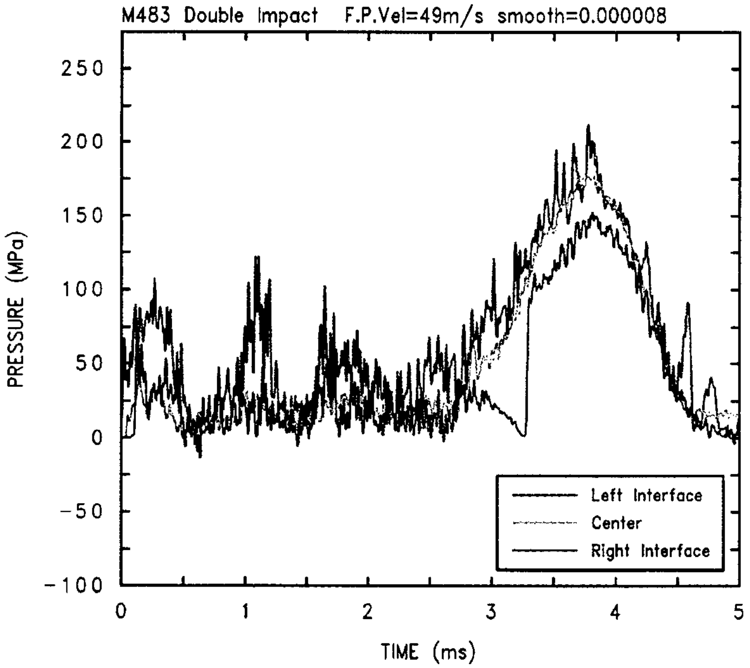

Figure 54. Pressure in the Unreacted Explosive Fill of the M483 Munition in Computation DM4-49 (smoothed).

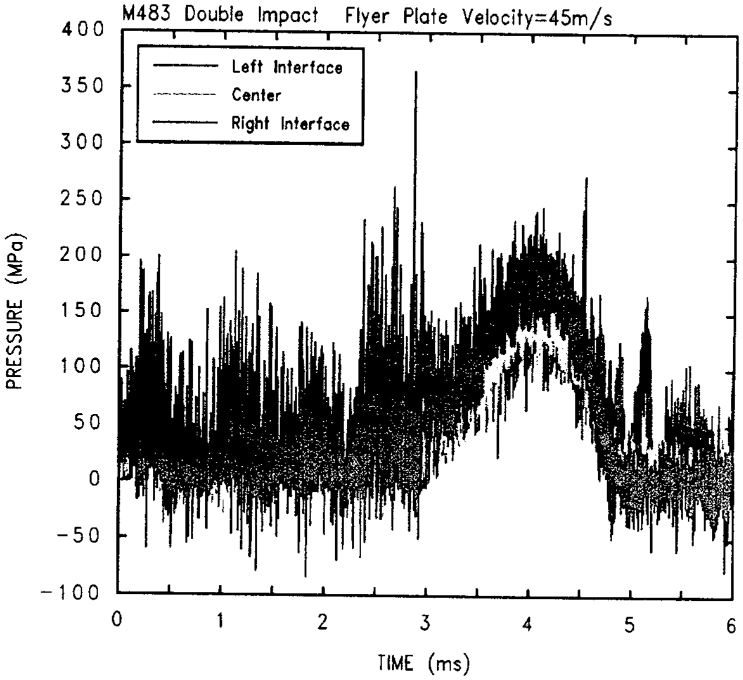

Figure 55. Pressure in the Unreacted Explosive Fill of the M483 Munition in Computation DM4-45 (unsmoothed).

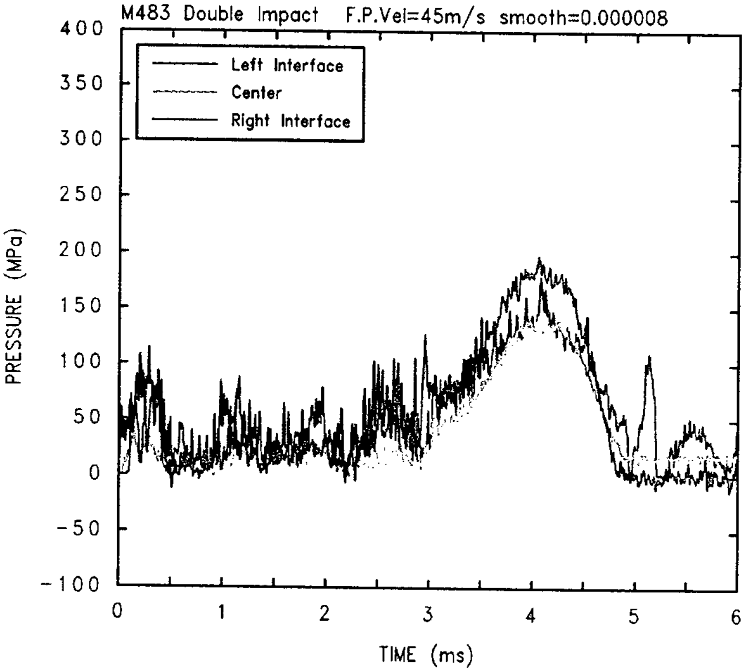

Figure 56. Pressure in the Unreacted Explosive Fill of the M483 Munition in Computation DM4-45 (smoothed).

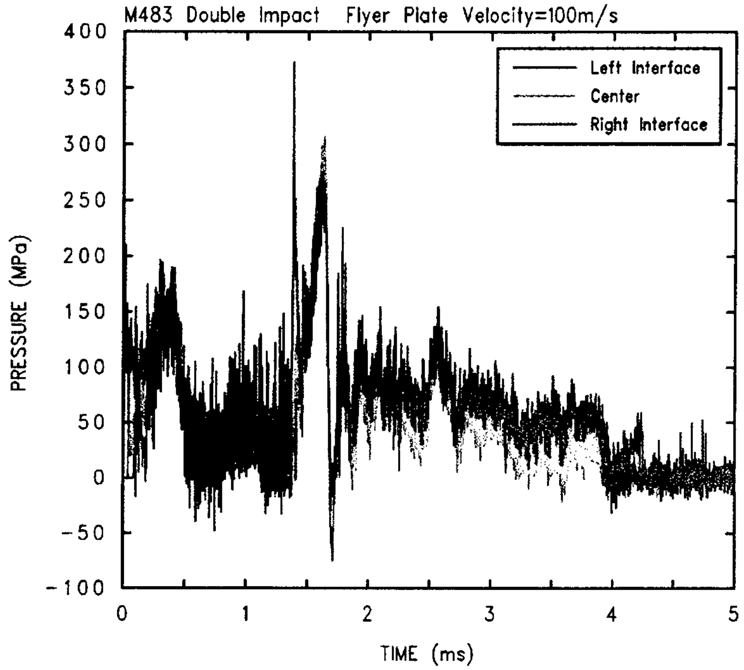

Figure 57. Pressure in the Unreacted Explosive Fill of the M483 Munition in Computation DM4-100 (unsmoothed).

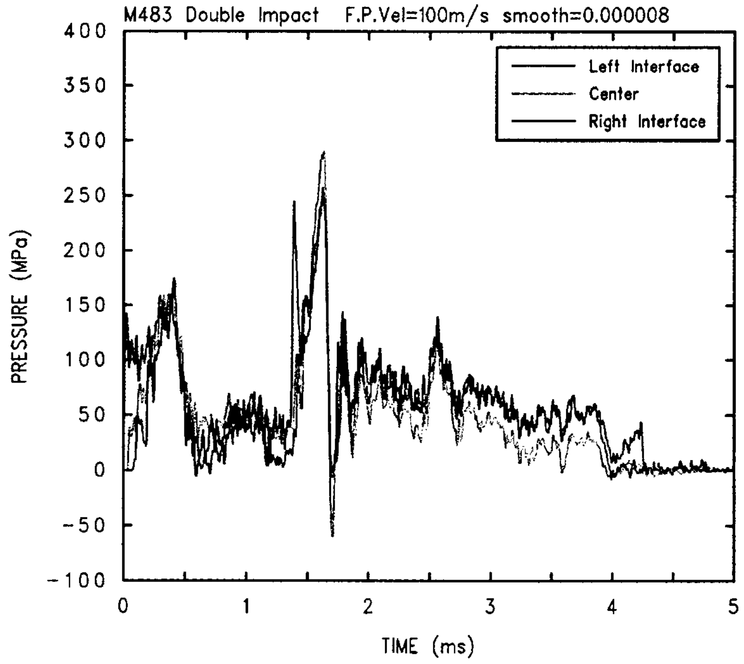

Figure 58. Pressure in the Unreacted Explosive Fill of the M483 Munition in Computation DM4-100 (smoothed).

4.3.3 Analysis of the Bulk Motion of the Explosive Fills for the M483 Double-Impact Computations

Figure 59 shows the X-direction momentum of the flyer plate and the X- and Y-direction momenta of the explosive fill of the M483 munition versus time in computation DM4-33. The values of momentum at 6.0 ms clearly show that the impact sequence has ended by this time, with the flyer plate in a rebound phase. Figure 60 shows the X-direction velocity of the flyer plate and the X- and Y-direction velocities of the explosive fill of the M483 munition. These velocities were computed as before from the respective momenta of the desired material. Figure 61 shows the X-direction acceleration of the flyer plate and the X- and Y-direction accelerations of the explosive fill of the M483 munition. It is interesting to note that after about 0.25 ms, the Y-direction accelerations of the explosive fill have a similar range to, and sometimes a larger range than, the X-direction accelerations of the fill.

Figure 62 shows the X-direction momentum of the flyer plate and the X- and Y-direction momenta of the explosive fill of the M483 munition versus time in computation DM4-49. Figure 63 shows the X-direction velocity of the flyer plate and the X- and Y-direction velocities of the explosive fill of the M483 munition. These velocities were computed from the respective momenta of the desired material as before. Figure 64 shows the X-direction acceleration of the flyer plate and the X- and Y-direction accelerations of the explosive fill of the M483 munition. The accelerations of the explosive in both the positive and negative X and Y directions are greater in magnitude than the corresponding ones for DM4-33. As was the case for DM4-33, the accelerations of the explosive in both directions are also comparable to one another in both range and magnitude in this computation.

Figure 65 shows a collected set of plots of flyer-plate velocity for each of the double-impact computations for the M483. Figure 66 shows the plots of the X-direction velocity of the explosive fill and Figure 67 shows the plots of the Y-direction velocity of the explosive fill. The plot for the Y-direction velocity of the explosive fill in DM4-100 in Figure 67 shows a sharp increase just before 1.5 ms, indicating the response of the explosive fill to the rupture of the casing that was noted earlier. Just as was the case for the M2A3 double-impact computations, basically a two-stage transformation of the X-direction momentum of the flyer plate to the various manifestations of shear, internal energy, and pressure in the explosive fill can be seen in these figures.

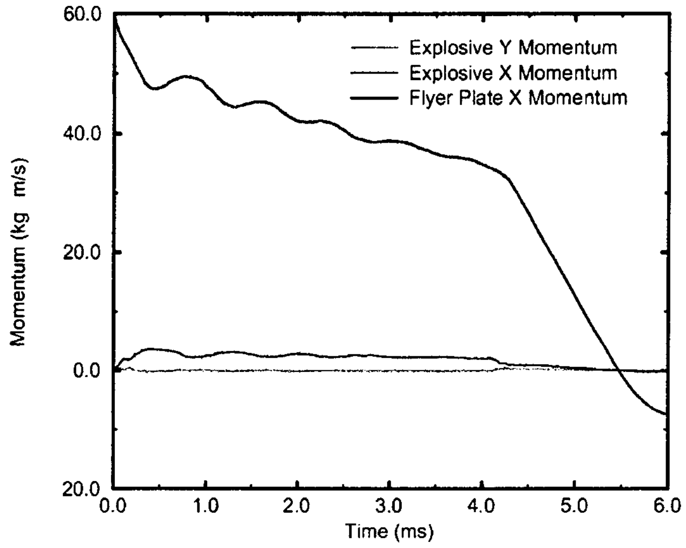

Figure 59. Momenta of the Flyer Plate and the Unreacted Explosive Fill of the M483 Munition in Computation DM4-33.

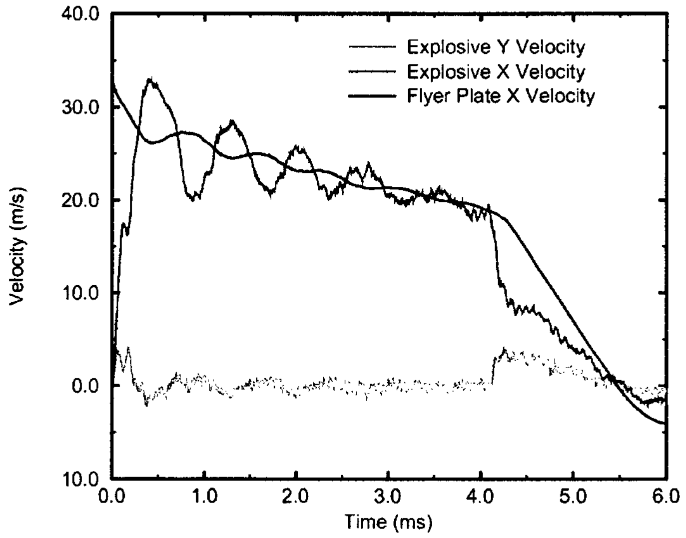

Figure 60. Velocities of the Flyer Plate and the Unreacted Explosive Fill of the M483 Munition in Computation DM4-33.

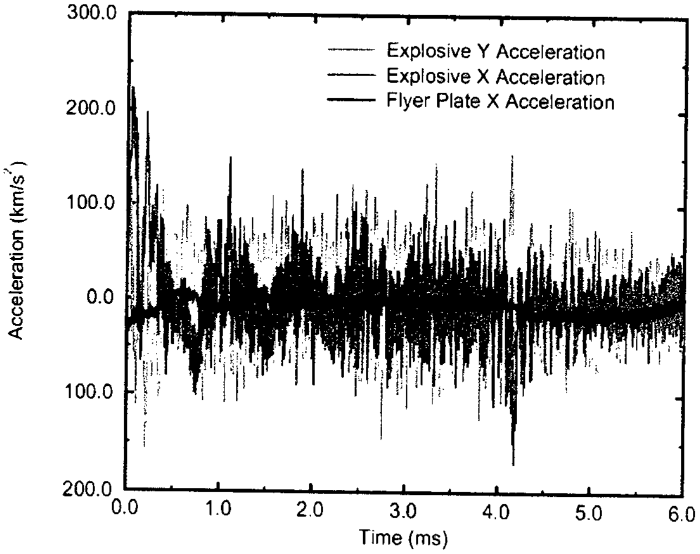

Figure 61. Accelerations of the Flyer Plate and the Unreacted Explosive Fill of the M483 Munition in Computation DM4-33.

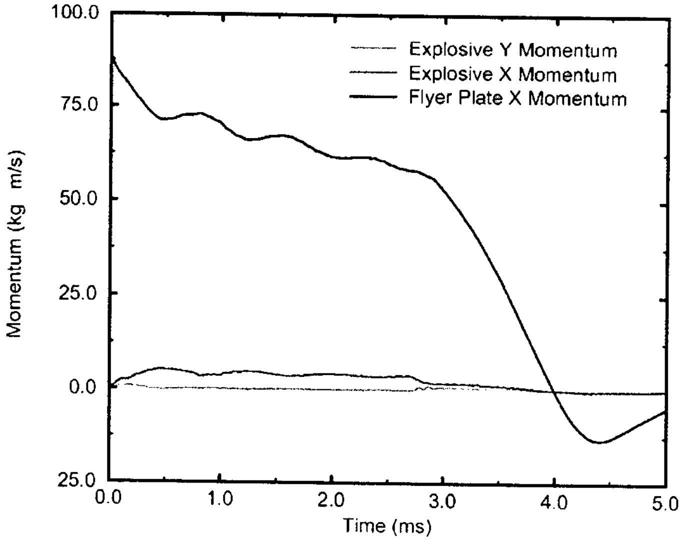

Figure 62. Momenta of the Flyer Plate and the Unreacted Explosive Fill of the M483 Munition in Computation DM4-49.

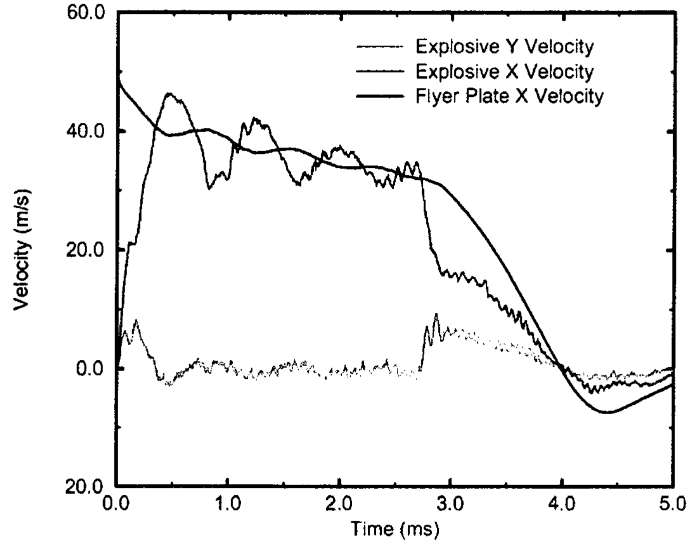

Figure 63. Velocities of the Flyer Plate and the Unreacted Explosive Fill of the M483 Munition in Computation DM4-49.

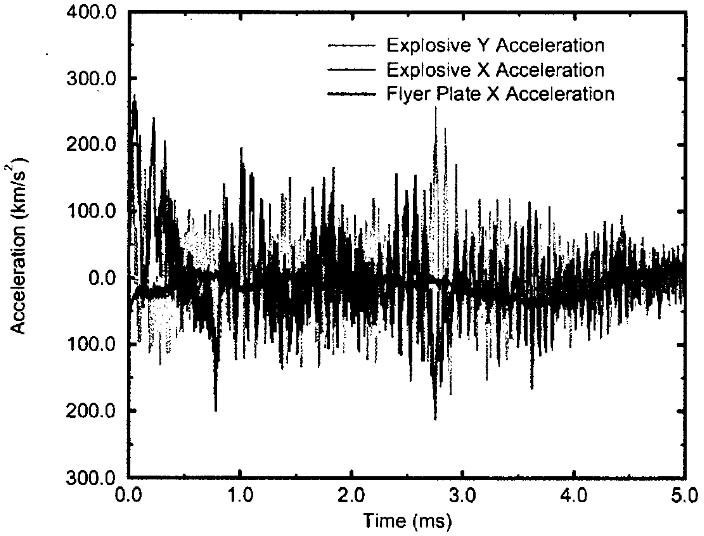

Figure 64. Accelerations of the Flyer Plate and the Unreacted Explosive Fill of the M483 Munition in Computation DM4-49.

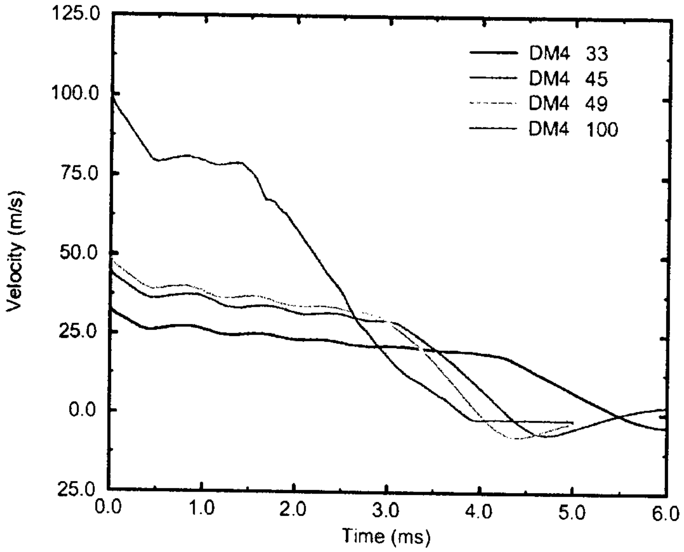

Figure 65. X-Direction Velocities of the Flyer Plate for Each of the Double-Impact Computations for the M483 Munition.

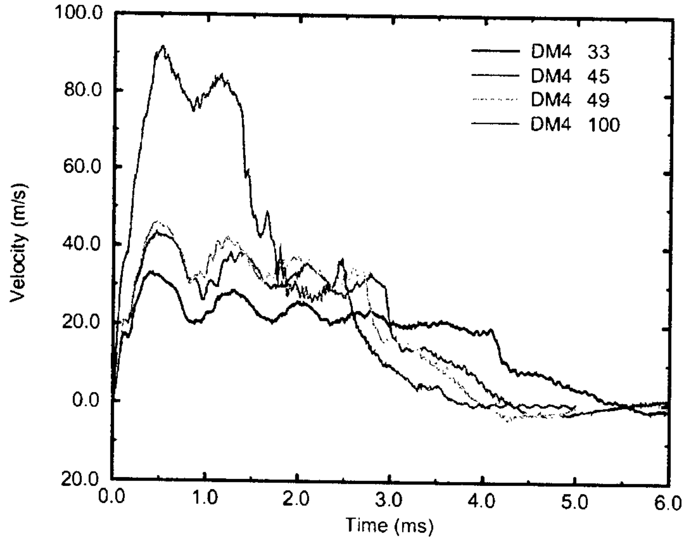

Figure 66. X-Direction Velocities of the Explosive Fill of the M483 Munition for Each of the Double-Impact Computations.

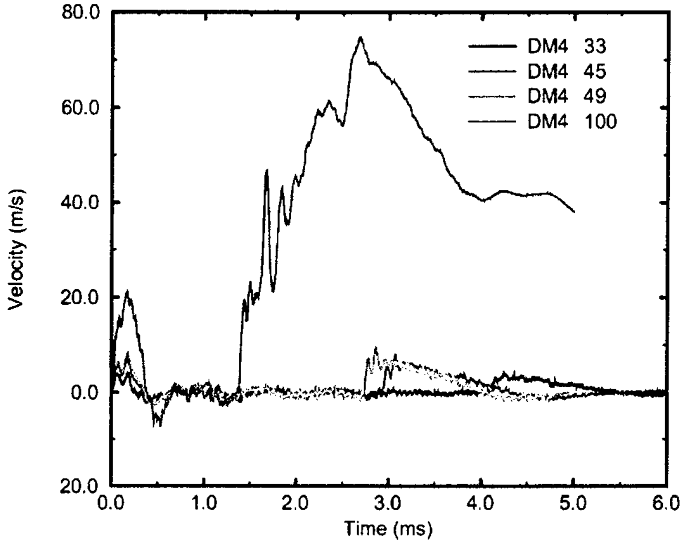

Figure 67. Y-Direction Velocities of the Explosive Fill of the M483 Munition for Each of the Double-Impact Computations.

5. A Comparison of the Crushing-Impact Computations and Experiments

5.1 The Computational Grid Geometry

The geometries of the computational flow fields used for all crushing-impact computations for the M2A3 and M483 munitions are described in Table 4. The left-to-right construction of the buffer pack as it was employed in the experiments is one of the pieces of information shown in the first column of Table 4, except that Lucite is simulated in place of the actual polyethylene used in the experiments. The computational buffer pack was made of eight alternating layers, starting with a Lucite layer, then steel, Lucite, and so on, ending with a steel layer, with each layer having a thickness of 2.54 cm (1.0 in.). The reverse-ordered buffer packs simulated in the computations with the trailing "R" identifier in the computation number started with a steel layer on the flyer-plate side and ended with a Lucite layer on the munition side. No reverse-ordered buffer packs were used in the experiments.

Table 4. Main Features of Flow-Field Geometry for the Crushing-Impact Computations

Left to Right in X-Direction Geometry	X Direction (cm)	Y Direction (cm)	Shell Thickness (cm)
Reflective Left Boundary	Yes	-	-
Reflective Left Boundary to Flyer Plate Simulated as a Void	(Open Span) M2A3 - 3.18 M483 – 2.75	-	-
Steel Flyer Plate	(Thickness) Both - 10.16	(1/2 Height) Both - 22.816	-
Eight-Layer Buffer Pack Lucite/Steel/etc. L/S/L/S/L/S/L/S	(Thickness) Both – 20.32	(1/2 Height) Both – 17.145	-
Phenolic Shell, No Shell or Void Simulated	-	-	M2A3 - 0.0
Steel Shell	-	-	M483 - 1.33985
Unreacted Composition B	(Diameter) M2A3 - 17.145 M483 - 12.8143	(Radius) M2A3 - 8.5725 M483 - 6.4072	-
Phenolic Shell, No Shell or Void Simulated	-	-	M2A3 - 0.0
Steel Shell	-	-	M483 - 1.33985
Reflective Right Boundary Simulating Backing Plate	Yes	-	-
Reflective Bottom Boundary to Transmissive Top Boundary	-	M2A3 – 70.00 M2A3 (reversed) - 50.00 M483 (all) - 35.0	-

5.2 Results of the M2A3 Crushing-Impact Computations

5.2.1 Analysis of the Flow Fields for the M2A3 Crushing-Impact Computations

Computation CM2-45 simulated the crushing-impact experiment in which a flyer plate traveling at 45.0 m/s struck the eight-layer computational buffer pack (Lucite/steel/etc.) and subsequently crushed an M2A3 against the backing plate. This resulted in a "Burn" reaction in the experiment.[9] This was a less severe reaction than the detonation that was observed in the experiment for the double impact for this munition with the same flyer-plate velocity. Figure 68 shows the computational flow field at time t = 0.00 at the instant of impact of the flyer plate on the buffer pack. All of the crushing-impact computations will have t = 0.00 defined at this instant. In this figure, the flyer plate is moving from left to right at 45.0 m/s, which is also the measure of positive X-direction velocity. Figure 69 shows the computational flow field at time t = 4.00 ms after impact. A comparison with Figure 7 for the double-impact interaction of a flyer plate traveling at the same impact velocity shows nearly the same resulting distortion of the M2A3 once the different spatial scales of the figures are accounted for. Figure 70 shows the computational flow field at time t = 5.00 ms, which is close to the ending time of 5.27 ms of the computation.

All of the experiments [9] used the eight-layer forward-ordered buffer pack, while the associated earlier computations [9] simulated a four-layer reverse-ordered buffer pack with two layers each of steel and Lucite. The reasons for simulating the buffer pack in that manner and the dimensions of the simulated layers were not stated in the report. The question arose during the execution of these current computations as to what would be the effects of reversing the order of the layers in the buffer pack. Computation CM2-45R simulated almost exactly the same configuration as in CM2-45, except that the order of the layers in the buffer pack is reversed. Figure 71 shows the flow field for this computation at time t = 0.00. In the interest of brevity, no other flow-field plots will be shown. This computation simulated 5.27 ms, just as CM2-45 did.

Computation CM2-100 simulated the same geometric and material configuration (forward-ordered buffer pack) as shown in Figure 68, except that the impact velocity of the flyer plate is 100.0 m/s. No flow-field plots will be shown for this computation, which simulated 5.25 ms. Computation CM2-100R simulated the same initial configuration with the reverse-ordered buffer pack as shown in Figure 71 but with a 100.0-m/s impact velocity for the flyer plate and a simulated time of 4.75 ms. Finally, computation CM2-300 simulated a flyer plate impacting at 300.0 m/s, with an initial flow field and forward-ordered buffer pack the same as in Figure 68 except for the velocity of the flyer plate. CM2-300 simulated a total time of 3.36 ms. No flow-field plots for these computations will be shown.

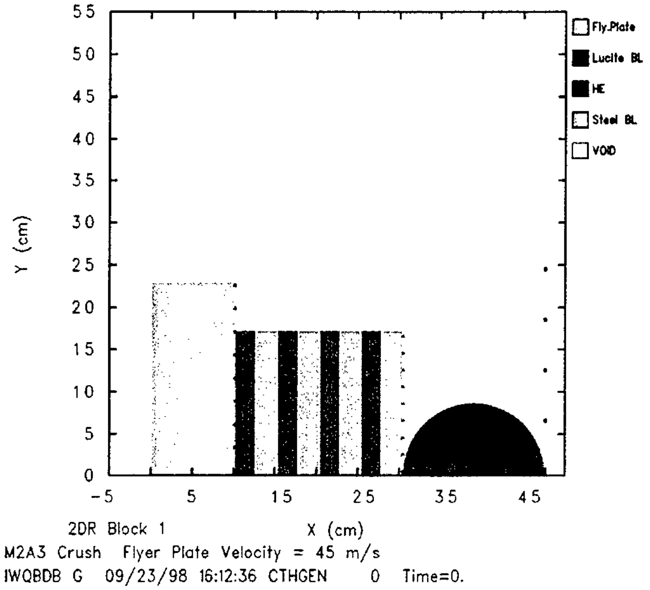

Figure 68. Flow Field at Time = 0.00 for Computation CM2-45, Crushing Impact of a Flyer Plate at 45.0 m/s on a Combination of a Forward-Ordered Buffer Pack and an M2A3 Munition.

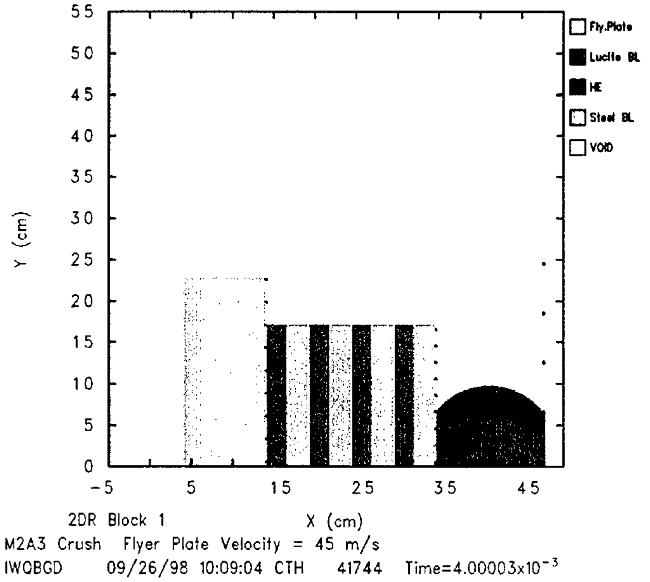

Figure 69. Flow Field at Time = 4.00 ms for Computation CM2-45, Crushing Impact of a Flyer Plate at 45.0 m/s on a Combination of a Forward-Ordered Buffer Pack and an M2A3 Munition.

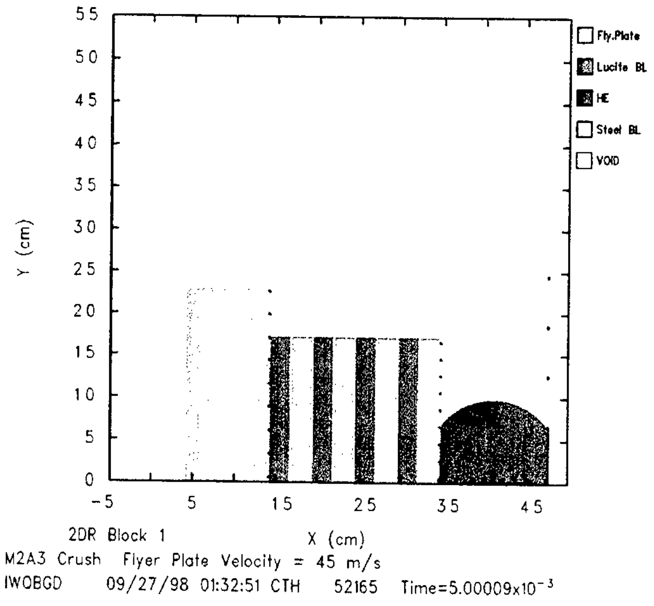

Figure 70. Flow Field at Time = 5.00 ms for Computation CM2-45, Crushing Impact of a Flyer Plate at 45.0 m/s on a Combination of a Forward-Ordered Buffer Pack and an M2A3 Munition.

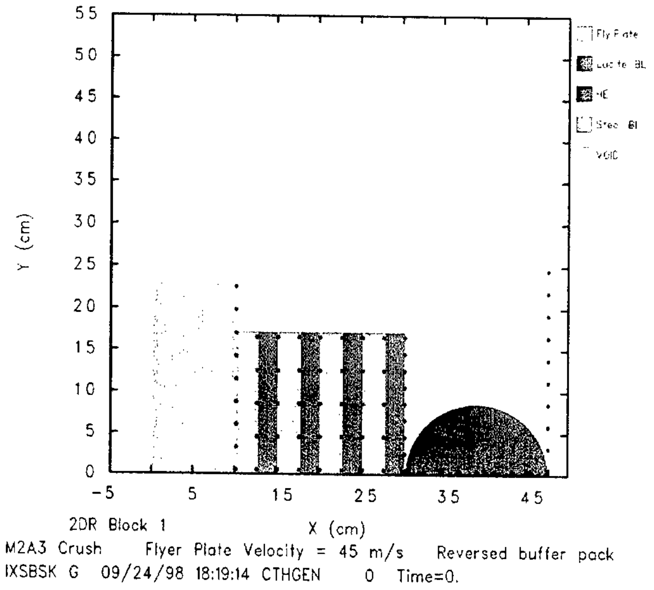

Figure 71. Flow Field at Time = 0.00 for Computation CM2-45R, Crushing Impact of a Flyer Plate at 45.0 m/s on a Combination of a Reverse-Ordered Buffer Pack and an M2A3 Munition.

5.2.2 Analysis of the Pressure in the Explosive Fills for the M2A3 Crushing-Impact Computations

Figure 72 shows the pressure at three locations within the Comp-B explosive fill of the M2A3 munition for computation CM2-45 (forward-ordered buffer pack). The locations of the points within the fill and the choices of line color are the same as those for the double-impact computations and will remain the same throughout this section. Figure 73 shows the same pressure data as in Figure 72 after smoothing with the standard HISPLT [27] data-smoothing option, with the smoothing parameter $\tau = 4.0x10^{-6}$. This makes it easier to see the trends in the data with only some minor loss in the local extrema in the curves. As stated previously, this and all other crushing-impact computations were run with a value for Poisson's ratio, ν, of 0.35, whereas the double-impact computations were run with a value of 0.45, which is now realized to be too great a value. Computation CM2-45pr was run with all parameters kept the same as for CM2-45 except for setting $\nu = 0.45$ to provide an indication of the effect of this change on the computational results. While several parameters within the range of elastic responses of the undetonated explosive can be affected, only the effect on the pressure in the same three locations as shown in Figures 72 and 73 is discussed here. Figure 74 shows the unsmoothed pressures in those same three locations in CM2-45pr, and Figure 75 shows the pressures smoothed with the same value of the smoothing parameter $\tau = 4.0x10^{-6}$. The early peaks in the pressures, both unsmoothed and smoothed, are essentially the same for the two computations. There are some notable differences in the structure of the lesser extrema at later time but not so much that would warrant rerunning the full computational set or call into question the analysis of the general trends and the conclusions drawn from the analysis. Virtually all of the responses of the undetonated explosive fill in these computations are in catastrophic yielding with large deformations well beyond the elastic range. Poisson's ratio is an elastic-deformation parameter, and so an inaccurate value would be expected to have only a minor influence on peak values of pressure in high-deformation interactions such as the ones of interest here. Nonetheless, a more accurate value of ν should have been determined and used.

For future reference, a brief analysis and computation of a more accurate value of ν for undetonated Comp-B are presented here. Discussions were held with Dandekar [29] as to the best way to determine values for ν from available data. At present, a draft technical report is being prepared by Spletzer and Dandekar [30] that includes a discussion of this topic, along with a set of equations from Schreiber et al. [31], which can be used to compute the elastic constants of a material. These equations are reproduced here with permission from Dr. Dandekar.[29]

$$L = \rho U_l^2 \tag{1}$$

$$G = \rho U_s^2 \tag{2}$$

$$K = \rho \left[U_l^2 - \frac{4U_s^2}{3} \right] \tag{3}$$

$$E = \rho \frac{[3U_l^2 U_s^2 - 4U_s^4]}{(U_l^2 - U_s^2)} \tag{4}$$

$$\lambda = \rho \left(U_l^2 - 2U_s^2 \right) \tag{5}$$

$$\nu = \frac{[U_l^2 - 2U_s^2]}{[2\,(U_l^2 - U_s^2)]} \tag{6}$$

Additional useful relations for an isotropic, elastic medium are **[28]**

$$G = \mu = \frac{E}{[2\,(1+\nu)]} \tag{7}$$

$$K = \frac{E}{[3\,(1-2\nu)]} \tag{8}$$

$$\lambda = \frac{\nu E}{[(1+\nu)\,(1-2\nu)]} \tag{9}$$

$$K = \lambda + \frac{2G}{3} \tag{10}$$

The various parameters are ρ = density, U_l = longitudinal wave speed, U_s = shear wave speed, L = longitudinal modulus, G = shear modulus, K = bulk modulus, E = Young's modulus, λ and μ (the Lamé constants), and ν = Poisson's ratio.

Published **[32]** values for the longitudinal and shear wave speeds for Comp-B are 3.12 km/s and 1.71 km/s, respectively. Inserting these values in Equation 6, ν is estimated to be 0.285. In the absence of more accurate information, this value for ν is suggested as the one to use for elastic deformation in Comp-B. Similarly, a better value of ν = 0.321 to have used for Lucite can be estimated from the longitudinal and shear wave speeds (2.69 km/s and 1.38 km/s, respectively) published by Dandekar and Gaeta.**[33]** These relations for estimating elastic constants are suggested for use in the absence of directly measured values for the various elastic constants.

Figure 76 shows the pressure at the three locations within the Comp-B explosive fill of the M2A3 munition for computation CM2-45R (reverse-ordered buffer pack). Figure 77 shows the same pressure data as in Figure 76 after the smoothing parameter $\tau = 5.0x10^{-6}$ has been used. Both computations simulate the impact of a steel flyer plate traveling at an initial velocity of 45.0 m/s prior to striking a buffer pack protecting the M2A3 munition. An interesting difference in the pressures can be seen by comparing the plots of smoothed pressures in Figure 73 (CM2-45) with those in Figure 77 (CM2-45R). The pressures at the center of the explosive fill, shown by the green lines in the two figures, are roughly comparable to one another in their values versus time. This is also true of the pressures at the right interface of the explosive fill, shown by the blue lines in the two figures. There is no immediate, local difference in the two computations at the right interface of the explosive fill. Both computations started at t = 0.00 with the right-most edge of the explosive on the X axis (i.e., the height Y = 0.00) at the reflective right boundary.

The pressures at the left interface, shown by the red line in the two figures, are significantly different. The smoothed peaks in Figure 73 between 0.0 and 1.0 ms are approximately 3.0 kbar, while the peak in Figure 77 within the same time span is approximately 1.0 kbar. Similarly, Figure 73 shows a peak of approximately 1.0 kbar near 3.0 ms, while Figure 77 shows a peak of approximately 0.25 kbar at that same time. There is a significant physical difference in the two computations at the left interface of the explosive fill because of the structure of the buffer pack. In computation CM2-45 (see Figure 73), the flyer plate struck a leading Lucite layer in the forward-ordered buffer pack, which then struck the explosive fill with a trailing steel layer. This combination may have allowed a greater transmission of energy from the steel flyer plate into the leading Lucite layer (and therefore into the buffer pack as a whole), and then a greater transmission of energy from the trailing steel layer of the buffer pack into the explosive fill. Conversely, in computation CM2-45R (see Figure 77), the mechanics are reversed by the reverse-ordered buffer pack. Here, the flyer plate has a steel-on-steel impact with the leading layer of the buffer pack. The energy transfer from the buffer pack to the explosive fill is through the trailing Lucite layer of the buffer pack. The net effect is to have a less severe energy transfer to the explosive fill for this configuration.

These results for the crushing-impact computations CM2-45 (see Figures 72 and 73) and CM2-45R (see Figures 76 and 77) also offer an opportunity for an informative comparison with the results from the double-impact computation, DM2-45, for the M2A3. The smoothed peak pressures at the right interface of the explosive fill in DM2-45 (see Figure 14) are comparable at 1.0 kbar to those in CM2-45R (reverse-ordered buffer pack) at 1.20 kbar but occur at different times, with the over-all pressure histories having completely different structures. The peak pressures at the left interface of the explosive for computations CM2-45R and DM2-45 are also quite different but at a lower level. The smoothed peak for DM2-45 is approximately 0.6 kbar, while the smoothed peak for CM2-45R is 67 percent greater at 1.0 kbar. Thus, the pressures computed along the horizontal mid-plane of the explosive fill are roughly comparable for the double-impact computation, DM2-45, and the reverse-ordered buffer pack computation, CM2-45R, and are well below the established minimum levels [1] of 3.0 to 4.0 kbar for the initiation of detonation by shock overpressure.

A comparison of pressures along that same horizontal mid-plane in the explosive fill between computations CM2-45 and DM2-45 is particularly interesting. There are two (smoothed) pressure peaks at the left interface prior to 1.0 ms in CM2-45 (forward-ordered buffer pack) that are approximately 3.0 kbar, about five times greater than the 0.6-kbar (smoothed) peak for that same point in DM2-45 (see Figure 14). The lower (smoothed) peak at the left interface at about 3.1 ms in CM2-45 may have been caused by temporarily separated plates in the buffer pack slapping back together. The (smoothed) 1.0-kbar pressure peak for DM2-45 at the right interface is also less than the 1.25-kbar (smoothed) pressure peak for CM2-45. Thus, the (smoothed) peak value of pressure in the explosive for CM2-45 is near the lower limit for shock initiation, and the values for DM2-45 (and also CM2-45R) are well below the lower limit. A reference to the summary of the computations reported here and the previously performed experiments [9] shows that for the M2A3 struck by a flyer plate at 45.0 m/s, the double-impact experiment resulted in a high-order detonation and the crushing-impact experiment (forward-ordered buffer pack) resulted in a "Burn" reaction. There were no experiments that involved a reverse-ordered buffer pack. Taken together, the results of the experiments and the computations imply, but do not confirm, the possibility that initiating mechanisms may be present other than a rapid rise in pressure (i.e., a simple manifestation of maximum principal stress) as would be caused by the passage of a shock. A further qualification that applies to this statement is that the M2A3 munitions in all of the experiments had only the normal thin phenolic casing and were modeled with no casing in any of the crushing-impact computations.

Figure 78 shows the pressure at the three locations within the Comp-B explosive fill of the M2A3 munition for computation CM2-100 (forward-ordered buffer pack). Figure 79 shows the same pressure data as in Figure 78 after the smoothing parameter $\tau = 5.0x10^{-6}$ was used. Figure 80 shows the pressure at the three locations within the Comp-B explosive fill of the M2A3 munition for computation CM2-100R (reverse-ordered buffer pack). Figure 81 shows the same pressure data as in Figure 80 after the smoothing parameter $\tau = 3.0x10^{-6}$ was used. Both computations simulate the impact of a steel flyer plate traveling at 100.0 m/s prior to striking a buffer pack protecting the M2A3. A comparison of the smoothed pressure plots in Figure 79 for CM2-100 with those in Figure 81 for CM2-100R shows behavior similar to that described in the comparison of the smoothed pressure plots for the 45.0-m/s impact. A comparison with the smoothed pressure plots in Figure 16 for computation DM2-100 also confirms the type of behavior in pressure peaks that was just discussed for the 45.0-m/s impact. The pressures at both the center of the explosive fill and at the right interface are comparable through 2.5 ms for CM2-100 and CM2-100R but with greater peak values for CM2-100R after that time. The pressure at the left interface of the explosive fill in CM2-100 (see Figure 79) shows three peaks above

3.0 kbar between 0.0 and 1.0 ms, while CM2-100R shows a single smoothed peak at 2.0 kbar in that same span of time. Thereafter, the pressure values for the left interface are roughly comparable to one another for the two computations. The peak values of pressure for DM2-100 are comparable to those for CM2-100R (reverse-ordered buffer pack) and well below those for CM2-100 (forward-ordered buffer pack). There were no comparable experiments for a flyer plate striking an M2A3 munition at 100.0 m/s.

Figure 82 shows the pressure at the three locations within the Comp-B explosive fill of the M2A3 munition for computation CM2-300 (forward-ordered buffer pack) for a flyer-plate impact at 300.0 m/s. Figure 83 shows the same pressure data as in Figure 82 after the smoothing parameter $\tau = 3.0x10^{-6}$ was used. No complementary computation with a reverse-ordered buffer pack was performed.

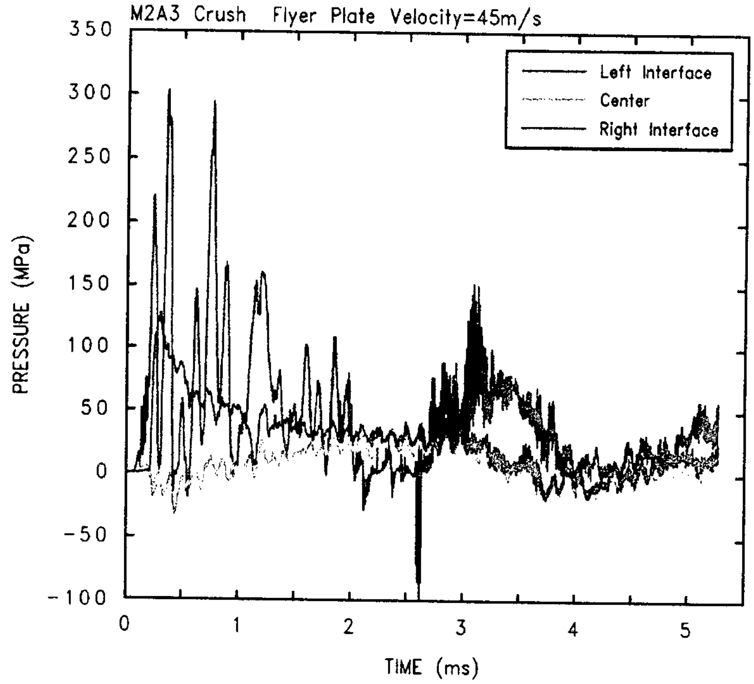

Figure 72. Pressure in the Unreacted Explosive Fill of the M2A3 Munition in Computation CM2-45 (unsmoothed, forward-ordered buffer pack).

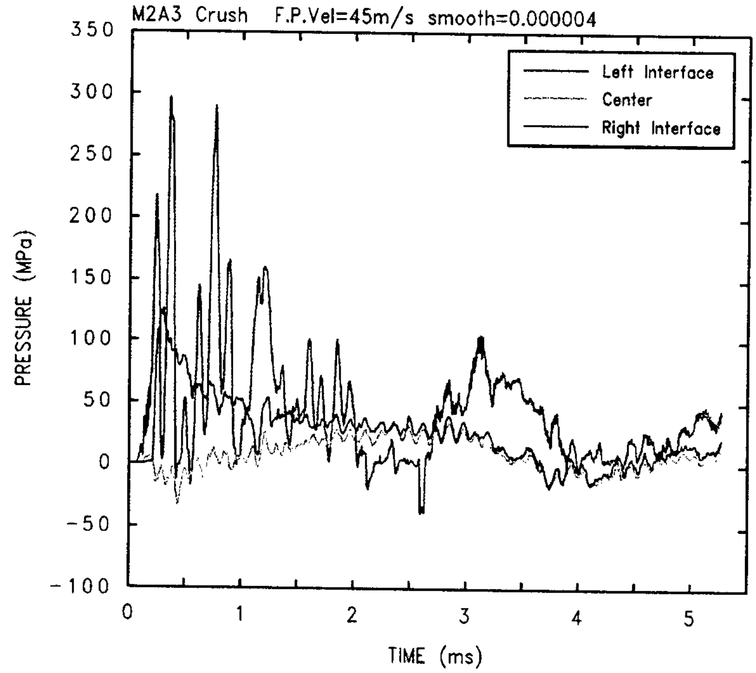

Figure 73. Pressure in the Unreacted Explosive Fill of the M2A3 Munition in Computation CM2-45 (smoothed, forward-ordered buffer pack).

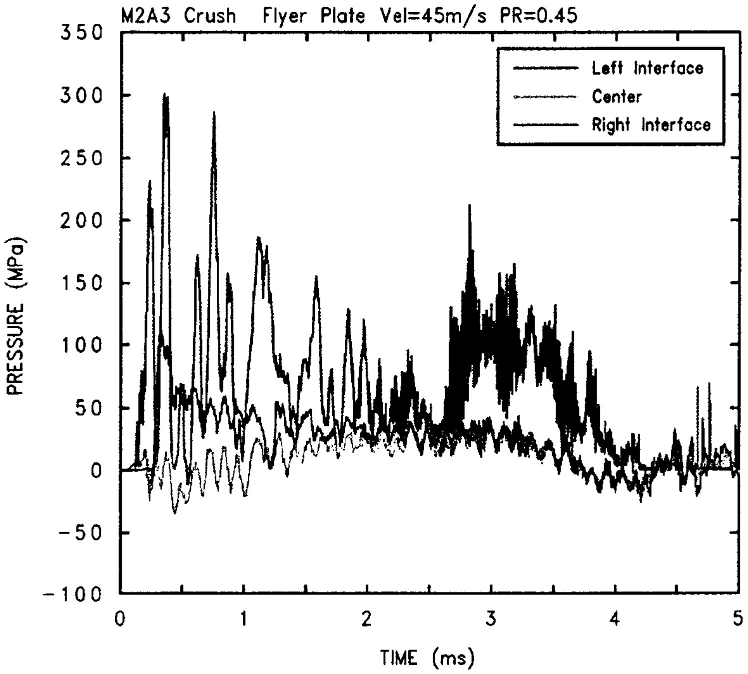

Figure 74. Pressure in the Unreacted Explosive Fill of the M2A3 Munition in Computation CM2-45pr, v = 0.45 (unsmoothed, forward-ordered buffer pack).

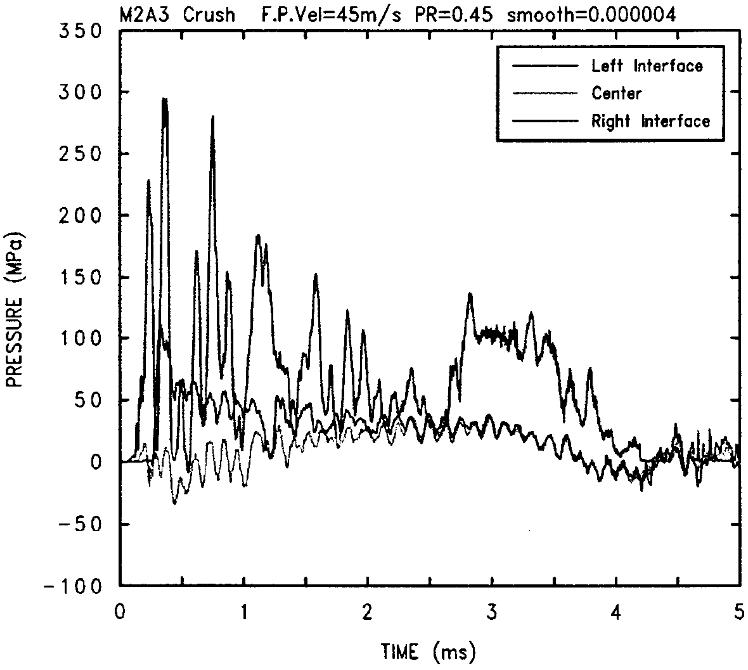

Figure 75. Pressure in the Unreacted Explosive Fill of the M2A3 Munition in Computation CM2-45pr, v = 0.45 (smoothed, forward-ordered buffer pack).

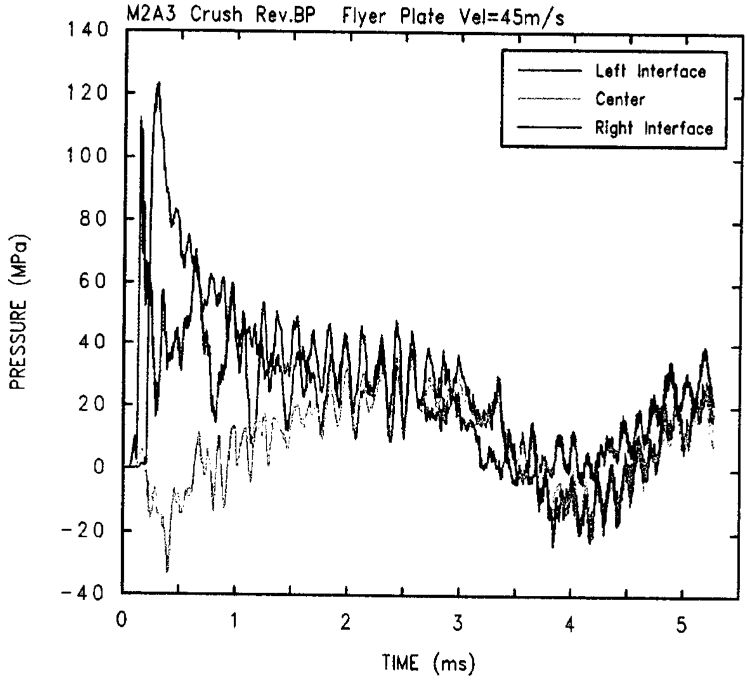

Figure 76. Pressure in the Unreacted Explosive Fill of the M2A3 Munition in Computation CM2-45R (unsmoothed, reverse-ordered buffer pack).

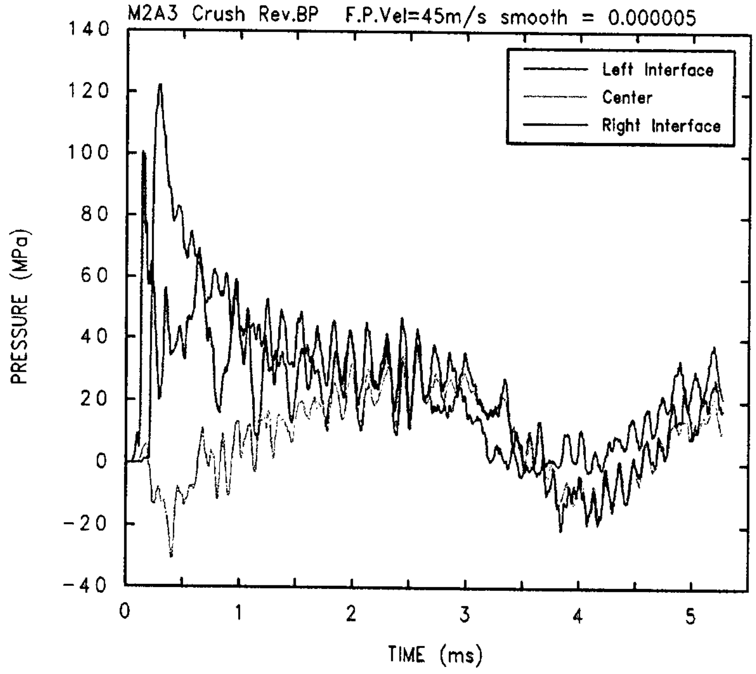

Figure 77. Pressure in the Unreacted Explosive Fill of the M2A3 Munition in Computation CM2-45R (smoothed, reverse-ordered buffer pack).

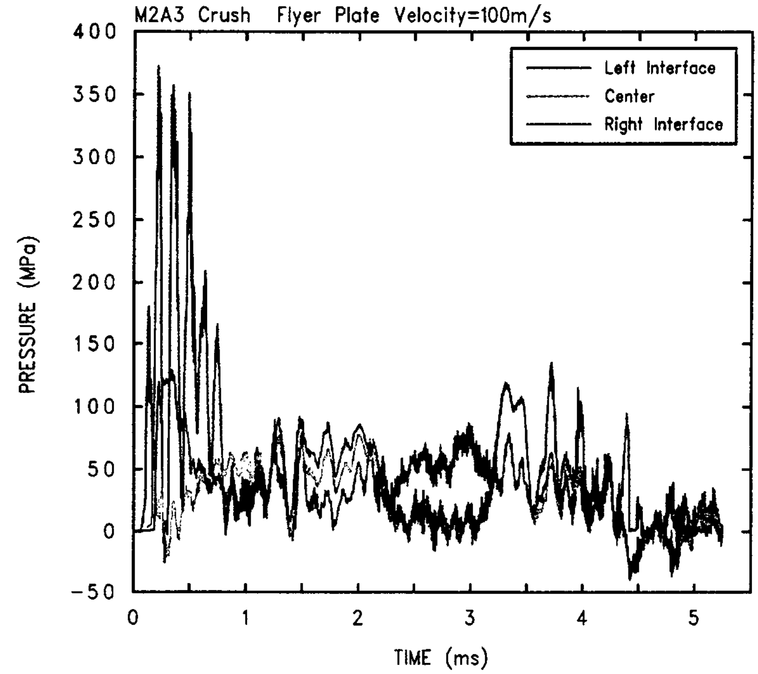

Figure 78. Pressure in the Unreacted Explosive Fill of the M2A3 Munition in Computation CM2-100 (unsmoothed, forward-ordered buffer pack).

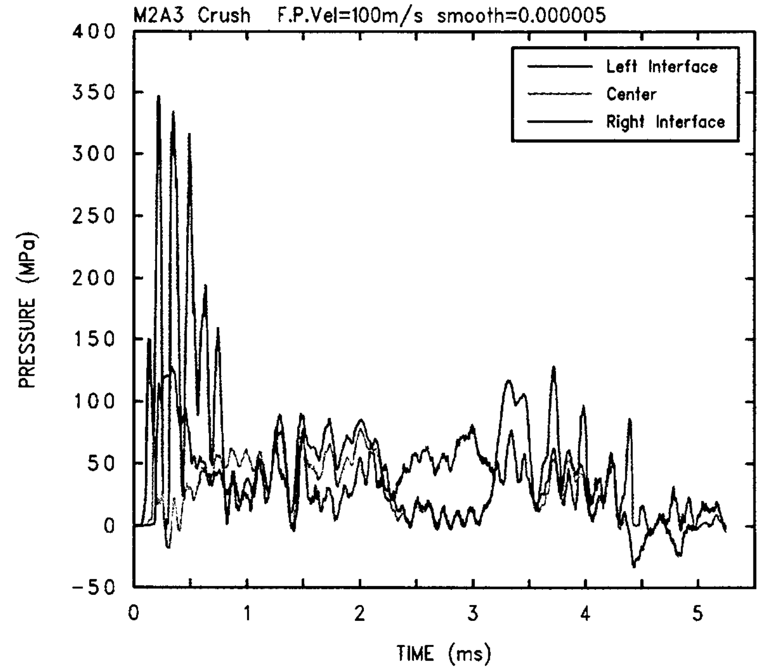

Figure 79. Pressure in the Unreacted Explosive Fill of the M2A3 Munition in Computation CM2-100 (smoothed, forward-ordered buffer pack).

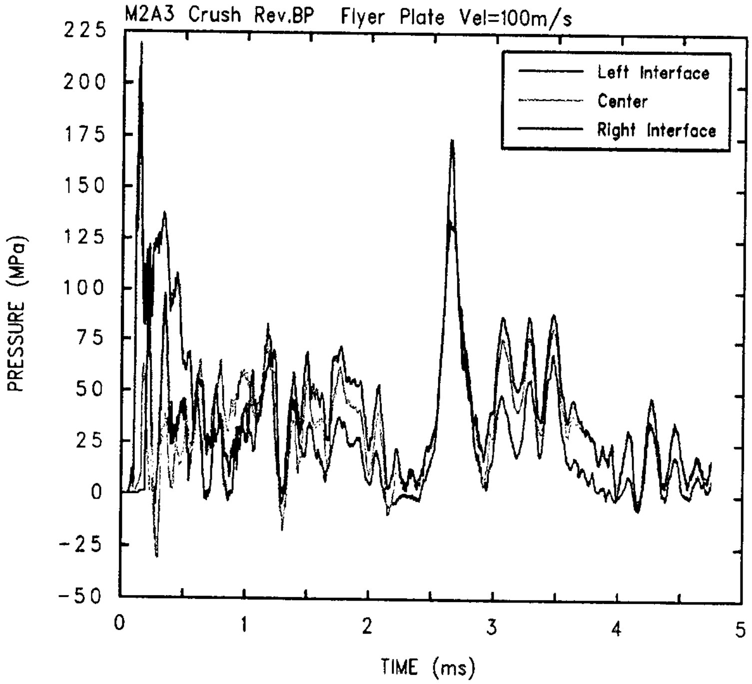

Figure 80. Pressure in the Unreacted Explosive Fill of the M2A3 Munition in Computation CM2-100R (unsmoothed, reverse-ordered buffer pack).

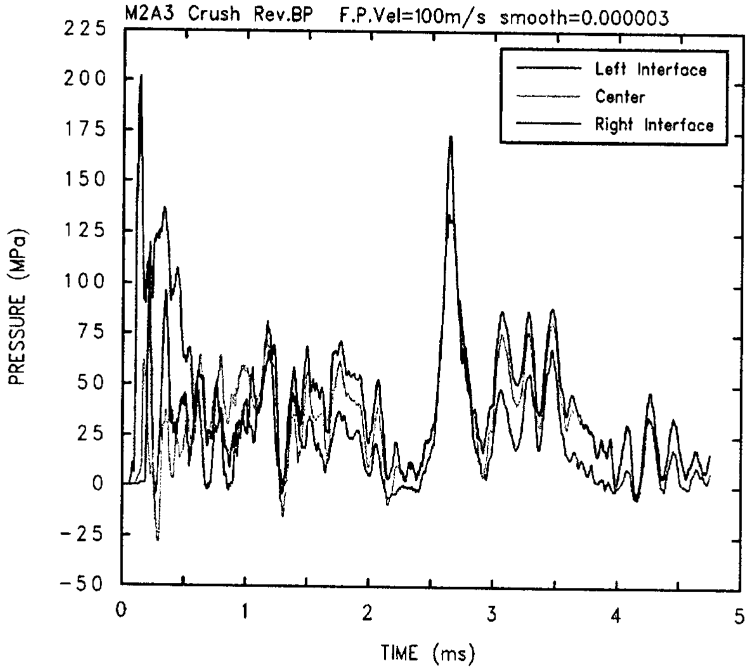

Figure 81. Pressure in the Unreacted Explosive Fill of the M2A3 Munition in Computation CM2-100R (smoothed, reverse-ordered buffer pack).

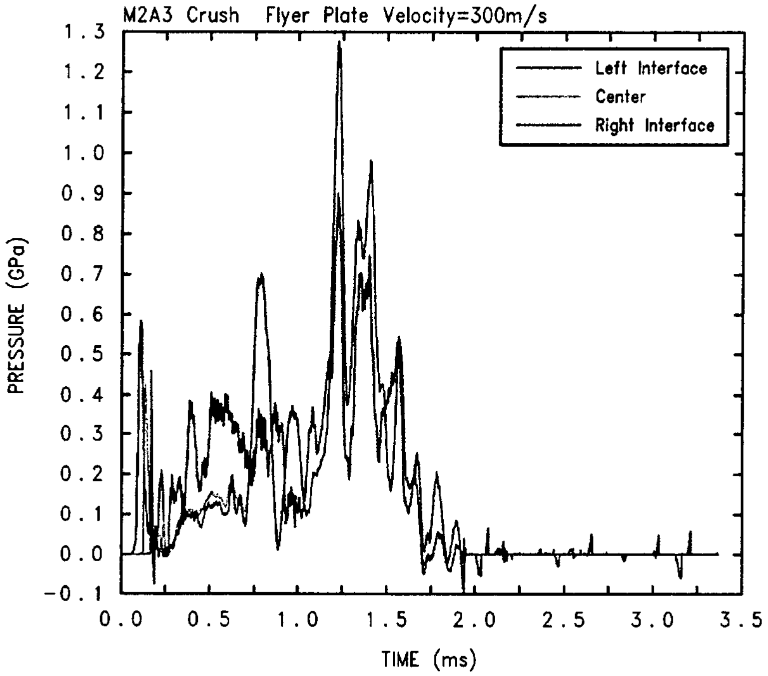

Figure 82. Pressure in the Unreacted Explosive Fill of the M2A3 Munition in Computation CM2-300 (unsmoothed, forward-ordered buffer pack).

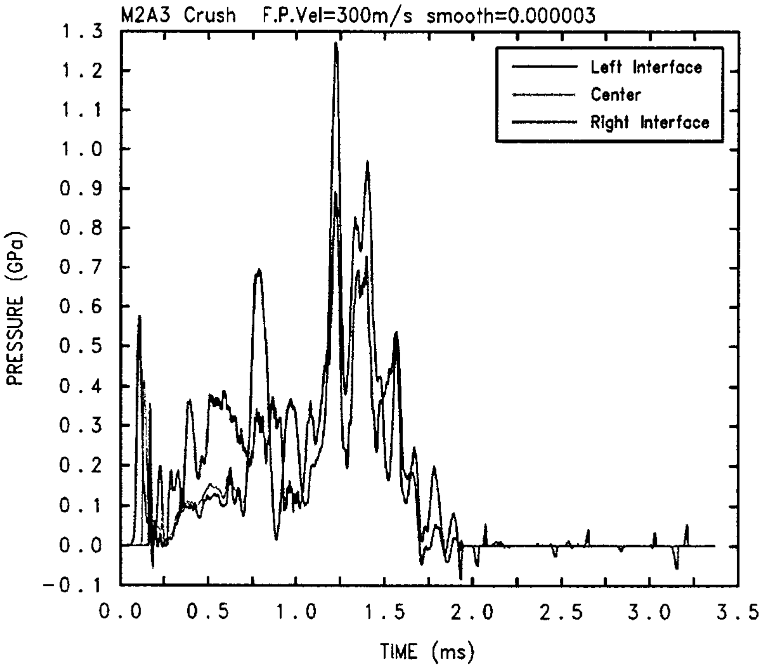

Figure 83. Pressure in the Unreacted Explosive Fill of the M2A3 Munition in Computation CM2-300 (smoothed, forward-ordered buffer pack).

5.2.3 Analysis of the Bulk Motion of the Explosive Fills for the M2A3 Crushing-Impact Computations

Figure 84 shows the X-direction momentum of the flyer plate and the X- and Y-direction momenta of the Comp-B explosive fill of the M2A3 munition versus time in computation CM2-45 (forward-ordered buffer pack). Figure 85 shows the X-direction velocity of the flyer plate and the X- and Y-direction velocities of the Comp-B explosive fill of the M2A3 munition. These velocities were computed as before from the appropriate momentum of the desired material. Figure 86 shows the X-direction acceleration of the flyer plate and the X- and Y-direction accelerations of the Comp-B explosive fill of the M2A3 munition. The early-time accelerations of the explosive fill are somewhat greater than those for DM2-45, while the late-time accelerations are considerably smaller (see Figure 25).

Figure 87 shows the X-direction velocities of the flyer plate for computations CM2-45, CM2-100, and CM2-300. Figure 88 shows a similar set of plots of the bulk X-direction velocity of the explosive fill and Figure 89 shows the bulk Y-direction velocities of the explosive fill for each of the computations. All of these computations simulated a forward-ordered buffer pack.

Figure 90 shows the flyer-plate velocities for computations CM2-45 (forward-ordered buffer pack) and CM2-45R (reverse-ordered buffer pack), Figure 91 shows a similar set of plots of the bulk X-direction velocity of the explosive fill, and Figure 92 shows the bulk Y-direction velocities of the explosive fill for each of the computations. None of these plots show a strong, obvious correlation of differences in the X-direction velocities between the forward- and reverse-ordered configurations of the buffer packs, as were discussed earlier for the smoothed pressure plots in Figures 73 and 77. However, Figure 91 does show a series of greater peaks at early time in the X-direction velocity for CM2-45, which could be indicative of whole-body responses to pressure peaks.

Figure 93 shows the flyer-plate velocities for computations CM2-100 (forward-ordered buffer pack) and CM2-100R (reverse-ordered buffer pack), Figure 94 shows a similar set of plots of the bulk X-direction velocity of the explosive fill, and Figure 95 shows the bulk Y-direction velocities of the explosive fill for each of the computations.

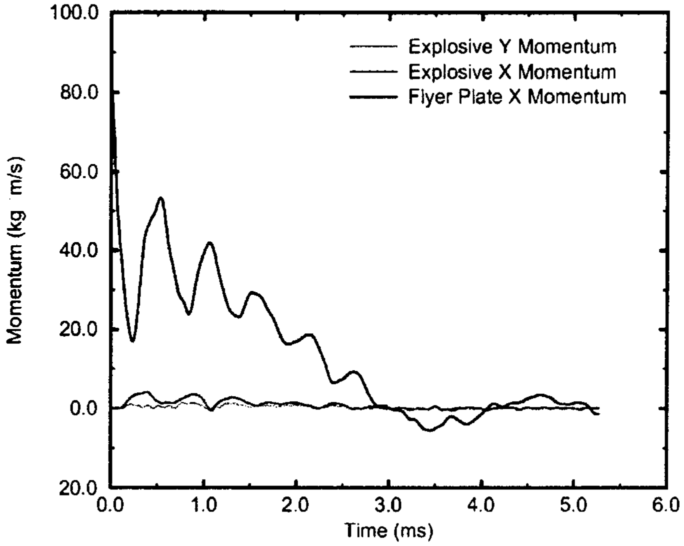

Figure 84. Momenta of the Flyer Plate and the Unreacted Explosive Fill of the M2A3 Munition in Computation CM2-45 (forward-ordered buffer pack).

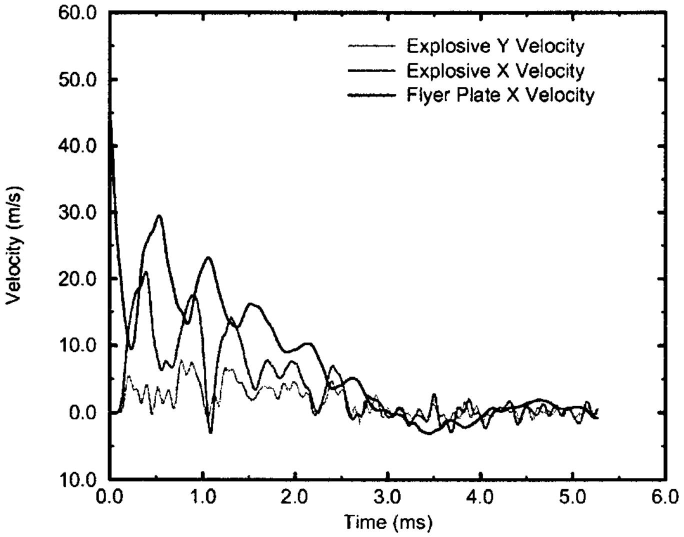

Figure 85. Velocities of the Flyer Plate and the Unreacted Explosive Fill of the M2A3 Munition in Computation CM2-45 (forward-ordered buffer pack).

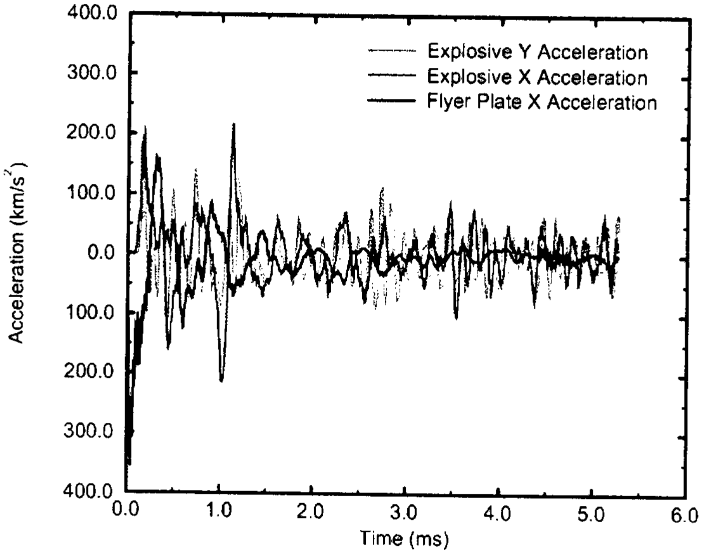

Figure 86. Acceleration of the Flyer Plate and the Unreacted Explosive Fill of the M2A3 Munition in Computation CM2-45 (forward-ordered buffer pack).

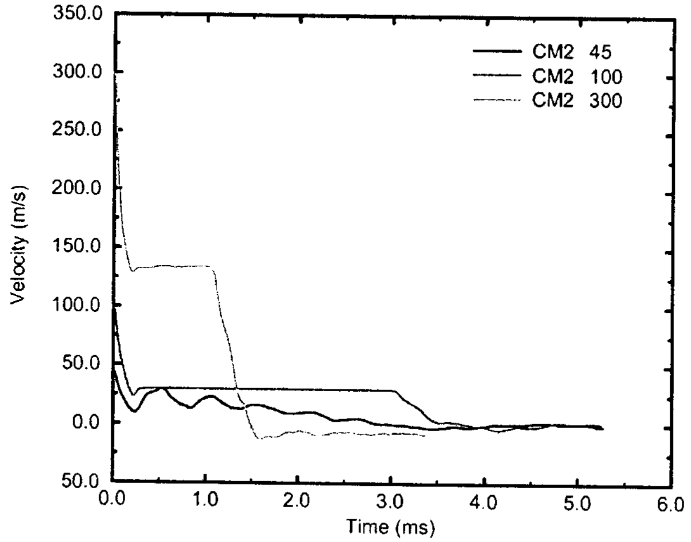

Figure 87. X-Direction Velocities of the Flyer Plate for Each of the Crushing-Impact Computations for the M2A3 Munition (forward-ordered buffer pack).

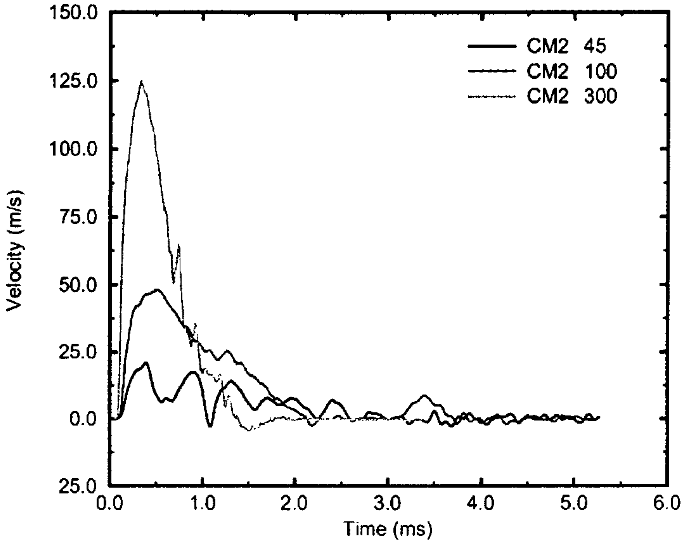

Figure 88. X-Direction Velocities of the Explosive Fill of the M2A3 Munition for Each of the Crushing-Impact Computations (forward-ordered buffer pack).

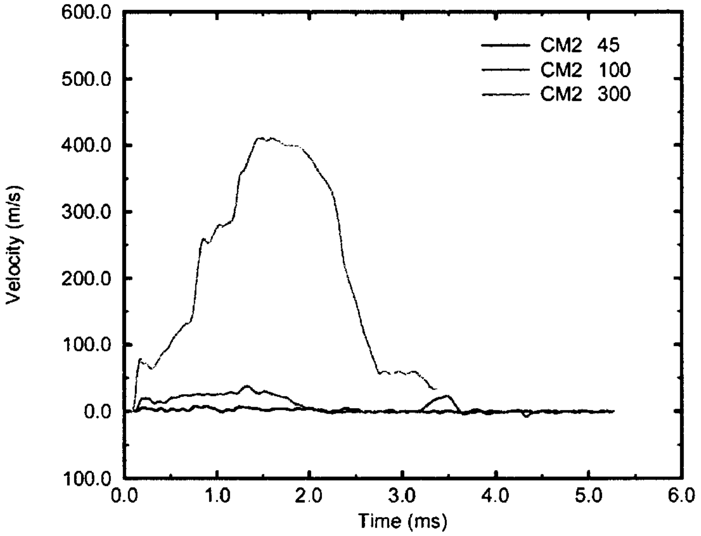

Figure 89. Y-Direction Velocities of the Explosive Fill of the M2A3 Munition for Each of the Crushing-Impact Computations (forward-ordered buffer pack).

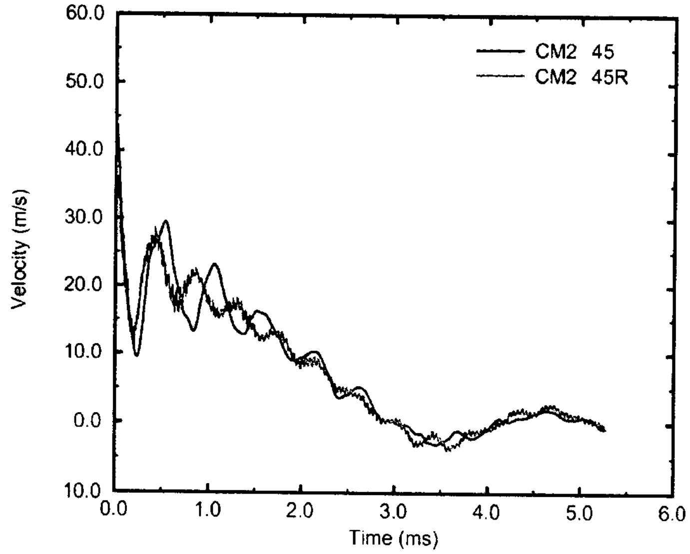

Figure 90. X-Direction Velocities of the Flyer Plate for the 45.0-m/s Crushing-Impact Computations for the M2A3 Munition (forward- versus reverse-ordered buffer pack).

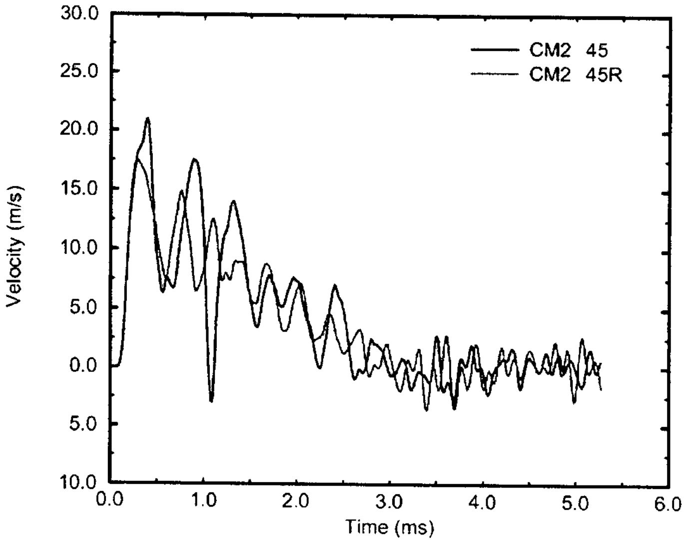

Figure 91. X-Direction Velocities of the Explosive Fill of the M2A3 Munition for the 45.0-m/s Crushing-Impact Computations (forward- versus reverse-ordered buffer pack).

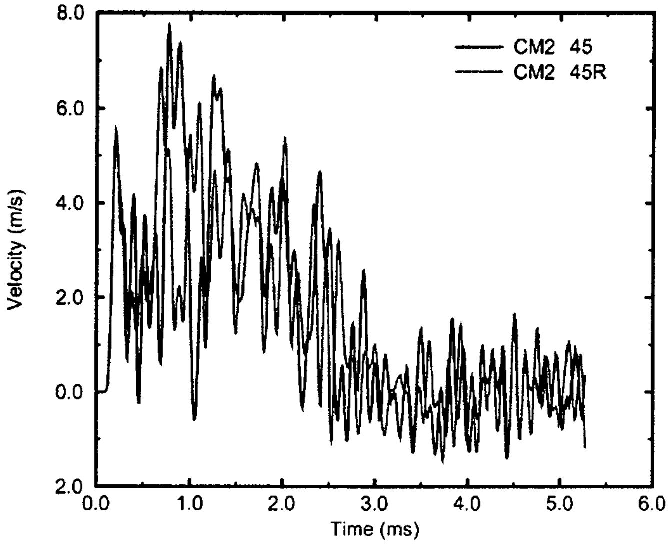

Figure 92. Y-Direction Velocities of the Explosive Fill of the M2A3 Munition for the 45.0-m/s Crushing-Impact Computations (forward- versus reverse-ordered buffer pack).

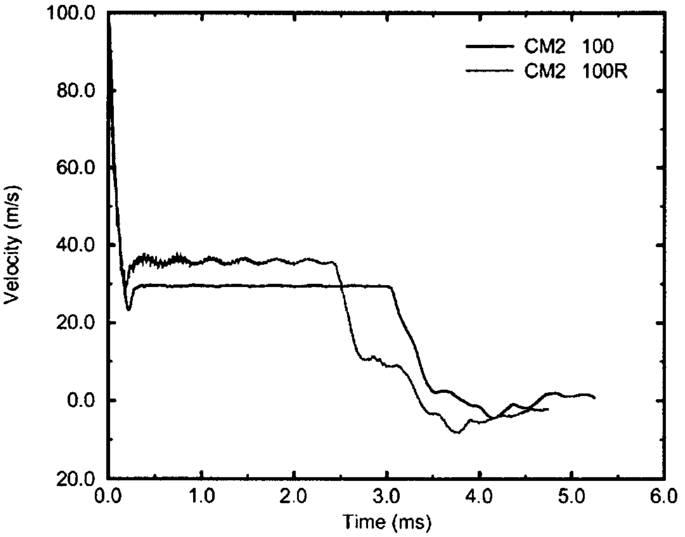

Figure 93. X-Direction Velocities of the Flyer Plate for the 100.0-m/s Crushing-Impact Computations for the M2A3 Munition (forward- versus reverse-ordered buffer pack).

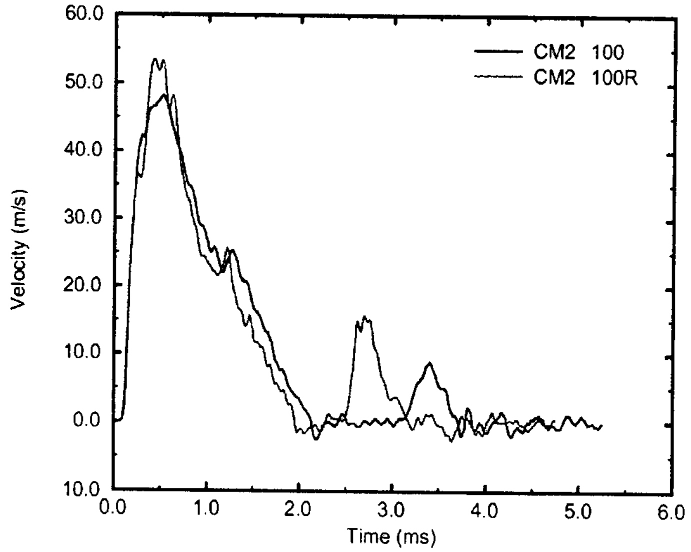

Figure 94. X-Direction Velocities of the Explosive Fill of the M2A3 Munition for the 100.0-m/s Crushing-Impact Computations (forward- versus reverse-ordered buffer pack).

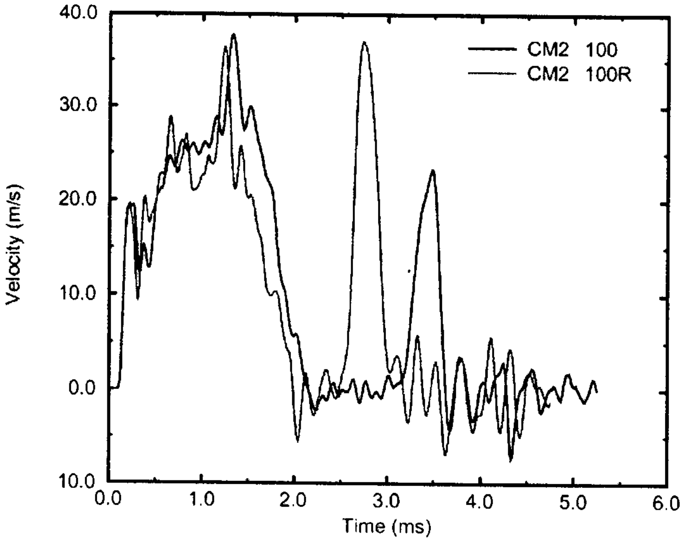

Figure 95. Y-Direction Velocities of the Explosive Fill of the M2A3 Munition for the 100.0-m/s Crushing-Impact Computations (forward- versus reverse-ordered buffer pack).

5.3 Results of the M483 Crushing-Impact Computations

5.3.1 Analysis of the Flow Fields for the M483 Crushing-Impact Computations

Figure 96 shows the flow field for computation CM4-43 at time t = 0.00. Except for the presence of the eight-layer, forward-ordered buffer pack, the right side of the munition touching the right reflective boundary, and the different impact velocity of the flyer plate, this initial flow field is similar to that shown in Figure 42 for DM4-33. The experiment [9] that this computation simulates resulted in a "No Go." Figure 97 shows the flow field for computation CM4-43 at time t = 2.00 ms. There is no directly comparable double-impact computation for the M483 at that same flyer-plate impact velocity. However, comparisons with Figures 43 (double impact at 33.0 m/s) and 47 (double impact at 49.0 m/s) clearly show the different early-time responses of the M483. The double-impact computations both show more compressive distortion at the left side of the M483 than at the right side (not yet in contact with the backing plate) plus a void between the explosive fill and the inside surface of the casing near the "top" of the munition. Conversely, CM4-43 shows nearly symmetric X-direction compression of the M483 and no void developing between the explosive fill and the casing. Figure 98 shows the flow field for computation CM4-43 at time t = 4.00 ms, the ending time of the computation. This can be compared with Figures 45 (double impact at 33.0 m/s) and 49 (double impact at 49.0 m/s), which show more asymmetry in the M483 than does CM4-43 at that same time.

Computation CM4-95 simulated the crushing-impact experiment in which a flyer plate traveling at 95.0 m/s struck the forward-ordered buffer pack and subsequently crushed an M483 155-mm projectile against the backing plate. This resulted in an "Expl" (explosion) reaction in the experiment.[9] The flow field for CM4-95 at t = 0.00 is not shown here because it is identical to that shown in Figure 96 except for the indicated impact velocity of the flyer plate. Figure 99 shows the computational flow field at time t = 1.00 ms. The steel casing of the M483 has already undergone considerable distortion, including an indication of rupture of the casing. Also, a gap has opened between the first Lucite layer and the first steel layer in the buffer pack. This gap is caused by the complex wave interactions within the buffer pack. Figure 100 shows the computational flow field at time t = 4.00 ms, the ending time of the computation. This shows extensive crushing of the casing and extrusion of the explosive fill through the rupture.

Computation CM4-45 simulated the impact of the flyer plate traveling at 45.0 m/s against the combination of the forward-ordered buffer pack and the M483 munition. Except for the initial velocity of the flyer plate, the flow field at time t = 0.00 was the same as that shown in Figure 96. A total time of 4.00 ms was simulated. No flow-field plots for this computation will be shown. Computation CM4-45R simulated the same interaction as for CM4-45, except that a reverse-ordered buffer pack was used in place of the forward-ordered buffer pack. The flow field for CM4-45R at time t = 0.00 is shown in Figure 101. This computation was run for a total simulated time of 4.85 ms. No additional flow-field plots will be shown. There were no corresponding experiments for these computations.

Computation CM4-100 simulated the impact of the flyer plate traveling at 100.0 m/s against the combination of the forward-ordered buffer pack and the M483 munition. Except for the initial velocity of the flyer plate, the flow field at time t = 0.00 was the same as that shown in Figure 96. A total time of 3.77 ms was simulated. Computation CM4-100R simulated the same interaction as for CM4-100, except that a reverse-ordered buffer pack was used in place of the forward-ordered buffer pack. The geometric configuration of the flow field for CM4-100R at time t = 0.00 is the same as that shown in Figure 101. This computation was run for a total simulated time of 5.33 ms. No flow-field plots will be shown for either of these two computations. There were no corresponding experiments.

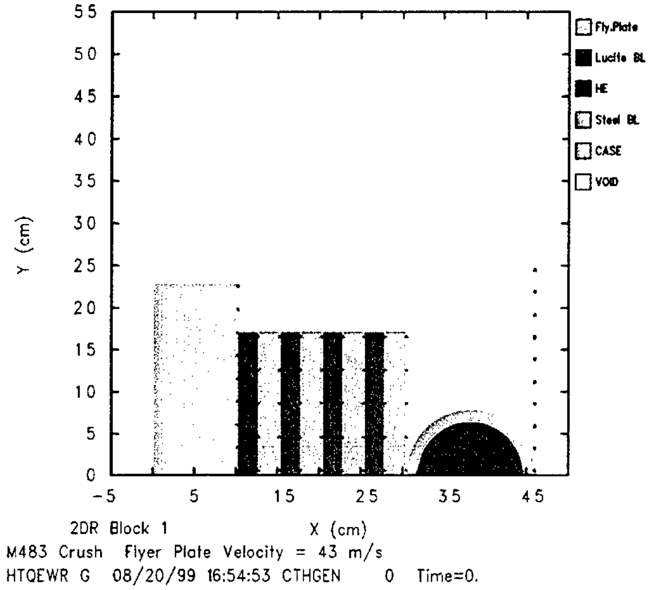

Figure 96. Flow Field at Time = 0.00 for Computation CM4-43, Crushing Impact of a Flyer Plate at 43.0 m/s on a Combination of a Forward-Ordered Buffer Pack and an M483 Munition.

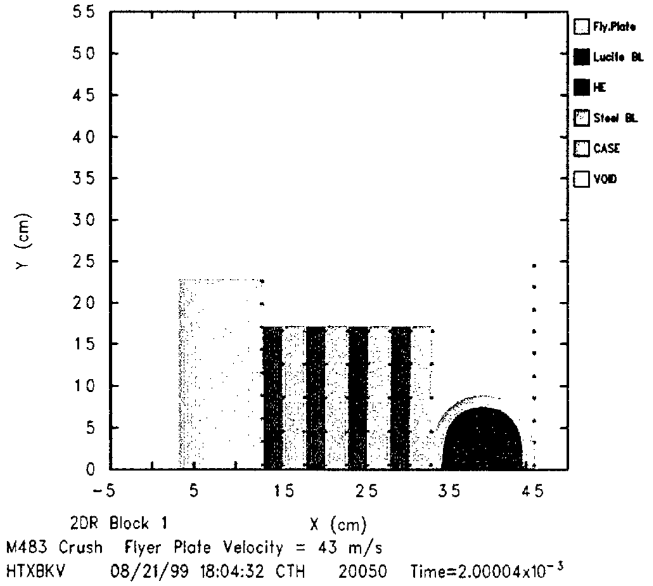

Figure 97. Flow Field at Time = 2.00 ms for Computation CM4-43, Crushing Impact of a Flyer Plate at 43.0 m/s on a Combination of a Forward-Ordered Buffer Pack and an M483 Munition.

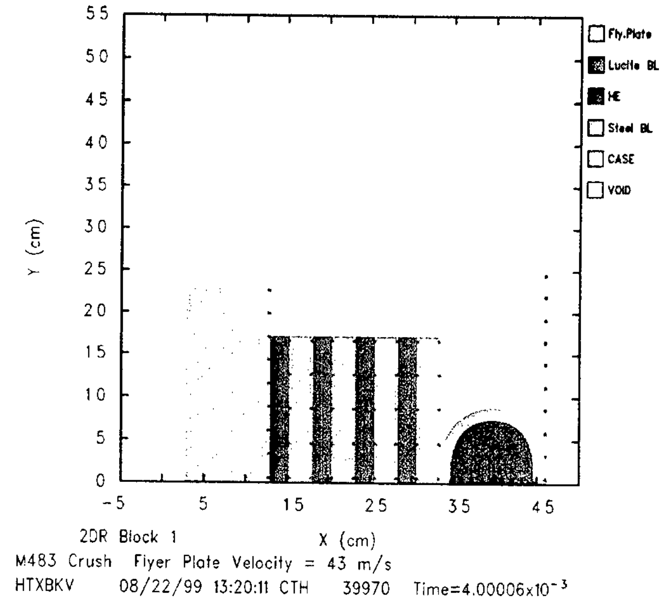

Figure 98. Flow Field at Time = 4.00 ms for Computation CM4-43, Crushing Impact of a Flyer Plate at 43.0 m/s on a Combination of a Forward-Ordered Buffer Pack and an M483 Munition.

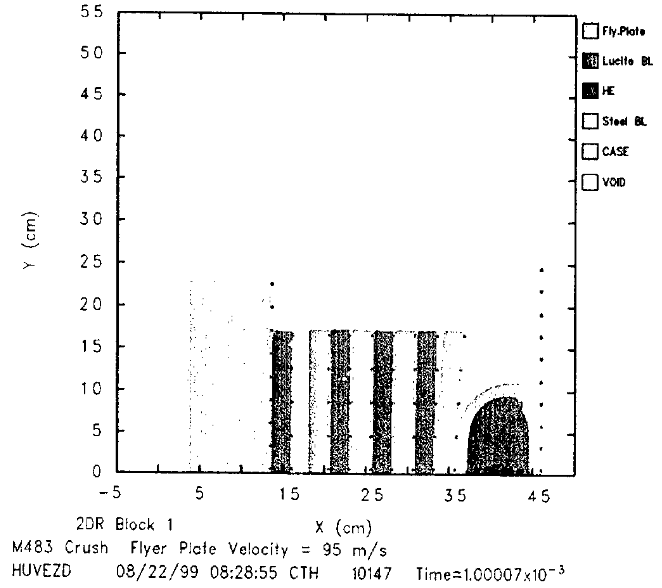

Figure 99. Flow Field at Time = 1.00 ms for Computation CM4-95, Crushing Impact of a Flyer Plate at 95.0 m/s on a Combination of a Forward-Ordered Buffer Pack and an M483 Munition.

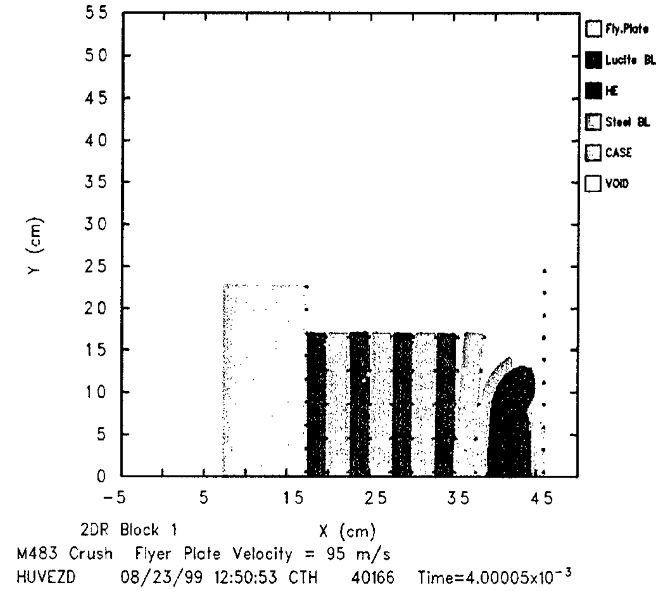

Figure 100. Flow Field at Time = 4.00 ms for Computation CM4-95, Crushing Impact of a Flyer Plate at 95.0 m/s on a Combination of a Forward-Ordered Buffer Pack and an M483 Munition.

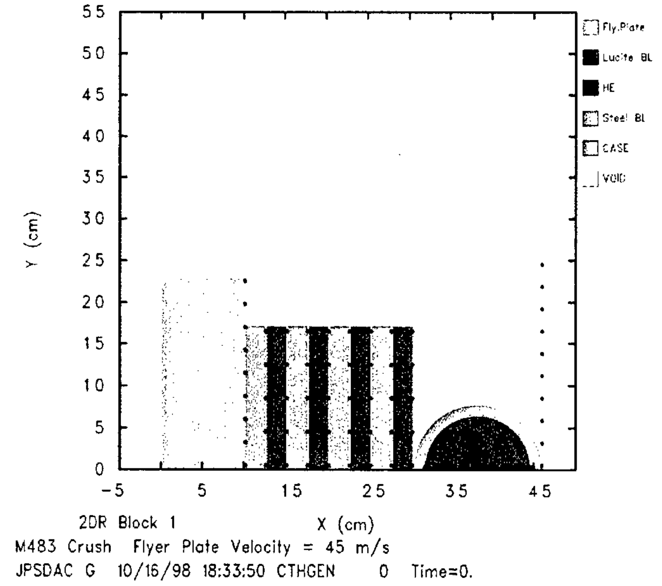

Figure 101. Flow Field at Time = 0.00 for Computation CM4-45R, Crushing Impact of a Flyer Plate at 45.0 m/s on a Combination of a Reverse-Ordered Buffer Pack and an M483 Munition.

5.3.2 Analysis of the Pressure in the Explosive Fills for the M483 Crushing-Impact Computations

Figure 102 shows the unsmoothed pressure at three locations within the unreacted explosive fill of the M483 munition for computation CM4-43 (forward-ordered buffer pack). These three locations and line colors are the same as were first described in the earlier discussion of Figure 51 and will remain the same throughout this section. Figure 103 shows the same pressures as were shown in Figure 102 except that a smoothing parameter τ = $6.0x10^{-6}$ was applied. Comparisons with the unsmoothed pressure plots for DM4-33 (see Figure 51) and DM4-49 (see Figure 53) and their smoothed counterparts are interesting in their almost counter-intuitive dynamics. The greatest peak in pressure of the three computations was just under 2.5 kbar for the smoothed pressure near the right interface of the explosive fill for DM4-33 (see Figure 52), with the smoothed curves for the other locations in that figure showing peaks of about half that value. This was the double-impact computation at the lower of the two velocities discussed in detail in a previous section. The double-impact computation DM4-49 showed its greatest smoothed peak, considerably lower at about 2.1 kbar (see Figure 54), at the left interface, with the smoothed peaks for the other points shown in that figure at 1.5 kbar (right interface) and 1.8 kbar (center). The crushing-impact computation CM4-43 showed smoothed pressure peaks for both the left and right interfaces at about 1.8 kbar (see Figure 103), with the smoothed peak for the center at a similar value of about 1.6 kbar. Thus, the crushing impact at 43.0 m/s produced a somewhat more uniform pressure field in the explosive at an intermediate value between the more varied fields for the double-impact computations, with the lower speed double-impact computation producing the greatest smoothed pressure peak of the three.

Figure 104 shows the pressure at the three locations within the unreacted explosive fill of the M483 munition for computation CM4-95 (forward-ordered buffer pack). Figure 105 shows the same pressures as were shown in Figure 104 except that a smoothing parameter τ = $3.0x10^{-6}$ has been applied. The smoothed pressures for each of the three points show the largest values ranging around 2.75 kbar (with the right interface highest at 3.0 kbar) during the early-time interaction at about 0.62 ms.

Figure 106 shows the pressure at the three locations within the unreacted explosive fill of the M483 munition for computation CM4-45 (forward-ordered buffer pack). Figure 107 shows the same pressures as were shown in Figure 106 except that a smoothing parameter τ = $6.0x10^{-6}$ has been applied. Figure 108 shows the pressure at three locations within the unreacted explosive fill of the M483 munition for computation CM4-45R (reverse-ordered buffer pack). Figure 109 shows the same pressures as were shown in Figure 108 except that a smoothing parameter τ = $9.0x10^{-6}$ has been applied. A comparison between the smoothed pressures for the forward-ordered buffer pack shown in Figure 107 with those for the reverse-ordered buffer pack shown in Figure 109 indicates that there are only minor differences in pressure in the explosive fill. Peak pressures (smoothed) are approximately 2.0 kbar. A comparison with the smoothed pressures in the explosive fill for the double-impact computation DM4-45 shown in Figure 56 for the M483 at the same impact velocity indicates that while the timing of the peak values is later in DM4-45, the peak values themselves are also approximately 2.0 kbar. This is contrary to the trends and values in smoothed peak pressure noted in the discussion of computations DM2-45, CM2-45, and CM2-45R. The heavy steel casing of the M483 is apparently a significant mitigating factor for these different physical configurations for impact by a steel flyer plate at 45.0 m/s.

Figure 110 shows the pressure at the three locations within the unreacted explosive fill of the M483 munition for computation CM4-100 (forward-ordered buffer pack). Figure 111 shows the same pressures as were shown in Figure 110 except that a smoothing parameter $\tau = 7.0x10^{-6}$ has been applied. Figure 112 shows the pressure at three locations within the unreacted explosive fill of the M483 munition for computation CM4-100R (reverse-ordered buffer pack). Figure 113 shows the same pressures as were shown in Figure 112 except that a smoothing parameter $\tau = 6.0x10^{-6}$ has been applied. The smoothed pressure plots in Figures 111 and 113 show only moderate differences at the center and right interfaces; these differences are caused by the simulation of forward- versus reverse-ordered buffer packs. At the left interface, while the initial peaks occurring at about 0.2 ms are similar and near 2.0 kbar, CM4-100R shows a more rapid drop in pressure, with its succeeding peaks being around 0.5 to 0.7 kbar. CM4-100 has a second peak of approximately 1.5 kbar, followed by a rapid decrease and then another increase to 1.5 kbar. A comparison with the smoothed pressure for the explosive fill for computation DM4-100 shown in Figure 58 shows that DM4-100 has all three points with very similar pressures to one another but different from those for the crushing-impact computations, with the greatest peak pressure being approximately 3.0 kbar, about 50 percent higher, occurring after the rupture of the casing.

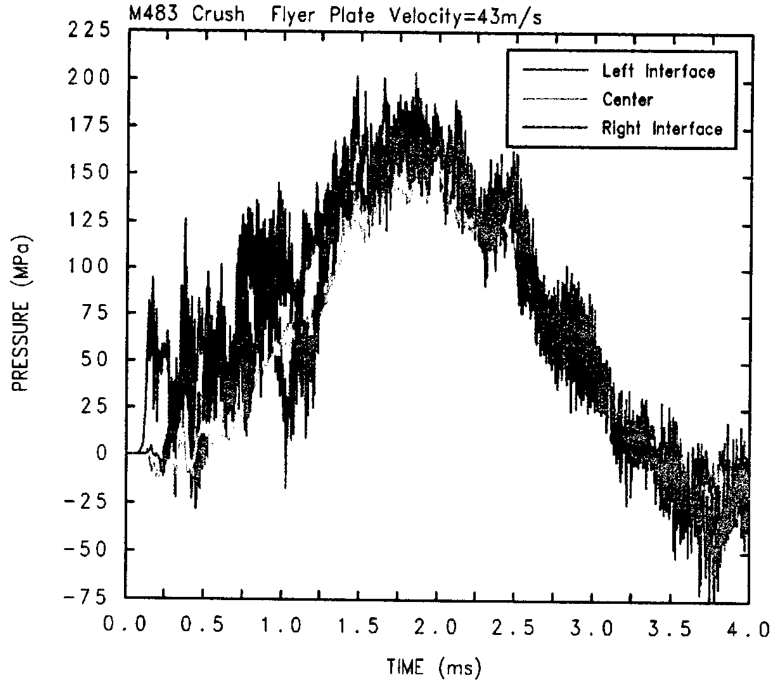

Figure 102. Pressure in the Unreacted Explosive Fill of the M483 Munition in Computation CM4-43 (unsmoothed, forward-ordered buffer pack).

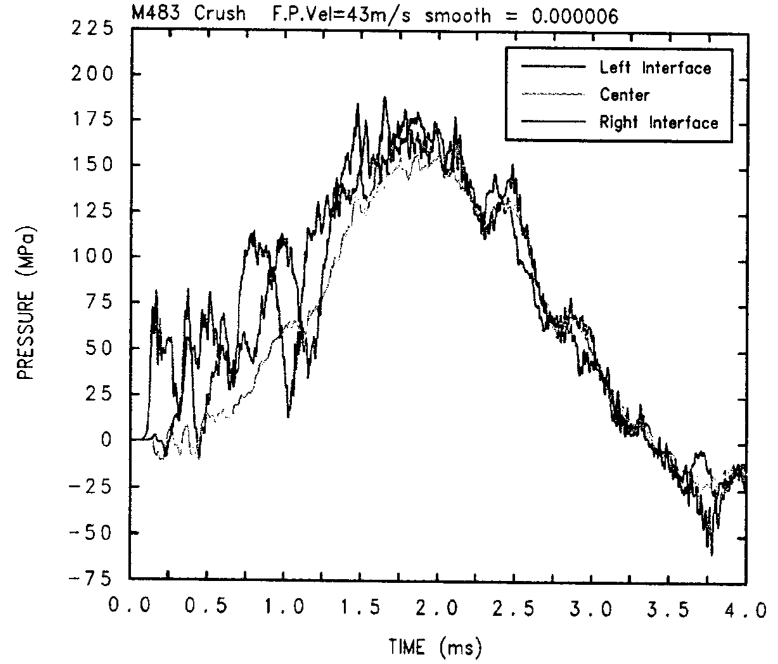

Figure 103. Pressure in the Unreacted Explosive Fill of the M483 Munition in Computation CM4-43 (smoothed, forward-ordered buffer pack).

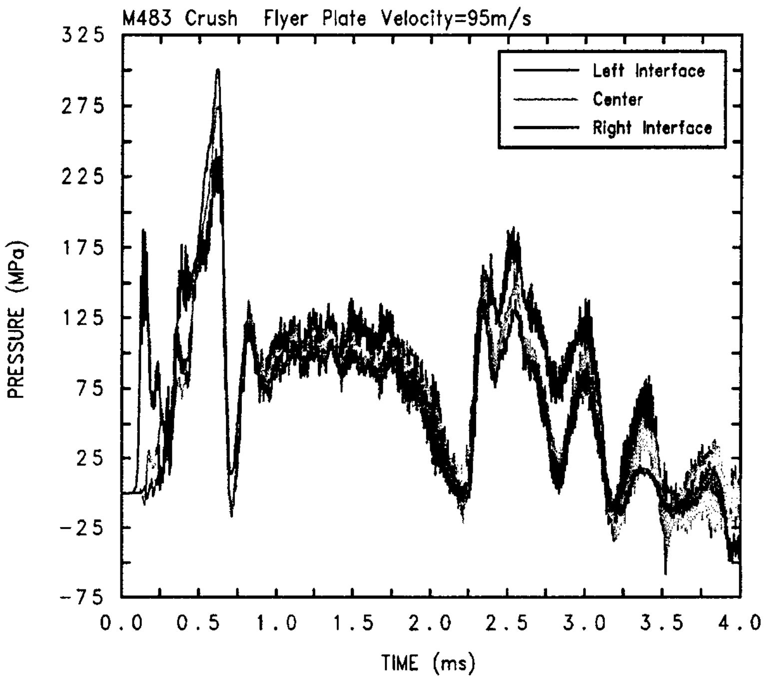

Figure 104. Pressure in the Unreacted Explosive Fill of the M483 Munition in Computation CM4-95 (unsmoothed, forward-ordered buffer pack).

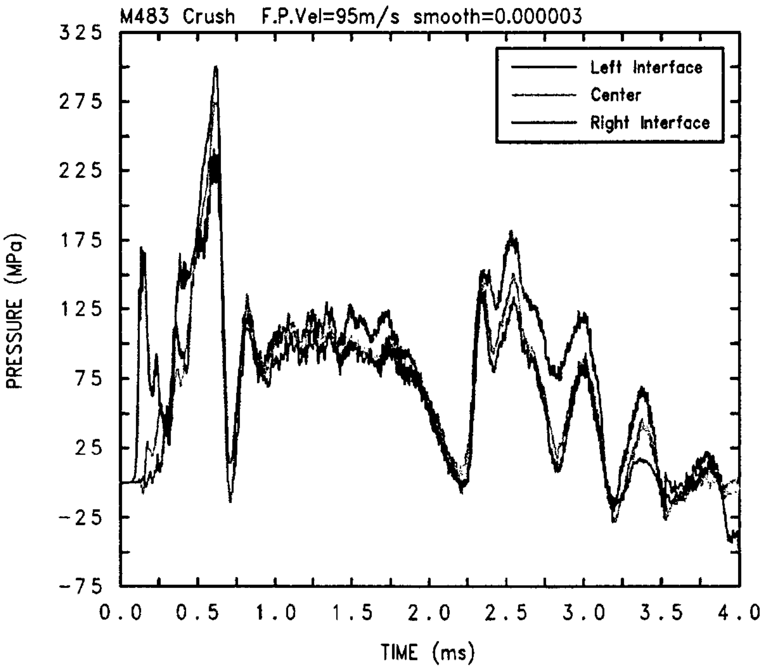

Figure 105. Pressure in the Unreacted Explosive Fill of the M483 Munition in Computation CM4-95 (smoothed, forward-ordered buffer pack).

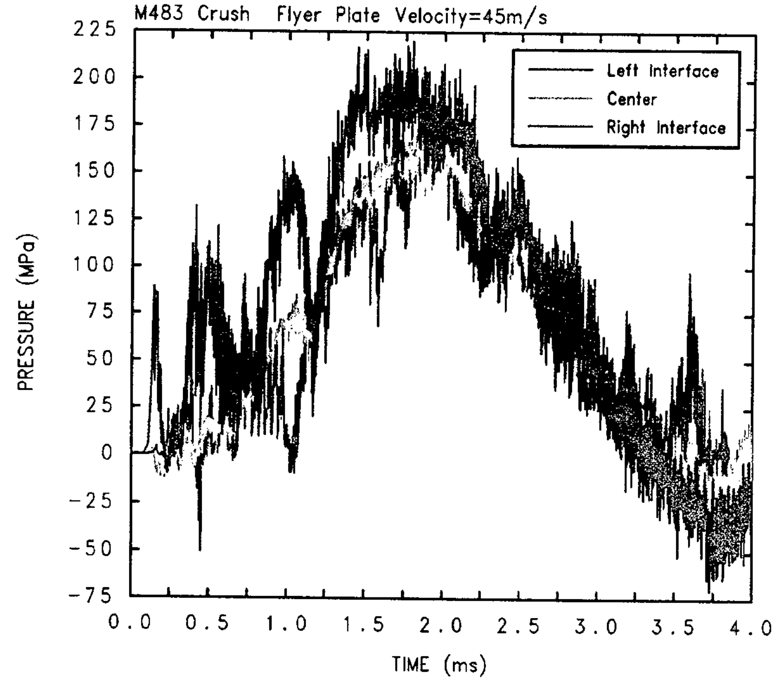

Figure 106. Pressure in the Unreacted Explosive Fill of the M483 Munition in Computation CM4-45 (unsmoothed, forward-ordered buffer pack).

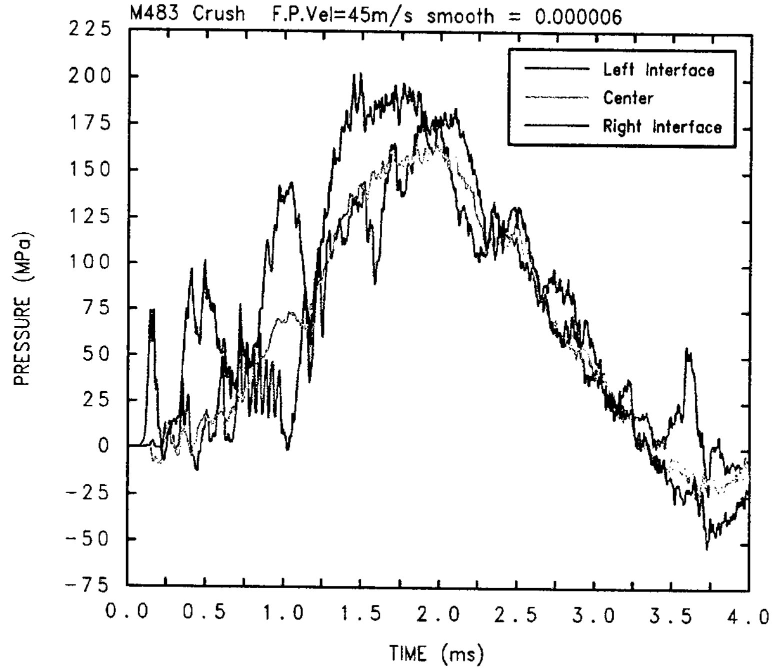

Figure 107. Pressure in the Unreacted Explosive Fill of the M483 Munition in Computation CM4-45 (smoothed, forward-ordered buffer pack).

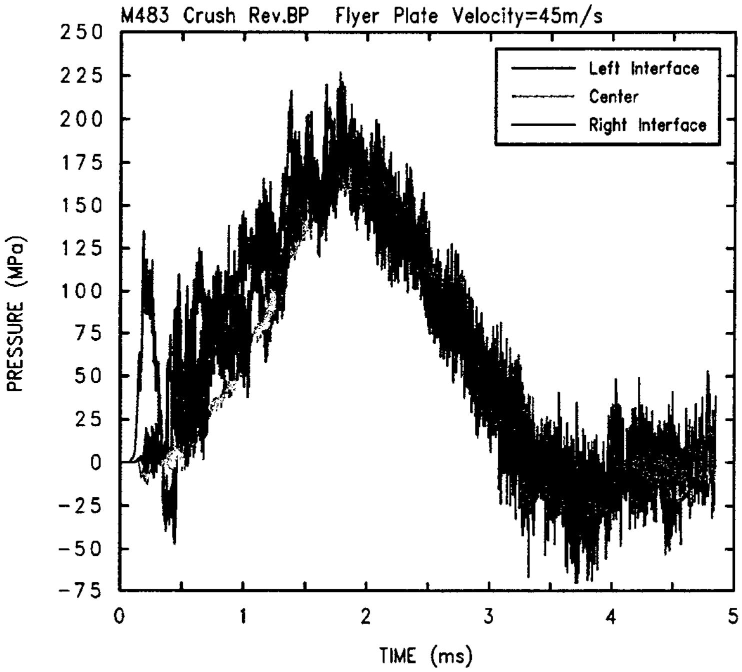

Figure 108. Pressure in the Unreacted Explosive Fill of the M483 Munition in Computation CM4-45R (unsmoothed, reverse-ordered buffer pack).

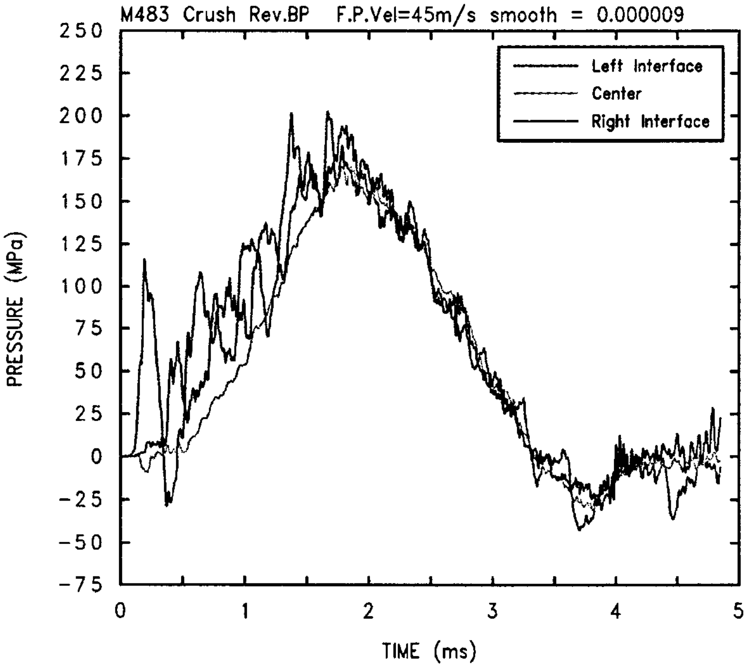

Figure 109. Pressure in the Unreacted Explosive Fill of the M483 Munition in Computation CM4-45R (smoothed, reverse-ordered buffer pack).

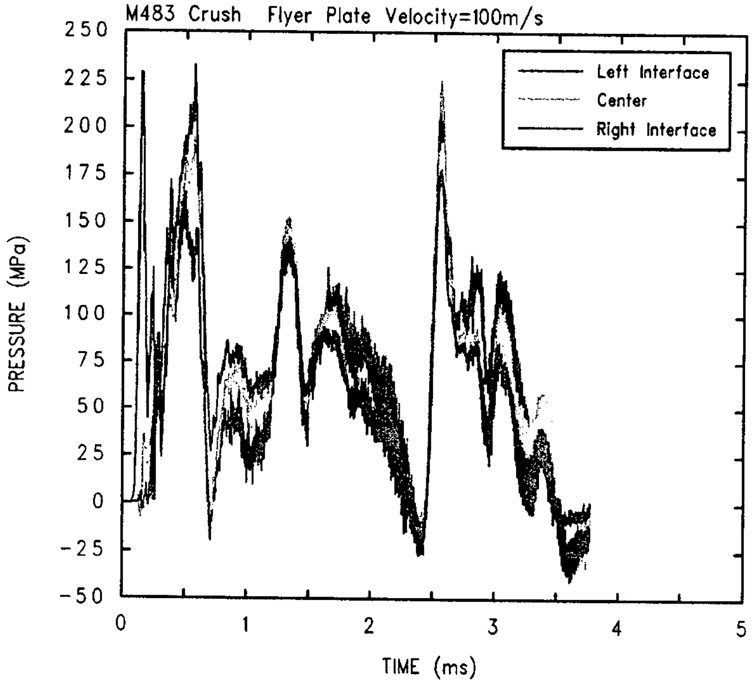

Figure 110. Pressure in the Unreacted Explosive Fill of the M483 Munition in Computation CM4-100 (unsmoothed, forward-ordered buffer pack).

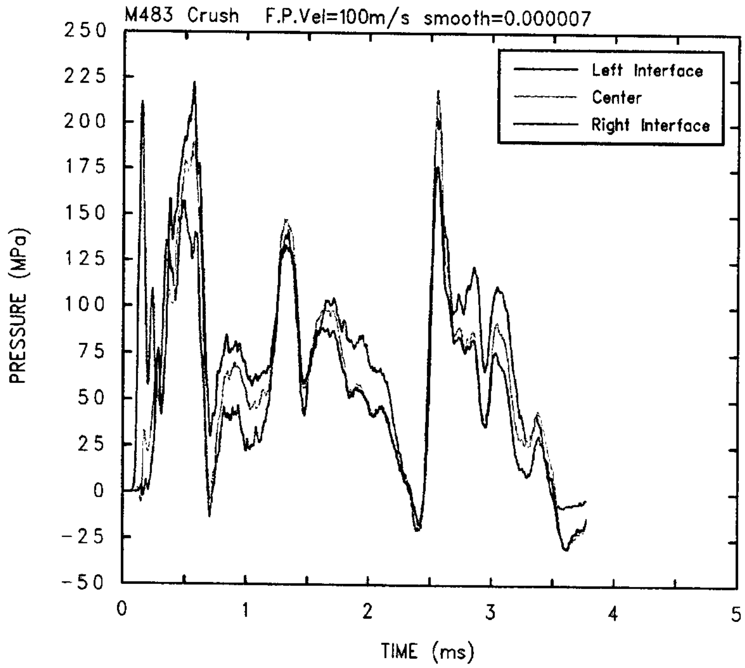

Figure 111. Pressure in the Unreacted Explosive Fill of the M483 Munition in Computation CM4-100 (smoothed, forward-ordered buffer pack).

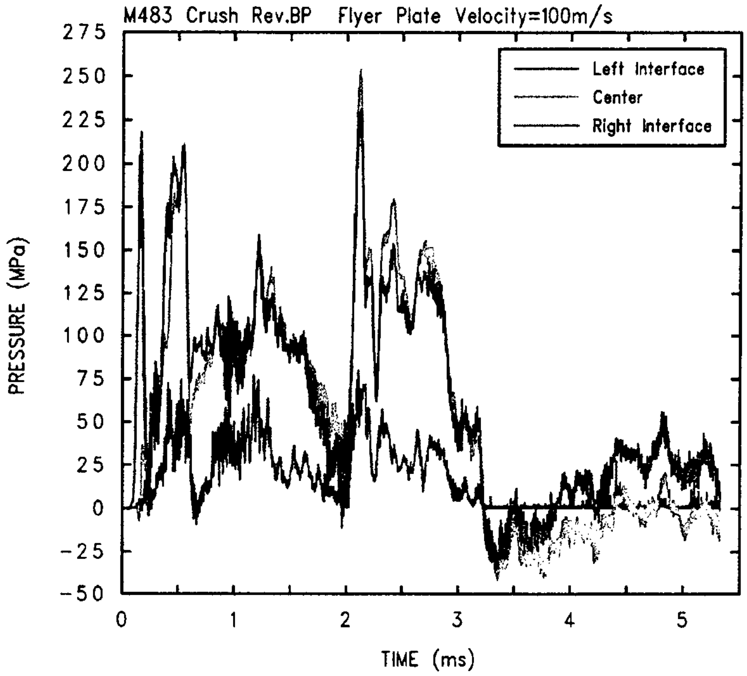

Figure 112. Pressure in the Unreacted Explosive Fill of the M483 Munition in Computation CM4-100R (unsmoothed, reverse-ordered buffer pack).

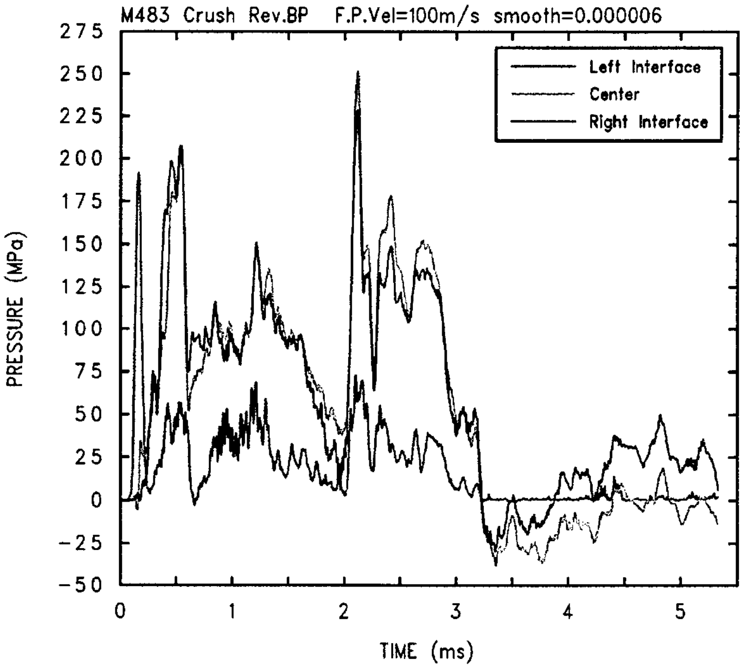

Figure 113. Pressure in the Unreacted Explosive Fill of the M483 Munition in Computation CM4-100R (smoothed, reverse-ordered buffer pack).

5.3.3 Analysis of the Bulk Motion of the Explosive Fills for the M483 Crushing-Impact Computations

Figure 114 shows the X-direction momentum of the flyer plate and the X- and Y-direction momenta of the unreacted explosive fill of the M483 munition versus time in computation CM4-43 (forward-ordered buffer pack). Figure 115 shows the X-direction velocity of the flyer plate and the X- and Y-direction velocities of the unreacted explosive fill of the M483 munition. These velocities were computed as described previously. Figure 116 shows the X-direction acceleration of the flyer plate and the X- and Y-direction accelerations of the unreacted explosive fill of the M483 munition. These accelerations were also computed as described previously.

Figure 117 shows the X-direction momentum and the X- and Y-direction momenta of the unreacted explosive fill of the M483 munition versus time in computation CM4-95. Figure 118 shows the X-direction velocity of the flyer plate and the X- and Y-direction velocities of the unreacted explosive fill of the M483 munition. Figure 119 shows the X-direction acceleration of the flyer plate and the X- and Y-direction accelerations of the unreacted explosive fill of the M483 munition.

Figure 120 shows the X-direction velocities of the flyer plate for computations CM4-43, CM4-45, CM4-95, and CM4-100. Figure 121 shows a similar set of plots of the bulk X-direction velocity of the explosive fill, and Figure 122 shows the bulk Y-direction velocities of the explosive fill for each of the computations. All of these computations simulated a forward-ordered buffer pack.

Figure 123 shows the flyer-plate velocities for computations CM4-45 (forward-ordered buffer pack) and CM4-45R (reverse-ordered buffer pack), Figure 124 shows a similar set of plots of the bulk X-direction velocity of the explosive fill, and Figure 125 shows the bulk Y-direction velocities of the explosive fill for each of the computations. Figure 126 shows the flyer-plate velocities for computations CM4-100 (forward-ordered buffer pack) and CM4-100R (reverse-ordered buffer pack), Figure 127 shows a similar set of plots of the bulk X-direction velocity of the explosive fill, and Figure 128 shows the bulk Y-direction velocities of the explosive fill for each of the computations. Taken together, these plots show relatively few differences in bulk motion that could be attributed to having a forward- versus reverse-ordered buffer pack.

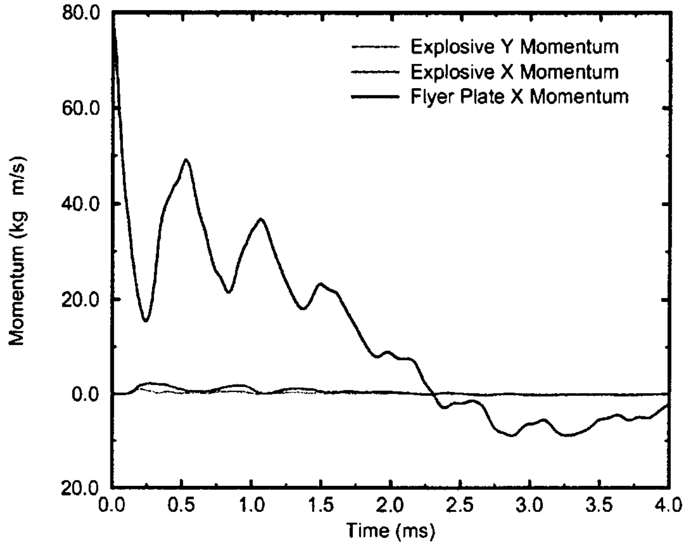

Figure 114. Momenta of the Flyer Plate and the Unreacted Explosive Fill of the M483 Munition in Computation CM4-43 (forward-ordered buffer pack).

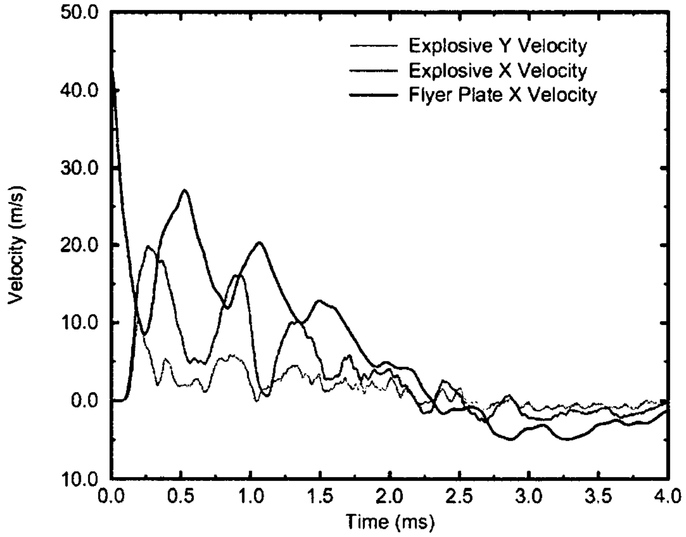

Figure 115. Velocities of the Flyer Plate and the Unreacted Explosive Fill of the M483 Munition in Computation CM4-43 (forward-ordered buffer pack).

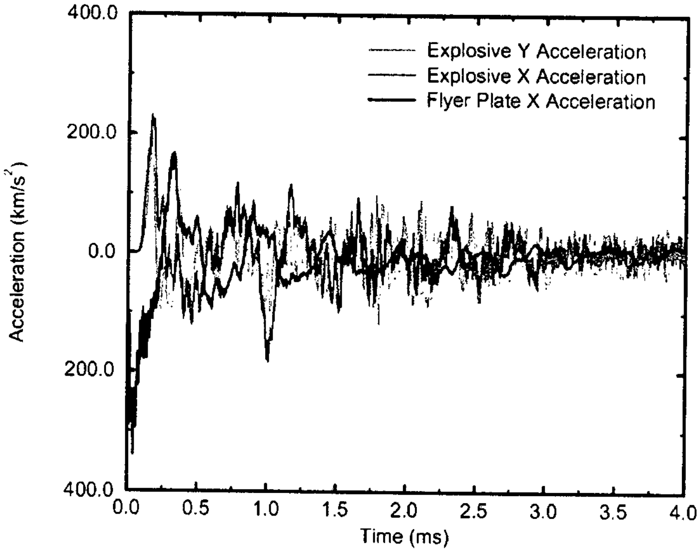

Figure 116. Accelerations of the Flyer Plate and the Unreacted Explosive Fill of the M483 Munition in Computation CM4-43 (forward-ordered buffer pack).

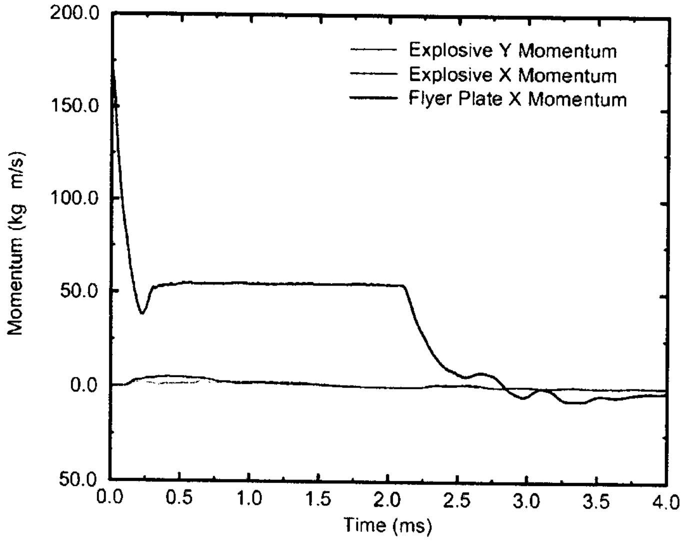

Figure 117. Momenta of the Flyer Plate and the Unreacted Explosive Fill of the M483 Munition in Computation CM4-95 (forward-ordered buffer pack).

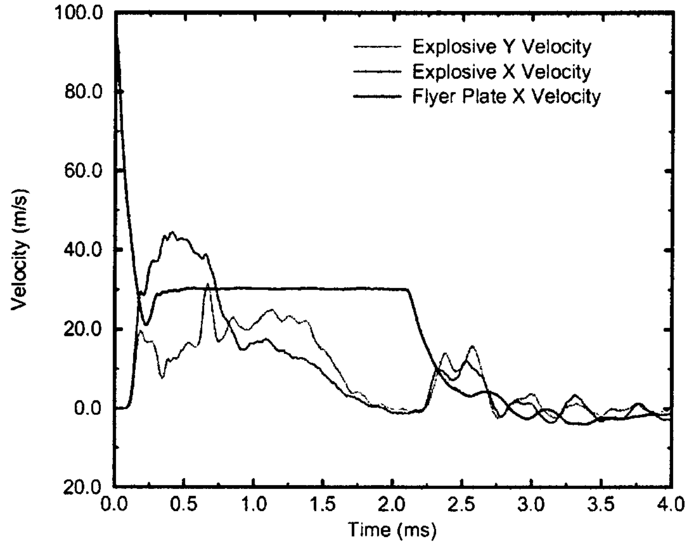

Figure 118. Velocities of the Flyer Plate and the Unreacted Explosive Fill of the M483 Munition in Computation CM4-95 (forward-ordered buffer pack).

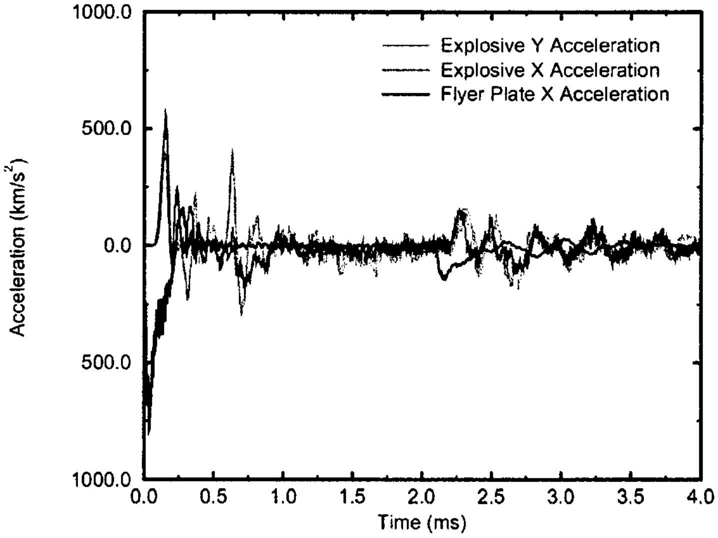

Figure 119. Accelerations of the Flyer Plate and the Unreacted Explosive Fill of the M483 Munition in Computation CM4-95 (forward-ordered buffer pack).

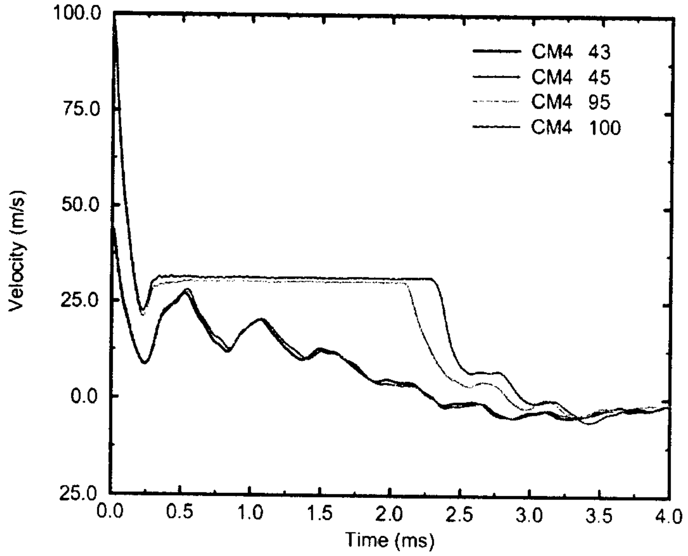

Figure 120. X-Direction Velocities of the Flyer Plate for Each of the Crushing-Impact Computations for the M483 Munition (forward-ordered buffer pack).

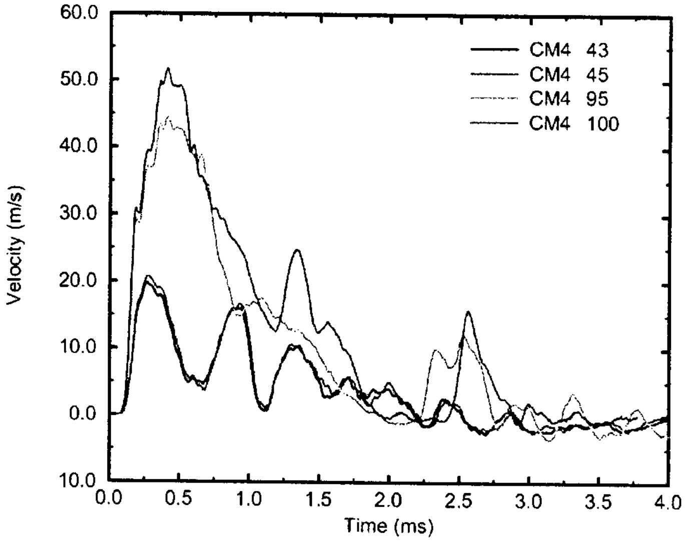

Figure 121. X-Direction Velocities of the Explosive Fill of the M483 Munition for Each of the Crushing-Impact Computations (forward-ordered buffer pack).

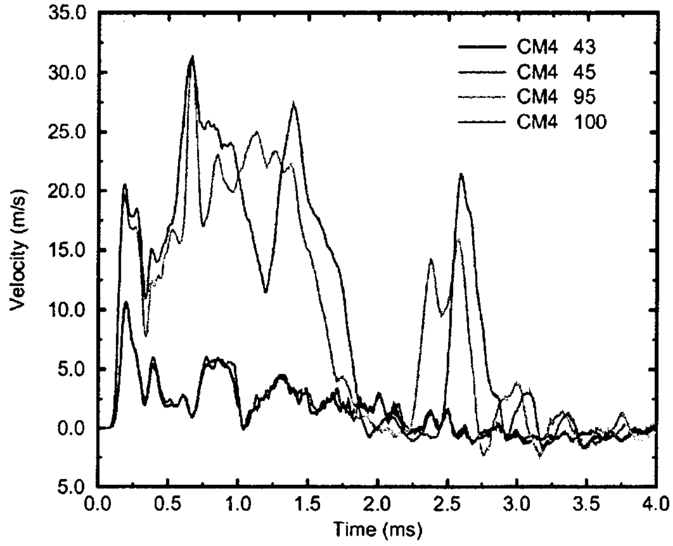

Figure 122. Y-Direction Velocities of the Explosive Fill of the M483 Munition for Each of the Crushing-Impact Computations (forward-ordered buffer pack).

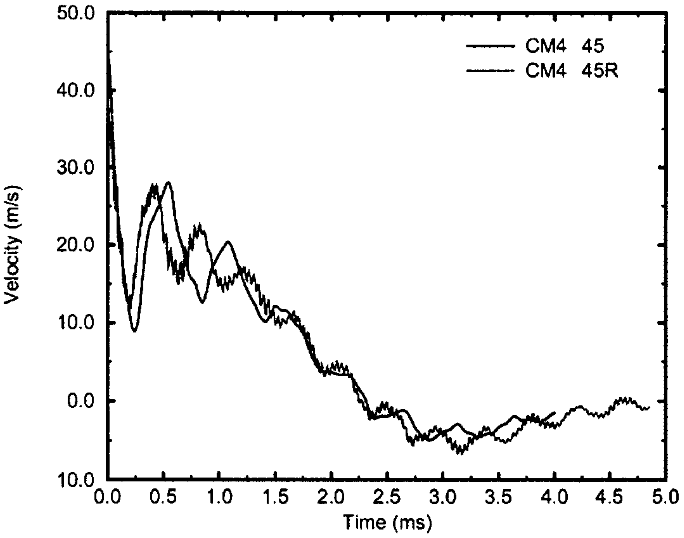

Figure 123. X-Direction Velocities of the Flyer Plate for the 45.0-m/s Crushing-Impact Computations for the M483 Munition (forward- versus reverse-ordered buffer pack).

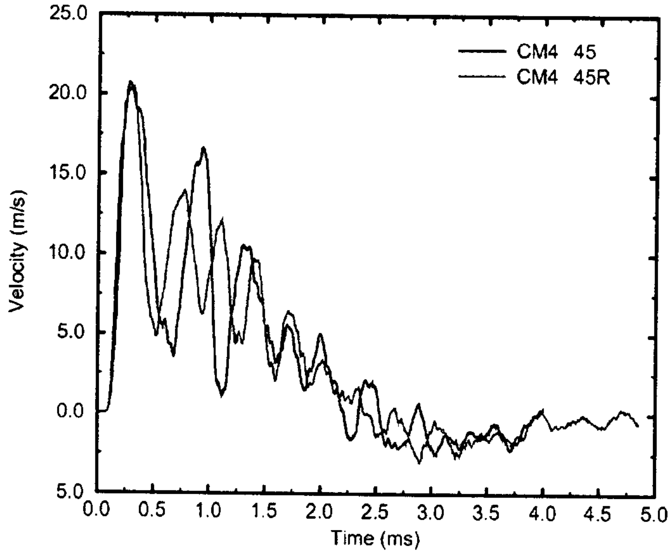

Figure 124. X-Direction Velocities of the Explosive Fill of the M483 Munition for the 45.0-m/s Crushing-Impact Computations (forward- versus reverse-ordered buffer pack).

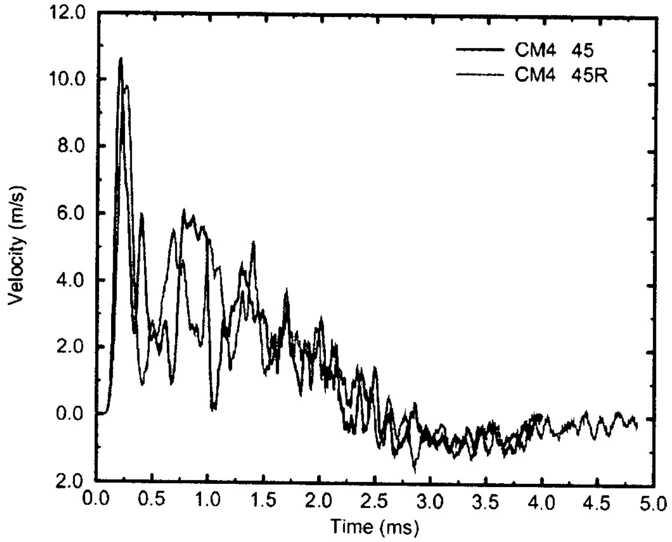

Figure 125. Y-Direction Velocities of the Explosive Fill of the M483 Munition for the 45.0-m/s Crushing-Impact Computations (forward- versus reverse-ordered buffer pack).

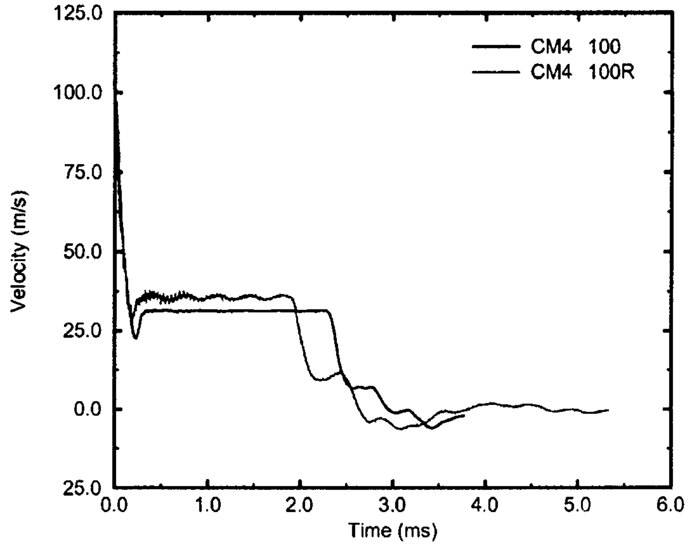

Figure 126. X-Direction Velocities of the Flyer Plate for the 100.0-m/s Crushing-Impact Computations for the M483 Munition (forward- versus reverse-ordered buffer pack).

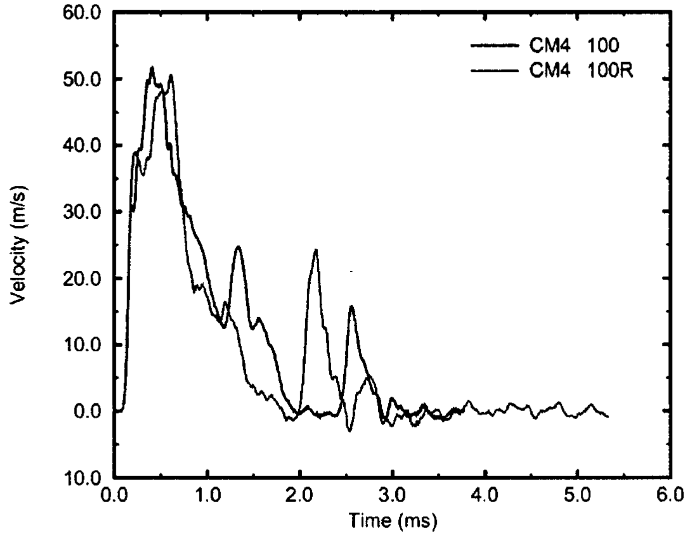

Figure 127. X-Direction Velocities of the Explosive Fill of the M483 Munition for the 100.0-m/s Crushing-Impact Computations (forward- versus reverse-ordered buffer pack).

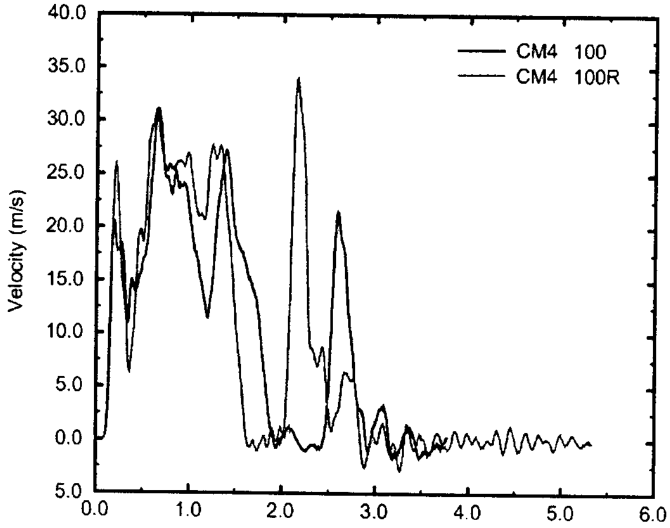

Figure 128. Y-Direction Velocities of the Explosive Fill of the M483 Munition for the 100.0-m/s Crushing-Impact Computations (forward- versus reverse-ordered buffer pack).

6. Conclusion

In general, the shock pressures that were computed in the explosive fills were below the minimum threshold levels cited by Liddiard and Forbes [1] as necessary for ignition for those computations that simulated actual experiments.[9] All computations were set up with HVRB enabled so that any computation that met the criteria for initiation would be free to proceed with a detonation of the explosive fill. No computation met the initiation criteria. No computation proceeded to an exothermic reaction in the explosive fill. This includes all computations, not just those that matched experiments. The previously reported experiments included one confirmed high-order detonation event, three explosion events, one burning event, and three events wherein no energetic reaction of the explosive fill of the munition occurred. No pressure data were reported for any of the experiments, so no direct comparisons could be made.

Computation DM2-45 simulated the one experiment in which there was a confirmed high-order detonation. The peak computed pressure identified in the tracer data in DM2-45 was approximately 143 MPa (1.43 kbar), well below the shock-initiation criteria. Because of the pre-selection of the tracer locations at grid-generation time, this does not necessarily mean that 1.43 kbar was the greatest peak for all time in the flow field, but it is most likely relatively close to being so. It is interesting to note that the crushing-impact computation, CM2-45, showed a much higher peak pressure of 300 MPa (3.0 kbar) for the selected tracers. This seemed to be somewhat counter-intuitive. The usual presumption is that the employment of a buffer pack as was used for the experiment and simulated in CM2-45 is a protective, mitigating intervention to reduce the severity of an impact. Although the M2A3 did not detonate as it did in the experiment simulated by DM2-45, the experiment that CM2-45 simulated resulted in a "Burn" reaction, which is the least energetic of the three possible categories of exothermic reactions. Analysis of computation CM2-45 indicated that there were transient separations of the plates in the buffer pack that resulted in multiple occurrences of buffer-pack plates slapping together. The plates were not bound together in either the experiments or the computations. These plate interactions generated many additional pressure spikes, some of which produced shock-on-shock pressure spikes in the explosive fill. It is quite possible to have undesirable results when testing buffer packs if the choices of materials, thicknesses, number of layers, and impedance mismatching at interfaces are not reasonably "tuned" to the structure of the incoming impact-loading wave. Taken together, these computations provide a strong indication that the mechanism for initiation in the two experiments was not shock pressure but possibly the result of the combined effects of rapid shearing under pressure.

There were some interesting differences in pressure peaks in the computations that simulated forward-ordered and reverse-ordered buffer packs. The comparison between computations CM2-45 and CM2-45R showed significant structural differences in the pressure histories at the left interface of the explosive fill. The smoothed pressure peaks at the left interface of the explosive at early time are approximately 3.0 kbar for the forward-ordered buffer pack and approximately 1.0 kbar for the reverse-ordered buffer pack. These differences were a direct result of simply changing the sequence of the layers in the buffer pack. In CM2-45 for the forward-ordered buffer pack, the impact sequences at the two ends of the buffer pack were the steel flyer plate on a Lucite layer and then a steel layer on the explosive. In CM2-45R for the reverse-ordered buffer pack, the impact sequences were the steel flyer plate on a steel layer and then a Lucite layer on the explosive.

The computations were performed with a grid resolution that was deemed to be appropriate for resolving peak shock pressures, given the desired physical space and time to be simulated. Both the experiments and the computations indicated significant deformation of the munitions at the higher impact velocities, especially the very thinly cased M2A3. A brief discussion of some of the combined pressure and flow parameters in the explosive fill was included, with the caveat that the chosen grid resolution was inadequate for a proper study of shearing. The explosive strength and failure values were also highly questionable for a proper analysis of shear and especially shear banding. All of the computations were performed within the constraints of a 2-D Cartesian coordinates system, with the munitions simulated as semi-infinite cylinders having circular cross sections. All deformations were therefore computed as plane strain. Three-dimensional effects were ignored.

The results of this report provide a further indication that a more detailed, accurate analysis of shearing in the explosive fills of munitions is warranted. It is recommended that additional experimental and computational studies be performed to further evaluate shearing as a possible initiation mechanism for explosives under low or moderate shock loading. This would require well-instrumented experiments to identify initiation sites within the explosive and the state of stress at the time. This would be a difficult task. Better constitutive models for the structural strength and failure modes of unreacted explosives are needed, along with better input data for those models that can be used to quantify their structural response under rapid loading. These models must then be incorporated into appropriate structural response computer codes. Because typical shear bands are physically quite small (on the order of 0.1 to 1.0 μm), the requirements placed on today's largest computing systems in modeling the impact loading of even a highly simplified munition would be extreme.

References

1. Liddiard, T.P., and J.W. Forbes, "A Summary Report of the Modified Gap Test and the Underwater Sensitivity Test," NSWC TR 86-350, Naval Surface Warfare Center, Silver Spring, MD, 12 March 1987.

2. Liddiard, T.P. Jr., "The Initiation of Burning in High Explosives by Shockwaves," Fourth Symposium (International) on Detonation, White Oak, MD, 12-15 October 1965.

3. Frey, R.B., "The Initiation of Explosive Charges by Rapid Shear," Proceedings, Seventh Symposium (International) on Detonation, Annapolis, MD, 16-19 June 1981.

4. Boyle, V., R. Frey, and O. Blake, "Combined Pressure Shear Ignition of Explosives," Proceedings, Ninth Symposium (International) on Detonation, Portland, OR, 28 August - 1 September 1989.

5. Howe, P.M., "On the Role of Shock and Shear Mechanism in the Initiation of Detonation by Fragment Impact," Proceedings, Eighth Symposium (International) on Detonation, Albuquerque, NM, 15-19 July 1985.

6. Howe, P.M., G.G. Gibbons, and P.E. Webber, "An Experimental Investigation of the Role of Shear in Initiation of Detonation by Impact," Proceedings, Eighth Symposium (International) on Detonation, Albuquerque, NM, 15-19 July 1985.

7. Kipp, M.E., "Modeling Granular Explosive Detonations With Shear Band Concepts," Proceedings, Eighth Symposium (International) on Detonation, Albuquerque, NM, 15-19 July 1985.

8. Coffey, C.S., M.J. Frankel, T.P. Liddiard, and S.J. Jacobs, "Experimental Investigation of Hot Spots Produced by High Rate Deformation and Shocks," Proceedings, Seventh Symposium (International) on Detonation, Annapolis, MD, 16-19 June 1981.

9. Lyman, O., R. Frey, and W. Lawrence, "Determination of a Worst-Case Acceptor for Large-Scale Sympathetic Detonation Testing," ARL-TR-490, U.S. Army Research Laboratory, Aberdeen Proving Ground, MD, July 1994.

10. Lottero, R.E., "Responses of a Water Barricade and an Acceptor Stack to the Detonation of a Donor Munitions Stack," ARL-TR-1600, U.S. Army Research Laboratory, Aberdeen Proving Ground, MD, March 1998.

11. McGlaun, J.M., S.L. Thompson, L.N. Kmetck, and M.G. Elrick, "A Brief Description of the Three-Dimensional Shock Wave Physics Code CTH," SAND 89-0607, Sandia National Laboratories, Albuquerque, NM, July 1990.

12. Bell, R.L., M.R. Baer, R.M. Brannon, M.G. Elrick, A.V. Farnsworth, E.S. Hertel, S.V. Petney, S.A. Silling, and P.A. Taylor, "CTHGEN User's Manual and Input Instructions, Version 3.00," CTH Development Project, Sandia National Laboratories, Albuquerque, NM, 18 July 1996.

13. Bell, R.L., M.R. Baer, R.M. Brannon, M.G. Elrick, A.V. Farnsworth, E.S. Hertel, S.V. Petney, S.A. Silling, and P.A. Taylor, "CTH User's Manual and Input Instructions, Version 3.00," CTH Development Project, Sandia National Laboratories, Albuquerque, NM, 18 July 1996.

14. Headquarters, Department of the Army, "Technical Manual. Army Ammunition Data Sheets. Artillery Ammunition. Guns, Howitzers, Mortars, Recoilless Rifles, Grenade Launchers, and Artillery Fuzes," TM-43-0001-28, April 1977.

15. Starkenberg, J., K.J. Benjamin, and R.B. Frey, "Predicting Fragmentation Propagation Probabilities for Ammunition Stacks," ARL-TR-949, U.S. Army Research Laboratory, Aberdeen Proving Ground, MD, January 1996.

16. Federal-Fabrics-Fibers, Inc., "Rapid Ammunition Barricade Technology Development," Small Business Innovative Research Contract DAAE30-97-C-1023, 10 March 1997.

17. Lottero, R.E., "Numerical Modeling of the Responses of a Water Barricade and an Acceptor Stack to the Detonation of a Donor Munitions Stack," Proceedings of the 28th DDESB Explosives Safety Seminar, Orlando, FL, 18-20 August 1998.

18. Bell, R.L., M.R. Baer, R.M. Brannon, M.G. Elrick, E.S. Hertel, Jr., S.A. Silling, and P.A. Taylor, "CTHGEN User's Manual and Input Instructions, Version 4.00," CTH Development Project, Sandia National Laboratories, Albuquerque, NM, 10 March 1998.

19. Bell, R.L., M.R. Baer, R.M. Brannon, M.G. Elrick, E.S. Hertel, Jr., S.A. Silling, and P.A. Taylor, "CTH User's Manual and Input Instructions, Version 4.00," CTH Development Project, Sandia National Laboratories, Albuquerque, NM, 13 March 1998.

20. Lottero, R.E., "Standoff Variation Study I: Detonation of a Donor Munitions Stack and Responses of a Trapezoidal Water Barricade and an Acceptor Stack," ARL-TR-1943, U.S. Army Research Laboratory, Aberdeen Proving Ground, MD, May 1999.

21. Lottero, R.E., "Standoff Variation Study II: Detonation of a Donor Munitions Stack and Responses of a Thin Rectangular Water Barricade and an Acceptor Stack," ARL-TR-1948, U.S. Army Research Laboratory, Aberdeen Proving Ground, MD, May 1999.

22. Lottero, R.E., "Standoff Variation Study III: Detonation of a Donor Munitions Stack and Responses of a Thick Rectangular Water Barricade and an Acceptor Stack," ARL-TR-2035, U.S. Army Research Laboratory, Aberdeen Proving Ground, MD, August 1999.

23. Kerley, G.I., "CTH Reference Manual: The Equation of State Package," SAND91-0344, Sandia National Laboratories, Albuquerque, NM, 24 May 1991.

24. Kerley, G.I., and T.L.C. Frear, "Composition B-3 Detonation Products," SAND93-2131, Sandia National Laboratories, Albuquerque, NM, 1993.

25. Starkenberg, J., and T.M. Dorsey, "An Assessment of the Performance of the History Variable Reaction Burn Explosive Initiation Model in the CTH Code," ARL-TR-1667, U.S. Army Research Laboratory, Aberdeen Proving Ground, MD, May 1998.

26. Dobratz, B.M., and P.C. Crawford, "LLNL Explosives Handbook, Properties of Chemical Explosives and Explosive Simulants," UCRL-52997, Change 2, Lawrence Livermore National Laboratory, Livermore, CA, 31 January 1985.

27. Thompson, S.L., and L.N. Kmetyk, "HISPLT: A Time-History Graphics Postprocessor, Users' Guide," SAND91-1767, Sandia National Laboratories, Albuquerque, NM, April 1994.

28. Malvern, L.E., Introduction to the Mechanics of a Continuous Medium, Prentice Hall, Inc., Englewood Cliffs, NJ, 1969.

29. Dandekar, D.P., private communication, U.S. Army Research Laboratory, Aberdeen Proving Ground, MD, February 2000.

30. Spletzer, S.V., and D.P. Dandekar, "Deformation of a Low Cost Ti-6Al-4V Armor Alloy Under Shock Loading," to be published, U.S. Army Research Laboratory, Aberdeen Proving Ground, MD, 2000.

Schreiber, E., O.L. Anderson, and N. Soga, Elastic Constants and Their Measurements, McGraw-Hill, Inc., 1973.

32. Marsh, S.P. (Editor), LASL Shock Hugoniot Data, University of California Press, Berkeley, CA 1980.

33. Dandekar, D.P., and P.J. Gaeta, "Shock, Reshock, and Release Response of Lucite to 2.1 GPa," International Conference on Mechanical and Physical Behavior of Materials Under Dynamic Loading," Ajaccio, France, 19-23 September 1988 (Journal de Physique, Tome 49, Colloque C3, supplement au n9, Septembre 1988).

NO. OF COPIES	ORGANIZATION
1	ADMINISTRATOR DEFENSE TECHNICAL INFO CTR ATTN DTIC OCA 8725 JOHN J KINGMAN RD STE 0944 FT BELVOIR VA 22060-6218
1	DIRECTOR US ARMY RSCH LABORATORY ATTN AMSRL CI AI R REC MGMT 2800 POWDER MILL RD ADELPHI MD 20783-1197
1	DIRECTOR US ARMY RSCH LABORATORY ATTN AMSRL CI LL TECH LIB 2800 POWDER MILL RD ADELPHI MD 20783-1197
1	DIRECTOR US ARMY RSCH LABORATORY ATTN AMSRL D D SMITH 2800 POWDER MILL RD ADELPHI MD 20783-1197
1	OSD ATTN OUSD(A&T)/ODDDR&E(R) ATTN R J TREW THE PENTAGON WASHINGTON DC 20310-0460
1	INST FOR ADVNCD TCHNLGY THE UNIV OF TEXAS AT AUSTIN PO BOX 202797 AUSTIN TX 78720-2797
1	DARPA 3701 N FAIRFAX DR ARLINGTON VA 22203-1714
1	NAV SURFACE WARFARE CTR ATTN CODE B07 J PENNELLA 17320 DAHLGREN RD BLDG 1470 RM 1101 DAHLGREN VA 22448-5100
1	US MILITARY ACADEMY MATHEMATICAL SCIENCES CTR OF EXCELLENCE DEPT OF MATH SCIENCES ATTN MDN A MAJ M D PHILLIPS THAYER HALL WEST POINT NY 10996-1786
1	DIRECTOR SANDIA NATL LAB DOC CONTROL 3141 PO BOX 5800 ALBUQUERQUE NM 87185-5800
2	LOS ALAMOS NATL LAB REPORT COLLECTION CIC 14 MS P364 CID 14 MS P364 PO BOX 1663 LOS ALAMOS NM 87545
1	RPT COLCTN AGENCY RSCH LAB MS P362 PO BOX 7113 LOS ALAMOS NM 87544-7113
1	DIRECTOR SANDIA NATL LAB LIVERMORE LAB DOC CONTROL FOR THE LIB PO BOX 969 LIVERMORE CA 94550
1	DIRECTOR NASA LANGLEY RSCH CTR TECH LIB HAMPTON VA 23665
1	SUNBURST RECOVERY INC ATTN C YOUNG PO BOX 2129 STEAMBOAT SPRINGS CO 80477
2	SRI INTERNATIONAL ATTN J GRAN B HOLMES 333 RAVEWOOD AVE MENLO PARK CA 94025
2	DENVER RSCH INSTITUTE ATTN J WISOTSKI TECH LIB PO BOX 10758 DENVER CO 80210
3	SOUTHWEST RSCH INST ATTN C ANDERSON S MULLIN A B WENZEL PO DRAWER 28255 SAN ANTONIO TX 78228-0255

NO. OF COPIES	ORGANIZATION
1	UNIV OF MARYLAND ATTN R DICK RM 2168 ENGRG CLASSROOM BLDG COLLEGE PK MD 20742-5121
1	US NAVAL ACADEMY ATTN TECH LIB 572 HOLLOWAY RD ANNAPOLIS MD 21402-5002
1	OLIN ORDNANCE ATTN RSCH LIB J KIBIGER PRODUCT MATERIAL CONTROL 10101 9TH ST N ST PETERSBURG Fl 33716
1	COMMANDER INDIAN HEAD DIV NSWC CODE 950T M SWISDAK 101 STRAUSS AVE INDIAN HEAD MD 20640-5035
1	COMMANDING OFFICER NFESC ATTN J TANCRETO ESC62 1100 23RD AVE BLDG 1100 PORT HUENEME CA 93043-4370
1	CHAIRMAN DOD EXPOSIVES SAFETY BOARD ATTN J WARD HOFFMAN BLDG I ROOM 856C 2461 EISENHOWER AVE ALEXANDRIA VA 22331-0600
1	DIRECTOR DEFENSE RSCH & ENGNRNG ATTN DD TWP WASHINGTON DC 20301
1	COMMANDER FIELD COMMAND DSWA ATTN FCTTS E MARTINEZ KIRTLAND AFB NM 87115
1	DIRECTOR ADV RSCH PROJECTS AGNCY ATTN TECH LIB 3701 N FAIRFAX DR ARLINGTON VA 22203-1714
1	COMMANDER USA ARDEC ATTN AMSTA FSM W BARBER BLDG 94 PICATINNY ARSENAL NJ 07806-5000
1	COMMANDER USA ENGINEER DIVISION ATTN HNDED FD PO BOX 1500 HUNTSVILLE AL 35807
1	COMMANDER USA CORPS OF ENGNRS FT WORTH DSTRCT ATTN CESWF PM J PO BOX 17300 FT WORTH TX 76102-0300
1	COMMANDER USA RSCH OFFICE ATTN SLCRO D PO BOX 12211 RSCH TRIANGLE PARK NC 27709-2211
1	COMMANDER DAVID TAYLOR RSCH CTR TECH INFO CTR CODE 522 BETHESDA MD 20084-5000
1	OFFICER IN CHARGE CIVIL ENGNRNG LAB NAVAL CONST BATTALION CTR TECH LIB CODE L31 PORT HUENEME CA 93041
1	CDR NAVAL SURF WARFARE CTR ATTN TECH LIB 17320 DAHLGREN RD DAHLGREN VA 22448-5150
1	COMMANDER NSWC DAHLGREN DIVISION LIB CODE E23 DAHLGREN VA 22448-5000
1	COMMANDER NAVAL RSCH LAB TECH LIB CODE 2027 WASHINGTON DC 20375

NO. OF COPIES	ORGANIZATION
1	COMMANDER NAVAL WEAPONS EVAL FAC DOCUMENT CONTROL KIRTLAND AFB NM 87117
2	AIR FORCE ARMAMENT LAB ATTN AFATL DOIL AFATL DLYV EGLIN AFB FL 32542-5000
1	DIRECTOR LAWRENCE LIVERMORE NATL LAB TECH INFO DEPT L 3 PO BOX 808 LIVERMORE CA 94550
1	NAIC DXLA ATTN TECH LIB 4180 WATSON WAY WRIGHT PATTERSON AFB OH 45433-5648
1	KAMAN SCIENCES CORP LIBRARY PO BOX 7463 COLORADO SPRINGS CO 80933-7463
1	DEFENSE AMMOLOG ACTWITY ATTN AMSTA AR AL D SCARBOROUGH PICATINNY ARSENAL NJ 07806-5000
1	US ARMY SOLDIER SYS CMD ATTN SSCNS WSO D LEMOINE KANSAS ST NATICK MA 01760-5018
5	USAE WATERWAYS EXP STN ATTN CEWES SD R B CARNES P KINNEBREW CEWES, TL TECH LIB CEWES SD K DAVIS CEWES SS J WEATHERSBY 3909 HALLS FERRY RD VICKSBURG MS 39180-6199
1	DIR SNL ATTN ES HERTEL JR MS 0836 PO BOX 5800 ALBUQUERQUE NM 87185-0836
1	KERLEY PUB SUC ATTN G I KERLEY PO BOX 13835 ALBUQUERQUE NM 87192-3835
1	CENTRAL INTEL AGENCY OFC OF TRANSNATIONAL ISSUES WEAPONS & TECHNOLOGY GROUP ATTN J D WALTON WASHINGTON DC 20505
	ABERDEEN PROVING GROUND
2	DIRECTOR US ARMY RSCH LABORATORY ATTN AMSRL CI LP (TECH LIB) BLDG 305 APG AA
1	COMMANDER US ARMY ATEC ATTN AMSTE TE F L TELETSKI RYAN BLDG
1	COMMANDER USATC ATTN STEC LI BLDG 400
4	DIR USARL ATTN AMSRL WM BC P PLOSTINS H EDGE B GUIDOS P WEINACHT BLDG 390
3	DIR USARL AMSRL WM MA W CHIN T MULKERN C PERGANTIS BLDG 4600
1	DIR USARL ATTN AMSRL WM T B BURNS BLDG 309
1	DIR USARL ATTN AMSRL WM TA P KINGMAN BLDG 393
1	DIR USARL ATTN AMSRL WM TB P BAKER BLDG 1185

NO. OF
COPIES ORGANIZATION

11 DIR USARL
ATTN AMSRL WM TB R FREY
T DORSEY W LAWRENCE
R LOTTERO (5 CYS)
E MCDOUGAL
J STARKENBERG
J WATSON
BLDG 309

1 DIR USARL
ATTN AMSRL WM TB
W HILLSTROM
BLDG 1119B

3 DIR USARL
ATTN AMSRL WM TC K KIMSEY
D SCHEFFLER S SCHRAML
BLDG 309

2 DIR USARL
ATTN AMSRL WM TD
M RAFTENBERG
S SCHOENFELD
BLDG 4600

6 DIR USARL
ATTN AMSRL WM TD
A M DIETRICH
P SIMMERS (5 CYS)
BLDG 309

ABSTRACT ONLY

1 DIRECTOR
US ARMY RSCH LABORATORY
ATTN AMSRL CI AP TECH PUB BR
2800 POWDER MILL RD
ADELPHI MD 20783-1197

1 DPTY CG FOR RDE HDQ
US ARMY MATL CMND
ATTN AMCRD MG CALDWELL
5001 EISENHOWER AVE
ALEXANDRIA VA 22333-0001

REPORT DOCUMENTATION PAGE

Form Approved
OMB No. 0704-0188

1. AGENCY USE ONLY *(Leave blank)*

2. REPORT DATE
August 2000

3. REPORT TYPE AND DATES COVERED
Final

4. TITLE AND SUBTITLE
A Computational Study of Munitions Response to Double Impact and Crushing Impact From a Flyer Plate

5. FUNDING NUMBERS
PR: 1L162618AH80

6. AUTHOR(S)
Simmers, P.B.; Lottero, R.E. (both of ARL)

7. PERFORMING ORGANIZATION NAME(S) AND ADDRESS(ES)
U.S. Army Research Laboratory
Weapons & Materials Research Directorate
Aberdeen Proving Ground, MD 21005-5066

8. PERFORMING ORGANIZATION REPORT NUMBER
ARL-TR-2279

9. SPONSORING/MONITORING AGENCY NAME(S) AND ADDRESS(ES)
U.S. Army Defense Ammunition Logistics Activity
Picatinny Arsenal, NJ 07806-5000

10. SPONSORING/MONITORING AGENCY REPORT NUMBER

11. SUPPLEMENTARY NOTES

12a. DISTRIBUTION/AVAILABILITY STATEMENT
Approved for public release; distribution is unlimited.

12b. DISTRIBUTION CODE

13. ABSTRACT *(Maximum 200 words)*

This report describes the results of a series of hydrocode computations, each of which modeled a steel flyer plate striking a single munition, either an M2A3 or an M483, in one of two different mounting configurations. One mounting configuration was for the munition to be first struck by the flyer plate and then to subsequently translate and strike a backing plate. The second configuration was to have the munition mounted with a buffer pack in contact on the flyer-plate side and be in initial contact with the backing plate on the opposite side. Some of the computations simulated experiments that were previously performed and reported by the U.S. Army Research Laboratory. Those experiments were not instrumented, so only limited data were produced. The primary purpose of the computations was to compute the pressures that may have occurred in the explosive fill to help explain the various exothermic reactions (or lack thereof) that occurred. Several different flyer-plate velocities were simulated in the computations. A brief discussion of parameters that may be related to ignition by shearing is also included.

14. SUBJECT TERMS
explosives safety
munitions impact
munitions storage
munitions survivability

15. NUMBER OF PAGES
135

16. PRICE CODE

17. SECURITY CLASSIFICATION OF REPORT
Unclassified

18. SECURITY CLASSIFICATION OF THIS PAGE
Unclassified

19. SECURITY CLASSIFICATION OF ABSTRACT
Unclassified

20. LIMITATION OF ABSTRACT

NSN 7540-01-280-5500

Standard Form 298 (Rev. 2-89)
Prescribed by ANSI Std. Z39-18
298-102